Theory and Simulation of Shear Flow Instabilities in Complex Fluids

HUGH JOHN BARLOW

How to cite:

BARLOW, HUGH JOHN (2020) Theory and Simulation of Shear Flow Instabilities in Complex Fluids. Doctoral thesis, Durham University.

Theory and Simulation of Shear Flow Instabilities in Complex Fluids

Hugh John Barlow

A Thesis presented for the degree of
Doctor of Philosophy

Supervised by Professor Suzanne Fielding
Department of Physics
University of Durham
UK

July 2020

Dedicated to my family

Abstract

The physics of complex fluids is important to the understanding of many biological and industrial systems. The flow properties of these materials are dominated by their mesoscopic microstructures, which can lead to a large variety of behaviours in response to deformation. In this thesis, we study flow instabilities of two such fluids in shear flow: shear-thinning viscoelastic fluids and elastoviscoplastic yield stress fluids.

Our first study examines the stability of a pressure-driven channel flow of a shear-thinning viscoelastic fluid to two-dimensional perturbations. We perform this study using three constitutive models: Rolie-Poly, Johnson-Segalman and White-Metzner. For each model, we perform linear stability analysis to determine the critical pressure drop, P'^{*}, for which the flow becomes unstable as a function of the model parameters. We find instability when the degree of shear thinning exceeds some level characterised by the logarithmic slope of the flow curve at its shallowest point.

Specifically, we show that P'^{*} obeys a criterion expressed in terms of the degree of shear-thinning,n= $\frac{d\log\Sigma}{d\log\dot{\gamma}}|_{min}$, together with the derivative of normal stress with respect to shear stress. In the Rolie-Poly and Johnson-Segalman models, the mechanism for instability appears to involve the deformation of a quasi-interface that exists in each half of the channel, across which normal stress varies rapidly. In the White-Metzner model, no such quasi-interface exists. Despite these apparent differences, the criterion for instability is of the same form in each model.

We next investigate yielding during shear start-up in soft glassy materials. Employing the soft glassy rheology model (SGR), we study the effects of sample preparation and applied shear-rate on yielding. Our study performs shear start-up on samples at zero and non-zero noise temperature, which correspond to athermal and thermal materials respectively. We perform this study using three preparation protocols commonly used in the simulation of soft glassy materials. Our results demonstrate qualitative agreement with the findings of particle-based simulations at athermal soft glasses not previously simulated using SGR.

For materials sheared at non-zero noise temperature, our calculations demonstrate that brittle yielding only occurs when the start-up curve has a sufficiently large overshoot. This is not the case for athermal materials, which display brittle yielding given any overshoot at small enough strain rate. In all protocols studied, we find close correspondence between material yielding and the formation of shear bands. This suggests that brittle yielding may be caused by the instability of a spatially homogeneous shear flow to heterogeneous shear rates during start-up, as opposed to a spinodal mechanism proposed by other authors.

Finally we study the longevity of shear bands during shear start-up in yield stress fluids using a novel lattice implementation of the soft glassy rheology model. We characterise the longevity of heterogeneous flow by calculating the time required for a material sample to completely fluidise during start-up. Our study explores the effects of sample preparation prior to the application of shear for materials at zero and non-zero effective noise temperature. We find qualitative agreement with the findings of both experimental studies and particle-based simulations. Our study shows this model to be quite effective at capturing the physics of transient shear banding in soft glassy systems.

Declaration

The work in this thesis is based on research carried out under the supervision of Prof. Suzanne Fielding, the Department of Physics, Durham Univeristy, UK. No part of this thesis has been submitted elsewhere for any other degree or qualification and it is all my own work unless referenced to the contrary in the text.

Publications

H. J. Barlow, E. J. Hemingway, A. Clarke and S. M. Fielding. Linear instability of shear thinning pressure driven channel flow. Journal of Non-Newtonian Fluid Mechanics 270 (August 2019), 66-78

H. J. Barlow, J. O. Cochran and S. M. Fielding. Ductile and brittle yield- ing in thermal and athermal amorphous materials. Physical Review Letters, 125:168003, Oct 2020

Acknowledgements

Firstly, I am deeply grateful to my supervisor Prof. Suzanne Fielding for her guidance, patience and wisdom throughout my research and without whom none of this would have been possible. She has taught me a great deal and been invaluable in helping me grow as a scientist. I am also grateful to Dr. Ewan Hemingway for his help and instruction throughout the first year of my doctorate. I wish to thank Dr. Andrew Clarke from Schlumberger Cambridge Research for the useful discussions and insights he provided as my industrial supervisor throughout the years of my PhD studies. My sincere gratitude to Prof. Helen Wilson and Dr. Hugo Castillo-Sanchez for their hosting me and for interesting discussions about channel flow during my visit to UCL.

My doctorate programme was part of the Soft Matter and Functional Interfaces Centre for Doctoral Training (SOFI CDT). Through the training provided as part of the first six months of my doctoral studies and through interactions with other soft matter scientists, I have gained invaluable exposure to a wide variety of topics from experts across academia and industry. I am indebted to the organisers for their time, efforts and dedication in making SOFI into the fantastic venture it has become.

I am sincerely grateful to all the wonderful people that I have had around me during my doctoral studies. Your friendship has helped me get through all the highs and lows of my doctoral experience. I would like to thank the wonderful people of SOFI CDT Cohort 2, the John Duck Pub Quiz team, the Durham University Hillwalking Society and all the post-docs and students of the Durham CMP group. My gratitude especially to all the other brilliant Fielding group members over the years who have helped me tremendously with their friendship, kindness and cross-

word enthusiasm. I would like to say thank you to all the other friends I have made since coming to Durham. Each and every one of you has made this a wonderful place to live and your support has been invaluable.

Finally, I would like to thank my family, to whom this thesis is dedicated, for all their care and support throughout my PhD studies.

The work in this thesis was funded by SOFI CDT, Durham University, EPSRC (EP/L015536/1) and Schlumberger Cambridge Research.

Contents

Chapter 1

Introduction

Complex fluids encompass a myriad of materials, and many have flow properties that lead to useful applications. These can vary from the domestic, such as foodstuffs and personal care products, to the industrial, such as drilling muds used in fossil fuel extraction. The flow properties of these materials result from their mesoscopic substructure, which may include jammed colloidal particles, entangled polymers and foam bubbles. When the material is deformed, the rearrangement of the substructure leads to a wide variety of fascinating mechanical responses. Rheology is the study of the way in which materials flow and mechanically respond to deformation. Flows of complex fluids can exhibit very different properties from the Newtonian variety and examples of this may be seen in the viscoelastic siphon [1], the rod-climbing Weissenberg effect [2], and the jets of the Kaye effect [3].

Fluid mechanics seeks to model how the flow of liquids evolve with time. The response of a given flow type to disturbance is often of great interest to both academic and industrial research. The dynamics of complex fluids can introduce new layers of complexity to the hydrodynamics of even simple flows. The principal aim of this thesis is to examine some of the flow instabilities that arise due to the rheology of complex fluids.

The first type of complex fluids we study are shear-thinning polymeric fluids, which include foodstuffs such as egg-whites [4], as well as industrially relevant polymer solutions and melts [5]. They also include wormlike micelles, the long flexible structures which exhibit some of the same relaxation mechanisms as polymers [6]. Pressure-driven flows, such as blood-flow in veins and arteries, are a ubiquitous example of shear flow. We shall demonstrate how a combination of rheological properties and flow geometry results in an initially simple flow becoming unstable to small perturbations.

The second variety of complex fluids we examine are elastoviscoplastic yield stress fluids. These amorphous materials include ketchup [7], mayonnaise [8], shaving-cream [9], and industrial fluids such as machine lubricants [10]. When elastoviscoplastic materials are subjected to deformation, they may behave as elastic solids for small deformation before *yielding* to viscous liquids at large deformation.

We investigate how the transition from a solid to a fluid like response is linked to a shear-induced phenomenon common to many complex fluids known as *shear-banding*. In this phenomenon, a homogeneous flow may develop into many different “bands” which coexist at a given shear stress, but at different shear-rates [11–13]. In the fluids we consider, these bands dissipate with time, and are known as *transient* shear-bands. Our studies examine the formation of these bands, as well as their development following yielding.

1.1 Layout of thesis

Three distinct studies are undertaken in this thesis. The first relates to shear-thinning polymeric fluids, the second and third to elastoviscoplastic fluids. These are discussed across three chapters, with an initial chapter introducing some of the prerequisite background information. A conclusion chapter then follows, which summarises the findings presented in this thesis and outlines future studies which may further advance the field.

1.1.1 Ch.2: Theory & Methods

The basic concepts relevant to the studies undertaken in subsequent chapters are outlined here. We introduce the formalisms used in this thesis to study hydrodynamics and their relative advantages. We also introduce the numerical methods used throughout our studies.

Some of the fundamentals of rheology, including steady-state flow curves, viscoelasticity and normal stress differences are discussed. We also describe flow instabilities in the contexts relevant to those investigations performed in the following chapters. The first is the stability of a one dimensional base state to two-dimensional perturbations as is studied in Chapter 3. Secondly, we introduce shear-banding and focus particularly on transient shear-banding and its occurrence in yield stress fluids, which is relevant to Chapters 4 and 5.

1.1.2 Ch. 3: Linear Instability of Shear-Thinning Pressure-Driven Channel Flow

The theoretical studies of Wilson and collaborators used a number of constitutive models to investigate the linear stability of pressure driven channel flow of a shear-thinning viscoelastic fluid [14–17]. Their work predicted that a one dimensional base flow of a highly shear thinning fluid may be linearly unstable to two-dimensional perturbations at high flow rates. In several later studies this prediction was proved experimentally [18–20]. Motivated by this, our study aims to find a common criterion to predict the onset of instability through linear stability analysis and full non-linear simulation, using three widely used models of shear-thinning polymeric fluids.

We numerically perform linear stability analysis of pressure driven channel flow in the phenomenological Johnson-Segalman and White-Metzner models, as well as the microscopically motivated Rolie-Poly model. We map extensively the critical pressure drop P'^{*} as a function of model parameters. In each of the models studied, we observe instability when the degree of shear-thinning, measured as the minimum logarithmic slope of the steady state flow curve $n = \frac{d\log\Sigma}{d\log\dot{\gamma}}|_{min}$ is below some critical value.

In both the Rolie-Poly and Johnson-Segalman models, we conduct full non-linear simulations which demonstrate that the unstable perturbations grow to form a system-spanning vortex at long times. We find that in the Rolie-Poly model, the flow will once again become stable at very high applied pressure drops.

We demonstrate that a general functional form can predict the critical applied pressure drop required to observe instability in each of the three models.

This criterion predicts the onset of instability as a function of the properties of the 1D base flow which stems from the steady-state 0D flow curves of the fluid. Within each model, we show that for the flow to become unstable, the applied pressure drop must exceed a value determined by the degree of shear-thinning, together with the maximum derivative of first normal stress difference with respect to shear-stress $\frac{dN_1}{d\Sigma}|_{max}$.

1.1.3 Ch. 4: Ductile to Brittle Yielding in Soft Glassy Materials

When an elastoviscoplastic material is subjected to external deformation, its material response changes from that of an elastic solid to a liquid. In some materials, this process is highly sensitive to the material history prior to deformation [21]. In this chapter, we examine this effect during shear start-up, whereby the material sample is subjected to a constant average rate of shear $\bar{\dot{\gamma}}$, switched on at some initial time $t = 0$. The transition from elastic to viscous behaviour may be gradual, a process known as *ductile* yielding, or may be sudden, called *brittle* yielding.

In recent years, several studies have proposed that a change from ductile to brittle yielding is attributed to a qualitative change in the theoretical start-up curve for a homogeneous flow [22–24]. This postulate suggests a spinodal phase transition like mechanism for brittle yielding. We challenge this hypothesis by studying theoretically how yielding behaviour varies as a result of sample preparation and applied shear-rate. Previous studies have demonstrated the yielding of soft glassy materials to be associated to time-dependent heterogeneous flow effects known as *transient shear-bands* [13, 25, 26]. Our study characterises the formation of shear-bands during yielding. We find brittle yielding to occur during start-up in well annealed samples at low shear-rates without the necessity of a qualitative change in the homogeneous start-up curves.

We use the soft glassy rheology (SGR) model to simulate the effects of sample preparation and applied shear-rate on yielding and the formation of transient shear-bands. We study the formation of bands using three different sample preparation protocols which emulate those widely used in simulation and experiment.

The adaptation of the SGR model used here for the first time, to this author's knowledge, replicates the dynamics observed in simulations of soft glassy materials performed at zero noise temperature. We show that there is a qualitative difference in yielding when shear start-up is performed at zero and non-zero noise temperature. In both systems, brittle yielding is accompanied with the formation of transient shear-bands. Our study therefore presents ample evidence to challenge the proposed interpretation of yielding in amorphous materials. Our finding instead suggests that brittle yielding results from a homogeneous flow becoming unstable to the formation of spatially heterogeneous flow rates.

1.1.4 Ch.5: Ultra-Long-Lived Transient Shear Banding in Soft Glassy Materials

Having studied the formation of shear-bands, we now move on to study their evolution. Experiments [27] and simulations [28, 29] of soft glassy materials have previously studied the longevity of transient shear-bands during start-up. They have demonstrated that the time taken for a system to completely fluidise following the formation of shear-bands may depend on both sample preparation and applied shear-rate.

We now attempt to reproduce these findings in an Elastoplastic Lattice Model. These mesoscopic models have emerged as a powerful theoretical tool to describe the dynamics of soft glassy materials [30, 31]. In this chapter we introduce a new such model that incorporates the dynamics of SGR. We are therefore able, for the first time, to incorporate ageing and other effects of finite temperature into this paradigm. We perform calculations using the ageing protocol of Moorcroft et al. [25]. In that study, very long lived shear-bands during shear start-up were observed, the longevity of which were not characterised. We measure the longevity of transient shear-bands in this protocol as a function of sample age and applied shear-rate. The second protocol we study replicates the gradual cooling preparation utilised in the simulations of Vasisht and collaborators [29, 32], which examined the longevity of shear-bands as a function of the applied cooling rate and shear-rate.

Our findings demonstrate good qualitative agreement with some of the results of simulation and experiment, reproducing particularly well the effects of the cooling protocol of Refs. [29,32]. We also find some agreement with the simulations of Refs. [28,33,34], including the observed $\bar{\gamma}^{1/2}$ growth of shear-band width as a function of strain. In both protocols, we find the longevity of shear-bands to vary as a power-law of the applied shear-rate $\bar{\dot{\gamma}}^{-p}$ in accordance with previous studies.

1.1.5 Ch. 6: Conclusions

We here summarise the findings of each chapter, and highlight where our results have furthered understanding of the relevant topic. We also discuss possible studies that may advance the research presented here.

Chapter 2

Theory & Methods

In this chapter, we introduce the basic elements of hydrodynamics, rheology and the numerical methods that will be used to study the flow behaviour of complex fluids. Firstly we introduce some hydrodynamic concepts relevant to the studies later performed in this thesis. Following this, we discuss some of the basic aspects of rheology, including the flow geometries relevant to the studies we conduct. We outline key aspects of hydrodynamic flow instabilities in viscoelastic and elastoviscoplastic fluids, including shear banding and viscoelastic turbulence. Finally, we introduce the fundamental numerical techniques used in this thesis to perform the studies undertaken.

2.1 Hydrodynamics

The Navier-Stokes equations for a generalised incompressible flow are given by

$$\rho(\partial_t \mathbf{v} + \mathbf{v} \cdot \nabla \mathbf{v}) = \nabla \cdot \mathbf{\Pi}, \tag{2.1}$$

$$\nabla \cdot \mathbf{v} = 0. \tag{2.2}$$

$\mathbf{\Pi}$ describes the total stress of the fluid, with a flow field $\mathbf{v}$ and fluid density ρ. For all systems we consider, the total stress is given by

$$\mathbf{\Pi} = 2\eta \mathbf{D} + \sigma - p\mathbf{I}, \tag{2.3}$$

where $\mathbf{D}\left(\mathbf{r}, t\right)$ is the symmetric rate of strain tensor, $\mathbf{D} = \frac{1}{2}(\nabla \mathbf{v} + \nabla \mathbf{v}^T)$ and p is the pressure which is set by enforcing incompressibility as in Eq. 2.2. The velocity gradient tensor, $(\nabla\mathbf{v})_{\alpha\beta} = \frac{\partial v_\alpha}{\partial x_\beta}$, describes rate of deformation of a material. The tensor $\sigma(\mathbf{r}, t)$ describes the stress contribution from the microscopic material elements e.g. entangled polymers, foam bubbles or suspended colloids. The $2\eta\mathbf{D}(\mathbf{r}, t)$ term corresponds to a Newtonian solvent stress, which may be attributable either to a true solvent, or to relaxation modes of the material much faster than those dominant to the dynamics of the material stress. The time dependent evolution of the material stress is described by constitutive models which shall be introduced in the relevant sections of this thesis.

The Reynolds number characterises the ratio of inertial to viscous forces in a fluid and is defined by $Re = \dfrac{\rho V L}{\eta}$, where the quantities V, L, ρ and η are the characteristic velocity, length-scale, density and viscosity of the fluid respectively. In all flow geometries we consider, we assume the limit of $Re = 0$. This assumption is valid where the fluid motion is slow, the length-scale of the system is small and the viscosity of the liquid is high, as it is in the viscometric flows that we consider in our studies. Eq. 2.1 then reduces to the Stokes equation,

$$\nabla \cdot (2\eta\mathbf{D} + \sigma - p\mathbf{I}) = 0. \tag{2.4}$$

In this limit, we assume that the flow field $\mathbf{v}$ responds instantaneously to any changes in the viscoelastic or elastoplastic stress σ in order to maintain force balance. We now illustrate how the hydrodynamics in this limit can be described using the streamfunction and Oseen formulations.

2.1.1 Streamfunction formulation

For a two dimensional incompressible flow field with velocity vector $\mathbf{v}$ and its spatial variation $\nabla\mathbf{v}$ confined to the xy-plane, assuming no flow and no variation in the $\hat{\mathbf{z}}$ direction, the streamfunction ψ is defined such that

$$\mathbf{v} = \nabla \times \psi\hat{\mathbf{z}}. \tag{2.5}$$

where $\mathbf{v} = (u, v, 0)$. u and v are the magnitude of the velocity vector in the $\hat{\mathbf{x}}$ and $\hat{\mathbf{y}}$ directions respectively. ψ is defined up to an arbitrary constant and $\psi \rightarrow \psi + const$ leaves Eq. 2.5 unchanged [35].

By substituting the expression Eq. 2.5 into Eq. 2.3 and given that $\nabla \times \nabla \cdot p\mathbf{I} = 0$ we obtain the expression

$$\eta \nabla \times \left[\nabla^2 (\nabla \times \psi \hat{\mathbf{z}}) \right] = -\nabla \times \nabla \cdot \sigma. \tag{2.6}$$

For an isotropic material, the conservation of angular momentum means the viscoelastic stress tensor must be symmetric i.e. $\sigma_{xy} = \sigma_{yx}$. Expanding each term of Eq. 2.6, we obtain the 4th order PDE

$$\eta \left(\partial_x^4 + 2\partial_x^2 \partial_y^2 + \partial_y^4 \right) \psi = \left(\partial_x^2 - \partial_y^2 \right) \sigma_{xy} - \partial_x \partial_y \left(\sigma_{xx} - \sigma_{yy} \right). \tag{2.7}$$

We shall come to use the streamfunction formulation to study channel flow in a system with mixed boundary conditions, periodic in the $\hat{\mathbf{x}}$ direction, but with fixed walls in the $\hat{\mathbf{y}}$ direction. The stream-function formalism is apposite to use in these circumstances as we shall see in more detail below.

Subject to a Fourier transform along the $\hat{\mathbf{x}}$ direction whereby $\psi\,(x, y) \rightarrow \sum\limits_{q_x} \tilde{\psi}_{q_x}\,(y)$ and $\sigma\,(x, y) \rightarrow \sum\limits_{q_x} \tilde{\sigma}_{q_x}\,(y)$, we can rewrite Eq. 2.7 (dropping subscript q_x for clarity) as

$$\eta \partial_y^3 \tilde{\psi} = -\partial_y \tilde{\sigma}_{yx} + P' \qquad q_x = 0, \tag{2.8}$$

$$\eta \left(q_x^4 - 2q_x^2 \partial_y^2 + \partial_y^4 \right) \tilde{\psi} = \left(-q_x^2 - \partial_y^2 \right) \sigma_{xy} - i q_x \partial_y \left(\tilde{\sigma}_{xx} - \tilde{\sigma}_{yy} \right) \qquad q_x \neq 0. \tag{2.9}$$

where $P^{'}$ is the average pressure gradient in the fluid along the $\hat{\mathbf{x}}$ direction. We may then solve this equation for ψ for any given wave-number q_x. This may be done for any value of q_x in order to assess the stability of a 1D base state to 2D perturbations of wave-number q_x, as we shall see in Chapter 3. We shall also use this method to perform full non-linear simulations of pressure driven flow in that study.

If we make the substitution $u = \partial_y \psi$, Eq. 2.8 becomes

$$\eta \partial_y^2 u + \partial_y \sigma_{xy} - P^{'} = 0, \tag{2.10}$$

The total shear-stress Σ is a combination of the viscoelastic shear-stress σ_{xy} and Newtonian shear-stress $\eta \partial_y u$. We may therefore rewrite Eq. 2.10 as

$$\partial_y \Sigma - P^{'} = 0. \tag{2.11}$$

From this we can see that the total shear-stress in a one-dimensional pressure-driven flow, i.e. a flow with no variation in $\hat{x}$ varies linearly in the $\hat{\mathbf{y}}$ direction, with slope P'. We make use of this equation extensively when we come to examine the instability of pressure driven channel flow in Chapter 3 of this thesis.

The stream-function formulation is an effective method for solving a two-dimensional flow in the regime described, and can also be implemented in systems with many different boundary conditions with relative ease. It is, however, usually limited to two dimensional flows. This is not a limitation that affects the Oseen Tensor formulation as we shall now see.

2.1.2 Oseen formulation

In a fully periodic system the Fourier Transform of the Stokes equation is given by the expression

$$\mathbf{0} = -\eta q^2 \tilde{\mathbf{v}}_q - i\mathbf{q}\tilde{p}_q + i\mathbf{q} \cdot \tilde{\sigma}_q, \tag{2.12}$$

where $\mathbf{q}$ denotes the wavevector. The divergence is taken by performing the dot product of each term with $i\mathbf{q}$. Using the incompressibility condition $i\mathbf{q} \cdot \tilde{\mathbf{v}}_q = \mathbf{0}$, we obtain

$$-q^2 \tilde{p}_q = i\mathbf{q} \cdot (i\mathbf{q} \cdot \tilde{\sigma}_q). \tag{2.13}$$

Rearranging this expression yields the following equation for the pressure

$$\tilde{p}_q = \frac{\mathbf{q} \cdot (\mathbf{q} \cdot \tilde{\sigma}_q)}{q^2}. \tag{2.14}$$

By substituting Eq. 2.14 into Eq. 2.12 the expression for the velocity becomes

$$\tilde{\mathbf{v}}_q = \frac{1}{\eta q^2}(\mathbf{I} - \hat{\mathbf{q}} \cdot \hat{\mathbf{q}}) \cdot (i\mathbf{q} \cdot \tilde{\sigma}_q). \tag{2.15}$$

A useful property of this formalism is that it generalises to any number of dimensions of a system with periodic boundary conditions while being relatively simple to implement computationally [36]. It is not straightforward to do so with non-periodic boundaries, although it may be done using a method of images [37]. We therefore make use of this formalism when we consider geometries with fully periodic boundaries as in Chapter 5, but utilise a stream-function formalism for systems with mixed boundary conditions as in Chapter 3.

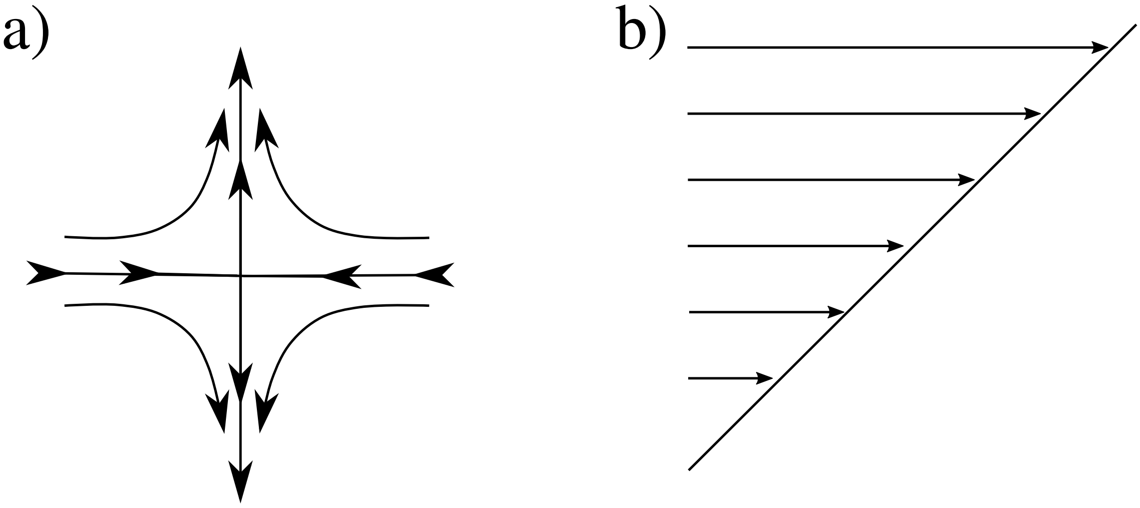

Figure 2.1: a) An extensional or simple shear flow. b) Planar shear flow.

2.2 Rheology

Rheology is the study of material response to flow deformation. Extensional flow describes one in which the material elements are stretched or extended without being sheared. Planar shear is a deformation in which the material elements in parallel planes remain parallel and are deformed relative to one another by a constant measure. Extensional and planar shear flow are sketched in Figure 2.1 a) and b) respectively. In this thesis we shall concentrate on planar shear flows. An example of such a shear-flow is a material between two parallel plates as in Figure 2.2 a) and flow is induced by imposing either a given shear-rate $\dot{\gamma}$ or shear stress Σ.

An imposed shear-rate is applied to the material by the motion of the cell wall at a fixed velocity v_{wall}. The direction of this motion is the flow direction, $\hat{\mathbf{x}}$ in Figure 2.2 a). The velocity varies between v_{wall} and 0 at a constant rate $\dot{\gamma} = v_{wall}/L_y$, which corresponds to the applied shear-rate. The direction in which the flow velocity varies, $\hat{\mathbf{y}}$ in Figure 2.2 a), is then the flow gradient direction. The direction $\hat{\mathbf{z}}$ then corresponds to the vorticity direction, along which we assume no variation in the flow. An idealised viscometric shear-flow has the form

$$\nabla \mathbf{v} = \begin{pmatrix} 0 & 0 & 0 \\ \dot{\gamma} & 0 & 0 \\ 0 & 0 & 0 \end{pmatrix}. \tag{2.16}$$

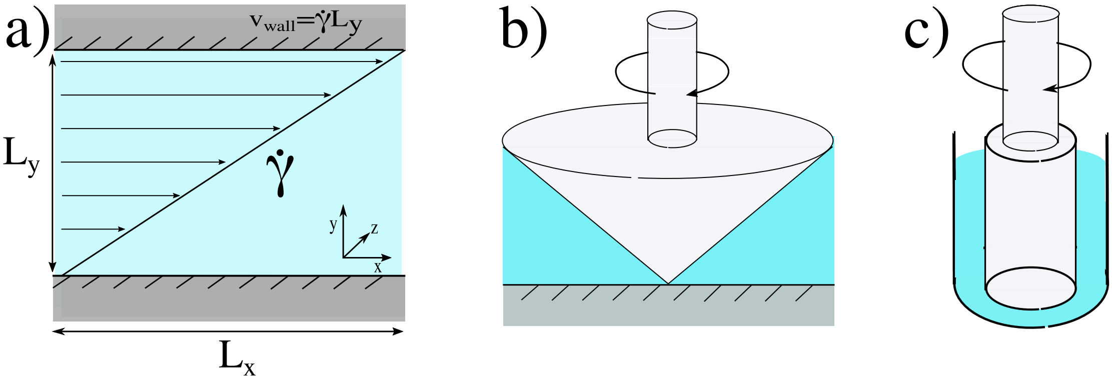

Figure 2.2: a) Shear flow betwen two plates b) A cone plate geometry. c) Taylor-Couette geometry

Here the quantity $\dot{\gamma} = \frac{\partial u}{\partial y}$, where u is the magnitude of the velocity field along the flow direction. By measuring the material response to such an imposed flow, the rheological properties may be characterised.

The flow sketched in Figure 2.2 a) is called planar Couette flow. In reality, it is difficult to implement such flow between parallel plates. Experimentalists generally use curved geometries to implement this flow type. Examples of such geometries are the cone-plate geometry as in Figure 2.2 b) and Taylor-Couette geometry Figure 2.2 c) [38].

For a Newtonian fluid, as shown in Figure 2.3 the stress is linearly proportional to the applied shear-rate. More generally the total stress tensor of a Newtonian fluid is described by the equation

$$\mathbf{\Pi} = 2\eta\mathbf{D} - p\mathbf{I}. \tag{2.17}$$

The viscosity η is defined as the ratio $\Sigma/\dot{\gamma}$, where Σ is the total shear-stress of the material. For a Newtonian fluid, this value is constant and does not depend on the applied shear-rate or shear-stress. The resultant stress tensor for a uniform shear-flow is then given by

$$\mathbf{\Pi} = \begin{pmatrix} -p & \eta\dot{\gamma} & 0 \\ \eta\dot{\gamma} & -p & 0 \\ 0 & 0 & -p \end{pmatrix}. \tag{2.18}$$

When the shear-stress for a Newtonian fluid is then plotted against the applied shear-rate, the result is a straight line through the origin. The measured stress against applied shear-rate of a material is known as its *flow curve*, and is a vital quantity when characterising the rheological properties of a fluid.

Many complex fluids exhibit non-linear (non-Newtonian) flow curves [38]. Examples of some common rheological behaviours observed in complex fluids are shown in Figure 2.3. Some of the mostly widely studied examples of non-Newtonian fluids include shear-thinning and shear-thickening fluids. The viscosity of a *shear-thinning* fluid decreases with increasing applied shear-rate. Examples include colloidal suspensions [39] and most polymer solutions [40]. A *shear-thickening* fluid will demonstrate the converse effect, becoming more viscous with increasing shear-rate, examples are found in telechelic polymeric fluids [38] and cornstarch and clay suspensions (for reviews see Ref. [41–43]).

In the case of yield stress fluids, no flow is observed below a critical yield stress Σ_y, but the material flows as a plastic fluid above this stress. This phenomenon known as viscoplasticity, and is so called due to the soft solid material yielding in an irreversible manner above Σ_y after which it behaves as a fluid. This behaviour is observed in foams, muds and emulsions such as mayonnaise (for reviews see Ref. [44, 45]).

A Bingham fluid is such a yield stress fluid, the flow curve of which is described by the equation $\Sigma\left(\dot{\gamma}\right) = \Sigma_y + A\dot{\gamma}$ for $\Sigma\left(\dot{\gamma}\right) > \Sigma_y$, where A is some constant of proportionality [46]. For $\Sigma\left(\dot{\gamma}\right) < \Sigma_y$, the material does not flow, therefore $\Sigma\left(\dot{\gamma}\right) = 0$. In many yield stress materials, the stress varies non-linearly as a function of the applied shear-rate. The yield stress fluids we consider in this thesis also display an elastic component of stress and are therefore considered to be *elastoviscoplastic* fluids.

2.2.1 Viscoelasticity

Viscoelasticity is the property whereby materials may exhibit characteristics of both an elastic solid and a viscous liquid depending on the timescale over which they are observed. A good means of elucidating the properties of such materials is to discuss the effects of imposing a constant shear-rate on a sample of the material. At a fixed time $t = 0$, a sample of a material previously at rest is subjected to a constant shear-

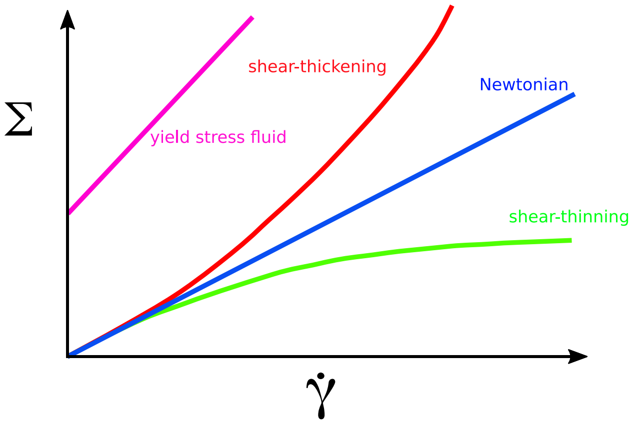

Figure 2.3: Flow curves for a range of rheological behaviours.

rate $\dot{\gamma}$ for all $t > 0$. The resulting shear-stress Σ is then measured as a function of time (or of the applied strain $\gamma = \dot{\gamma}t$). This protocol is known as shear start-up.

In absence of inertia, the shear stress on a Newtonian fluid subjected to a fixed shear-rate $\dot{\gamma}$ instantaneously reaches a steady state value such that $\Sigma = \eta\dot{\gamma}$ where η is the viscosity of the fluid. In an elastic solid, the material stress increases linearly as a function of applied strain such that $\Sigma = G\dot{\gamma}t$ where G is the elastic shear-modulus and t is the time during which strain is applied. Many materials fit into neither of categories, but are *viscoelastic* and display both elastic and viscous properties. During applied shear, these materials initially deform as an elastic solid before gradually changing to a fluid like response. A very simple model of such a viscoelastic fluid is the Maxwell model [47]

$$\partial_t \Sigma = G\dot{\gamma} - \frac{1}{\tau}\Sigma. \tag{2.19}$$

Here τ is the *viscoelastic relaxation time* of the material. By imposing $\Sigma(0) = 0$ and solving for $\Sigma(t)$ we obtain the solution

$$\Sigma(t) = G\tau\dot{\gamma}\left(1 - e^{-\frac{t}{\tau}}\right). \tag{2.20}$$

By varying the relaxation time τ the fluid will behave more like an elastic solid or a viscous fluid during start-up. For a very large value of τ the fluid will take a very long time to transition to a fluid like state, while conversely for a very small value it will transition quickly. The quantity $G\tau$ then corresponds to the viscosity of the

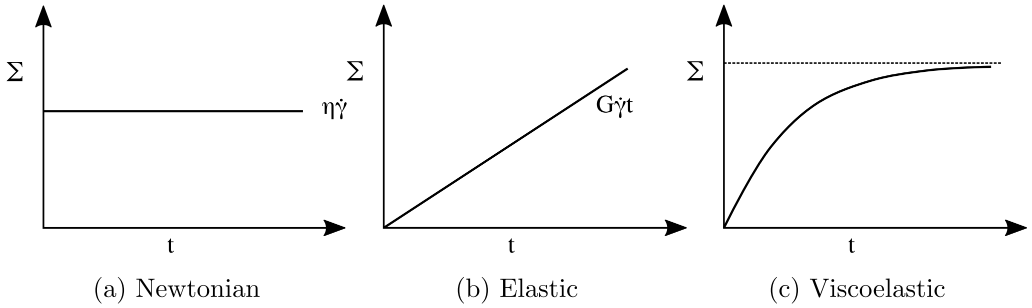

(a) Newtonian (b) Elastic (c) Viscoelastic

Figure 2.4: Start-up curves for a fixed shear-rate $\dot{\gamma}$ for a) Newtonian fluid b) Elastic solid c) viscoelastic material (steady state value shown in dashed line).

material. Sketches of shear start-up are shown in Figure 2.4 for a) a Newtonian fluid, b) an elastic solid and c) a viscoelastic material.

Viscoelasticity is a common feature of complex fluids including polymeric materials [38,48]. While many viscoelastic fluids may exhibit non-linear flow curves, there also exist constant viscosity viscoelastic fluids, known as Boger fluids [49]. The fluid described by the Maxwell model used here is such an example. The start up behaviour sketched here is only a very simple example of the many varieties of start-up behaviour observed in complex fluids. We examine some of these when we study age dependent start-up in elastoviscoplastic materials.

2.2.2 Normal stress differences

In many complex fluids, the stress response to a uniform imposed shear-rate $\dot{\gamma}$ as in Eq. 2.16 is not characterised purely by the scalar shear-stress Σ as in a Newtonian fluid. The viscoelastic stress tensor σ may instead be of the form

$$\sigma = \begin{pmatrix} \sigma_{xx} & \sigma_{xy} & 0 \\ \sigma_{yx} & \sigma_{yy} & 0 \\ 0 & 0 & \sigma_{zz} \end{pmatrix} \tag{2.21}$$

The off diagonal terms correspond to the viscoelastic shear-stress as described by the flow curves. The diagonal terms of the stress tensor are *normal stress* terms. Experimentally one can only measure components of the total stress tensor $\mathbf{\Pi} = \sigma + 2\mathbf{D} - p\mathbf{I}$, for which the normal stress terms include the hydrostatic pressure p.

Hence one cannot measure the normal stress components explicitly, but only the normal stress differences [50]

$$N_1 = \sigma_{xx} - \sigma_{yy} \tag{2.22}$$

$$N_2 = \sigma_{yy} - \sigma_{zz}. \tag{2.23}$$

Here N_1 and N_2 are the *first normal stress difference* and *second normal stress difference* respectively. Normal stress differences typically arise from the microstructure of the fluid becoming anisotropic in the presence of flow. In the context of a polymeric fluid under a simple shear flow, the polymers align with the flow direction. They are stretched along this direction and entropic forces then act to return the polymer to an isotropic conformation. This results in the normal stresses just described [51].

2.2.3 Pressure Driven Channel Flow

We now introduce the fundamentals of another type of shear-flow pertinent to this thesis, pressure driven channel flow. An idealised shear flow in two dimensions is described by the flow gradient tensor

$$\nabla \mathbf{v} = \begin{pmatrix} 0 & 0 \\ \dot{\gamma} & 0 \end{pmatrix}. \tag{2.24}$$

In planar Couette flow this $\dot{\gamma}$ is a constant across the channel and is specified by the velocity of the wall v_{wall}. This is no longer the case in a pressure driven flow. In the geometry we consider, the walls are fixed and the flow speed is determined by the applied average pressure gradient P'. The local shear-rate within the channel, $\dot{\gamma}(y)$ is then a function of position.

The Stokes equation for a one-dimensional (1D) pressure-driven channel flow for any fluid with a shear-stress Σ is given by

$$\partial_y \Sigma - P' = 0. \tag{2.25}$$

The shear-stress will then vary linearly within the channel $\Sigma \propto P'y$. In a constant viscosity fluid, with shear-stress $\Sigma = \eta\dot{\gamma}$, the shear-rate then varies linearly as a function of position in the channel, and flow speed $u(y)$ will be parabolic $u(y) \propto P'y^2/\eta$.

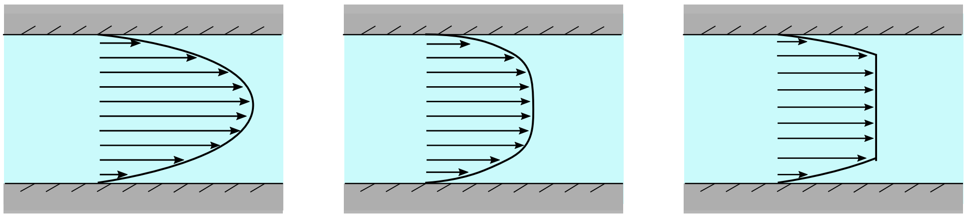

(a) Newtonian (b) Shear-thinning (c) Yield Stress Fluid

Figure 2.5: Flow profiles for different fluids under an applied pressure gradient between fixed walls.

This is not the case for a non-constant viscosity fluid, for which the shear stress may vary in a non-linear manner as a function of shear-rate. The shear-rate for a pressure driven flow of such a fluid therefore varies according to the flow curve of the fluid in question. Sketched examples of flow profiles for different fluids (for a 1D flow) are shown in Figure 2.5. We examine such pressure driven channel flows in Chapter 3 of this thesis. Specifically, we study instabilities that may arise in pressure driven flows for shear-thinning viscoelastic fluids.

2.2.4 Flow Instability

The studies conducted in this thesis explore flow instability in complex fluids. Instability in this context refers to the emergence of complex behaviours from initially simple flow states. This has long been a topic of study in broader fluid mechanics. Complex fluids may demonstrate instabilities in flow regimes where inertial effects are minimal and the flow of a Newtonian fluid would be stable [52–57]. We examine in detail two such instabilities. The first is the emergence of two-dimensional (2D) flow from a one-dimensional (1D) base state. The second is the formation of transient shear-bands during shear start-up. We now introduce some of these concepts here, before they are re-explored in greater detail within the following relevant chapters.

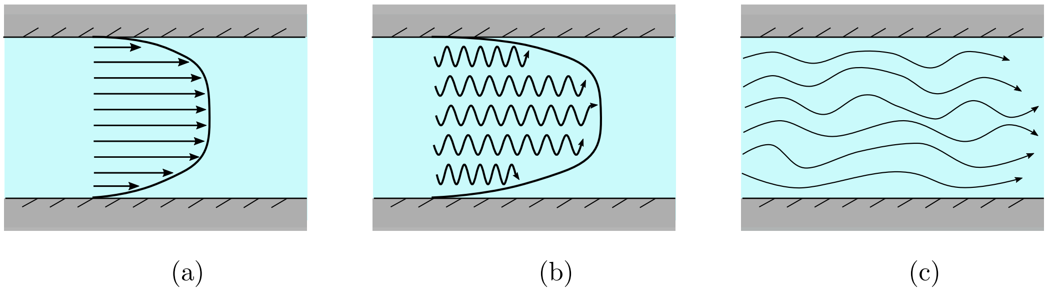

Figure 2.6: a) A 1D base state prior to the application of perturbation. b) Periodic 2D perturbations applied throughout the channel. The perturbations grow or shrink depending on the stability of the base state. c) At long times an unstable base state may transition to a non-linear state, demonstrating unsteady flow behaviour.

2.2.5 Instability of a 1D base state to 2D perturbations

Consider a flow within an infinitely long channel of height L_y. The *base state* flow within the channel varies only in the cross channel direction $\hat{\mathbf{y}}$ and is uniform along the direction $\hat{\mathbf{x}}$. The flow-field $\mathbf{v}(x, y) = (U(y), 0)$. We consider this flow to be one-dimensional (1D), since it varies only in a single direction. Such a base flow is sketched for a shear thinning pressure driven flow in Figure 2.6 a).

We use linear stability analysis to assesses the response of an initially 1D base flow to infinitesimally small perturbations of the form $\delta\mathbf{v}(y)\exp(iqx + \omega_q t)$, where q is the wavenumber of the perturbation and ω_q is the eigenvalue corresponding to the wavenumber q. These perturbations may result in experiment from mechanical or thermal noise, but are be added numerically in the studies performed here. After these perturbations are added, they may grow or shrink depending on whether the flow is unstable or stable respectively. If stable, these perturbations will shrink and the original 1D base state will be recovered. If unstable, the perturbations will grow exponentially up to some value where the flow effects become non-linear and the flow may transition to turbulence (see Figure 2.6 c)). The growth rate of these perturbations is determined by the real part of the eigenvalue $Re(\omega_q)$. If $Re(\omega_q) > 0$ the base state is unstable to perturbations of wavenumber q, while if $Re(\omega_q) < 0$ the flow is stable.

In Chapter 3, we analyse the stability of pressure-driven channel flow of

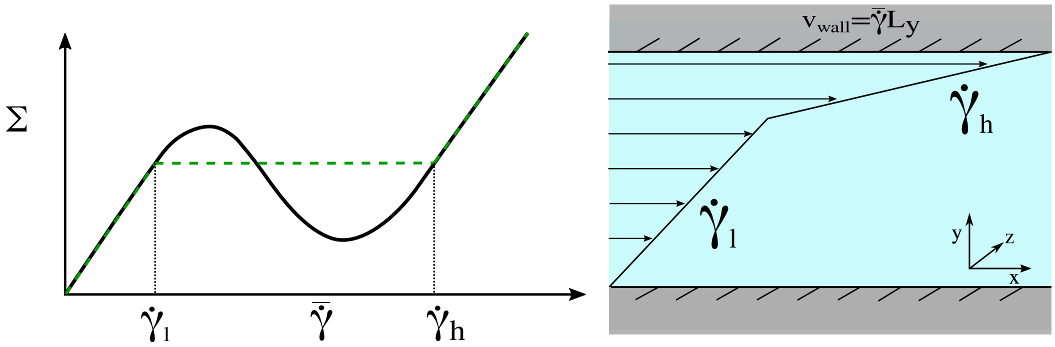

(a) (b)

Figure 2.7: a) The constitutive curve (solid black line) and flow curve (broken green line) of a shear-banding fluid. b) Shear-banded flow between parallel plates. The flow separates into regions of low and high shear-rates $\dot{\gamma}_l$ and $\dot{\gamma}_h$ respectively.

a shear-thinning viscoelastic fluid. In that chapter, we study the stability of the flow to infinitesimally small perturbations in the linear regime. At longer timescales we see how these perturbations grow to a finite amplitude, producing non-linear behaviour. We describe in detail the process by which we undertake the linear stability analyis that has been outlined here. The work done here is inspired by previous theoretical studies [14–17] and by results obtained experimentally [18–20]. These studies have shown such flows to be linearly unstable for a combination of sufficient shear-thinning and high pressure gradients. We expand on this previous work and develop criteria for instability based on characteristics of the 1D base state.

2.2.6 Shear Banding

A *constitutive curve* gives the measured response in shear-stress subject to a fixed homogeneous shear-rate $\Sigma(\dot{\gamma})$. This may be a theoretically idealised flow and not attainable experimentally. A flow curve is the material response directly measured when a material is sheared in a system where spatial heterogeneities may develop. In the cases where heterogeneities do not emerge these are equivalent. For some materials this is not the case. We see in Figure 2.7 a), such an example where the homogeneous constitutive curve and heterogeneous flow curve are different from each other.

Some fluids may exhibit an extreme level of shear-thinning such that the constitutive curve is non-monotonic and the material exhibits a phenomenon known as shear banding [58]. In this phenomenon the homogenous flow profile is unstable to the formation of distinct regions of high and low shear-rate ($\dot{\gamma}_h$ and $\dot{\gamma}_l$ as shown) which coexist within the cell as in Figure 2.7 b). Hence the heterogeneous flow curve will show a different response to a homogeneous constitutive curve. The flow is linearly unstable to the formation of these bands for the non-monotonic region of the constitutive curve, but depending on the previous history of flow deformation, bands can also form in the surrounding metastable regions. This behaviour is observed in a wide variety of complex fluids and reviews of both experimental and theoretical progress on the study of shear-banding may be found in Refs. [11, 13, 59, 60]. We do not directly study systems that display steady-state shear-banding in this thesis, but study the related phenomenon of time-dependent shear-banding.

Time-Dependent Shear Banding

We have discussed how a material with a non-monotonic constitutive curve may demonstrate steady state shear-banding. However, many materials may demonstrate shear-banding during the time-dependent stress response in start-up, a behaviour seen in many soft glassy materials [12, 21, 44] and polymeric fluids [13, 61]. During start-up, viscoelastic and elastoviscoplastic fluids transition from an elastic like response to fluid-like behaviour. Transient shear bands are formed when this process does not happen uniformly in a sample, but instead portions of the sample fluidise more rapidly than others. This leads to regions of the flow having different shear-rates. Over time, the fluidised regions grow until all of the material sample is completely fluidised and the shear-rate is once again uniform. These heterogeneous shear-rates may occur during many different rheological protocols, such as in large amplitude oscillatory shear [62, 63], stress imposed flow [64, 65], channel flow [66] and, the main focus of our studies, shear start-up [25, 27, 67]. For polymeric materials the criteria for the formation of transient shear bands in a wide variety of these start-up protocols was developed by Moorcroft et al. [68, 69].

Our focus in the studies performed here is the emergence of this phenomenon in yield stress fluids, where transient shear-bands have been found to occur in carbopol gels [27,70], laponite clays [71,72], fumed silica [73], carbon-black gels [65,74,75] and waxy crude oil [76]. A stress overshoot is often observed during shear start-up in these fluids, i.e. during start up the transient stress may exceed the steady state value [64,72]. The presence or absence of this overshoot may depend on the history of the sample, including how long the sample is aged prior to being deformed [21,67,77]. Fielding and collaborators have shown that this overshoot is required for the formation of transient shear-bands during shear start-up using both fluidity and elastoviscoplastic models of age dependent soft glassy materials [25,26]. In Chapter 4 of this thesis, we focus on the formation of these bands, and the link between their formation and material yielding. We examine the effects of sample age, shear-rate and different preparation protocols on the transient rheology of yield stress fluids.

Moorcroft et al. [25] noted that these bands may persist to very large values of strain, but did not explicitly characterise their longevity. Divoux and collaborators have shown that the timescale for fludisation τ_f in a carbopol gel is dependent on the applied shear-rate [27] or shear-stress [64]. We study the longevity of these bands theoretically, evaluating the effects of preparation and shear-rate on the timescale of fluidisation in Chapter 5 of this thesis.

2.3 Numerical Implementation

The systems studied here are described by coupled differential equations which are evolved numerically. We use several methods in order to solve the hydrodynamic and constitutive equations of interest. We now outline these, beginning with the Finite Difference and Fourier methods used to evaluate non-local terms, before discussing the time-stepping routines used to evolve the dynamical equations.

2.3.1 Finite Difference Method

Differentiation-Centred Difference

The finite difference method uses a set of discrete grid points to approximate a continuous function [78]. Derivatives are taken as a function of neighbouring grid points. We can derive these expressions by taking a Taylor series expansion of a function $\phi\left(y\right)$. We consider the value of this function at a point y_0, $\phi\left(y_0\right)$ and perform a Taylor series expansion to approximate the values of $\phi\left(y_0+\Delta y\right)$ and $\phi\left(y_0-\Delta y\right)$

$$\phi(y_0+\Delta y)=\phi(y_0)+\Delta y\frac{d\phi}{dy}|_{y=y_0}+\frac{\Delta y^2}{2}\frac{d^2\phi}{dy^2}|_{y=y_0}+\mathcal{O}(\Delta y^3) \tag{2.26}$$

$$\phi(y_0-\Delta y)=\phi(y_0)-\Delta y\frac{d\phi}{dy}|_{y=y_0}+\frac{\Delta y^2}{2}\frac{d^2\phi}{dy^2}|_{y=y_0}+\mathcal{O}(\Delta y^3) \tag{2.27}$$

The first derivative $\frac{d\phi}{dy}|_{y=y_0}$ can then be approximated to an accuracy of $\mathcal{O}\left(\Delta y^2\right)$ by taking the difference of these equations and rearranging

$$\frac{d\phi}{dy}|_{y=y_0}\approx\frac{\phi(y_0+\Delta y)-\phi(y_0-\Delta y)}{2\Delta y}. \tag{2.28}$$

The second derivative may also be approximated by summing to give

$$\frac{d^2\phi}{dy^2}|_{y=y_0}\approx\frac{\phi\left(y_0+\Delta y\right)-2\phi\left(y_0\right)+\phi\left(y_0-\Delta y\right)}{\Delta y^2}. \tag{2.29}$$

Higher order derivatives are approximated by expanding to a larger number of terms. By using these expansions, combined with discretisation of space into elements separated by a distance Δy, we may approximate the derivatives of a continuous function. We also see how such a method may be used to solve differential equations.

Eq. 2.28 is accurate up to $\mathcal{O}(\Delta y^2)$, but higher accuracy expressions are obtained by summing series that expand to higher orders, and in turn utilise a larger number of grid points to approximate the derivative. Such a case is when calculating upwind derivatives in order to evaluate advective terms.

Differentiation-Upwinding

So far we have discussed centred derivatives where the value of a derivative at some gridpoint is taken as an equal function of elements either side of itself. However there exist scenarios where this is not optimal. Such an example is in the case of advective quantities in a flow field. Consider the advective equation

$$\partial_t \phi + \mathbf{v} \cdot \nabla \phi = 0. \tag{2.30}$$

where $\mathbf{v} = (u, v, 0)$ is the two dimensional flow field that advects the scalar quantity ϕ. Numerically solving these equations on a discretised mesh can lead to what are called transport errors. The source of these errors is clear if we expand the terms of Eq. 2.30

$$\partial_t \phi + u \partial_x \phi + v \partial_y \phi = 0. \tag{2.31}$$

Using a centred derivative, $\partial_x \phi$ and $\partial_y \phi$ are approximated in either direction of the flow. In reality, however, if u is positive, then only points which are in the positive direction are advected, and so information is lost using a centred method. In order for information to be preserved and propagate in the correct direction, we therefore use an upwinding finite difference method which accounts for the direction of the flow field [78]. Where this is utilised, we make use of a third order upwinding formalism [78]. We consider the quantity ϕ being advected in the $\hat{\mathbf{y}}$ direction in a channel of width L_y in the $\hat{\mathbf{y}}$ direction. The channel $\hat{\mathbf{y}}$ direction is discretised into a grid of $N_y + 1$ elements, with index $j = 0, ..., N_y$ and space step $\Delta y = L_y / N_y$. At each grid point j, the value of $y = L_y j / N_y$. At any grid point j, the derivative is determined by the conditional expression;

$$\begin{aligned} \frac{\partial \phi}{\partial y} &= \frac{1}{6\Delta y} \left(-\phi_{j+2} + 6\phi_{j+1} - 3\phi_j - 2\phi_{j-1} \right) & \quad v_j < 0 \\ \frac{\partial \phi}{\partial y} &= \frac{1}{6\Delta y} \left(\phi_{j-2} - 6\phi_{j-1} + 3\phi_j + 2\phi_{j+1} \right) & \quad v_j > 0. \end{aligned} \tag{2.32}$$

Here we see that the derivative takes into account the direction of the flow field, biasing the derivative against the direction of the flow (i.e "upwind"). Higher order upwinding methods may be used for flows that require a greater level of accuracy to obtain numerical stability [79], but for the studies undertaken in this thesis the third order formulation in Eq. 2.32 is sufficient.

Boundary Conditions and Integration

In order to solve differential equations using the finite difference method, we must be able to apply relevant boundary conditions. As a working example, we may consider the ordinary differential equation describing the scalar quantity ϕ

$$\frac{d^2\phi}{dy^2} = f\left(y\right), \tag{2.33}$$

within the region $0 \leq y \leq L_y$, where the function $f\left(y\right)$ is some known continuous function of y. We impose boundary conditions such that $\frac{d\phi}{dy}|_{y=0} = \frac{d\phi}{dy}|_{y=L_y} = 0$. This is known as a Neumann boundary condition as it imposes a fixed value on a gradient term. To impose this numerically using a finite difference method, we use so called phantom points. We first discretise the channel in the $\hat{\mathbf{y}}$ direction on a grid of $N_y + 1$ elements, with index $j = 0, ..., N_y$. The space between each element is then $\Delta y = L_y/N_y$. The value of y on each grid point is then given by $y = L_y j/N_y$. In this discretised grid Eq. 2.33 is approximated at each element by

$$\frac{\phi_{j+1} - 2\phi_j + \phi_{j-1}}{\Delta y^2} = f\left(L_y j/N_y\right). \tag{2.34}$$

At the edges of the region, where $y = 0$ and $y = L_y$, we construct points beyond the grid such that

$$\frac{\phi_1 - 2\phi_0 + \phi_{-1}}{\Delta y^2} = f\left(0\right) \tag{2.35}$$

and

$$\frac{\phi_{N_y+1} - 2\phi_{N_y} + \phi_{N_y-1}}{\Delta y^2} = f\left(L_y\right). \tag{2.36}$$

Our prescribed boundary conditions are then

$$\frac{\phi_1 - \phi_{-1}}{2\Delta y} = 0 \tag{2.37}$$

at the channel wall $y = 0$ and

$$\frac{\phi_{N_y+1} - \phi_{N_y-1}}{2\Delta y} = 0 \tag{2.38}$$

at the channel wall $y = L_y$.

Solving for phantom points ϕ_{-1} and ϕ_{N_y+1}, and inserting these into Eqs. 2.35 and 2.36 we obtain

$$\frac{2\phi_1 - 2\phi_0}{\Delta y^2} = f\left(0\right) \tag{2.39}$$

and

$$\frac{-2\phi_{N_y} + 2\phi_{N_y+1}}{\Delta y^2} = f\left(L_y\right). \tag{2.40}$$

We can now decompose the system described by Eq. 2.33 with these boundary conditions as $N_y + 1$ coupled simultaneous equations;

$$\begin{aligned}
\frac{-2\phi_1 + 2\phi_0}{\Delta y^2} &= f\left(0\right) \\
\frac{\phi_2 - 2\phi_1 + \phi_0}{\Delta y^2} &= f\left(\frac{1}{N_y}L_y\right) \\
\frac{\phi_3 - 2\phi_2 + \phi_1}{\Delta y^2} &= f\left(\frac{2}{N_y}L_y\right) \\
\frac{\phi_4 - 2\phi_3 + \phi_2}{\Delta y^2} &= f\left(\frac{3}{N_y}L_y\right) \\
&\vdots \\
\frac{\phi_{N_y} - 2\phi_{N_y-1} + \phi_{N_y-1}}{\Delta y^2} &= f\left(\frac{N_y-1}{N_y}L_y\right) \\
\frac{2\phi_{N-1} - 2\phi_N}{\Delta y^2} &= f\left(L_y\right).
\end{aligned}$$

These in turn can be written in the form of an $(N_y + 1) \times (N_y + 1)$ matrix equation

$$\frac{1}{\Delta y^2}\begin{pmatrix}
2 & -2 & 0 & 0 & 0 & 0 & \dots & 0 \\
1 & -2 & 1 & 0 & 0 & 0 & \dots & 0 \\
0 & 1 & -2 & 1 & 0 & 0 & \dots & 0 \\
0 & 0 & 1 & -2 & 1 & 0 & \dots & 0 \\
\vdots & \ddots & \ddots & \ddots & \ddots & \ddots & \ddots & \vdots \\
0 & \dots & 0 & 0 & 1 & -2 & 1 & 0 \\
0 & \dots & 0 & 0 & 0 & 0 & 2 & -2
\end{pmatrix}
\begin{pmatrix}
\phi_0 \\ \phi_1 \\ \phi_2 \\ \phi_3 \\ \vdots \\ \phi_{N_y-1} \\ \phi_{N_y}
\end{pmatrix}
=
\begin{pmatrix}
f\left(0\right) \\
f\left(\frac{1}{N_y}L_y\right) \\
f\left(\frac{2}{N_y}L_y\right) \\
f\left(\frac{3}{N_y}L_y\right) \\
\vdots \\
f\left(\frac{N_y-1}{N_y}L_y\right) \\
f\left(L_y\right)
\end{pmatrix} \tag{2.41}$$

By inverting this matrix, we can then solve for ϕ at each grid-point. One may apply other boundary conditions in a similar manner using a finite difference method. This includes periodic boundary conditions, which we also consider in our studies here. A limitation of the finite difference method, however, is that derivatives are only calculated from adjacent grid elements. The information used to calculate derivatives is therefore limited by the number of adjacent elements used. We can obtain greater numerical accuracy by increasing either the total number of elements, thus reducing Δy, or the number of adjacent points used. However, doing so may prove very computationally expensive. When we come to study systems with periodic boundary conditions, we therefore make use of Fourier methods, which have several advantages over finite difference methods.

2.3.2 Fourier Methods

In geometries with periodic boundaries, it is convenient to make use of Fourier methods to solve differential equations. Numerically this is done by decomposing the quantity into a Fourier series using a Discrete Fourier Transform. In a periodic system of size L_x the function $\phi(x)$ thus becomes

$$\phi(x) = \sum_{q_x} \tilde{\phi}_{q_x} \exp(iq_x x), \tag{2.42}$$

where $q_x = 2\pi q_x^{'}/L_x$ is the wavenumber and $\tilde{\phi}_{q_x}$ is the Fourier transform of the function $\phi(x)$ with wavenumber q_x and mode number $q_x^{'}$ [80]. When a Discrete Fourier transform is performed on a system of N_x elements approximating a system of size L_x, the highest frequency mode is determined by the number of elements.

As an example of how Fourier methods may be used to solve differential equations, let us consider the system described by the second order differential equation

$$\frac{d^2\phi}{dx^2} = g(x). \tag{2.43}$$

In this system both $\phi(x)$ and $g(x)$ are continuous periodic functions of x. By properties of a Fourier transform, derivatives in Fourier space become

$$\partial_x^n \phi(x) = \sum_{q_x} (iq_x)^n \tilde{\phi}_{q_x} \exp(iq_x x). \tag{2.44}$$

By performing a Fourier transform to Eq. 2.43, we therefore obtain for each q_x

$$-q_x^2 \tilde{\phi}_{q_x} = \tilde{g}_{q_x}, \tag{2.45}$$

where $\tilde{g}_{q_x}$ is the Fourier transform of the function $g(x)$ for wavenumber q_x. To obtain a solution for $\phi(x)$ we divide both sides of this equation by $-q_x^2$ and perform an inverse Fourier transform. This method is used in the following studies to solve differential equations with periodic boundaries.

As with all computational techniques, there are both advantages and disadvantages to the use of Fourier methods to solve differential equations numerically. A key merit over using finite difference methods for the same systems is that the calculation of derivatives uses information from throughout the system, not just from locally adjacent grid points. This can mean that a greater numerical accuracy may be achieved for a much smaller mesh. The principal disadvantage however comes from the computational resources required to perform Fourier transforms on large numbers of elements. The use of Fast Fourier Transform algorithms mitigates this [81], but for very large systems their use may still prove computationally intensive.

In a completely periodic system, Fourier methods may be used to evaluate all derivatives of a set of equations, as in Chapter 5. In the case of systems with mixed boundary conditions, as for our non-linear simulations in Chapter 3, we make use of a combination of both Fourier and finite difference methods.

2.3.3 Time-stepping

Euler Timestepping

Given a function which evolves continuously in time $\phi(t)$, with known value $\phi\left(t_0\right)$, one can approximate its value at some time $t_0+\Delta t$ for a small value of Δt by taking a Taylor series expansion. The value of $\phi\left(t\right)$ at $t_0+\Delta t$ can be approximated by

$$\phi(t_0+\Delta t)\approx\phi(t_0)+\Delta t\frac{\partial\phi}{\partial t}|_{t=t_0}. \tag{2.46}$$

Therefore, given the equation

$$\frac{\partial\phi}{\partial t}=f(t) \tag{2.47}$$

The quantity ϕ may be evolved by the equation

$$\phi(t_0+\Delta t)=\phi(t_0)+\Delta t f(t_0). \tag{2.48}$$

This method is referred to as the explicit Euler algorithm [78] and unless otherwise specified is used for the temporal evolution of most local terms in this thesis. In other cases we use the 4th order Runge-Kutte timestepping algorithm.

Runge-Kutte Timestepping

In certain cases where Euler timestepping is insufficient to ensure numerical stability or the timestep size Δt required by the Euler algorithm is too small to make a calculation numerically feasible, we make use of an semi-implicit Runge-Kutta method [78]. In order to timestep the system described in Eq. 2.47 with a stepsize Δt, the Runge-Kutta method defines the advance by the set of equations

$$\begin{aligned}
\phi(t_0 + \Delta t) &= \phi(t_0) + \frac{1}{6}(k_1 + k_2 + k_3 + k_4) \\
k_1 &= \Delta t f(\phi(t_0), t_0) \\
k_2 &= \Delta t f(\phi(t_0) + \frac{k_1}{2}, t_0 + \frac{\Delta t}{2}) \\
k_3 &= \Delta t f(\phi(t_0) + \frac{k_2}{2}, t_0 + \frac{\Delta t}{2}) \\
k_4 &= \Delta t f(\phi(t_0) + k_3, t_0 + \Delta t)
\end{aligned}$$

This makes the system of equations much more numerically stable, allowing for the use of larger timesteps, thereby reducing numerical cost.

2.4 Conclusion

This chapter has introduced some of the fundamentals which are relevant throughout this thesis. This includes hydrodynamics, rheology and flow instabilities. In the coming chapters, we study these topics theoretically using a variety of numerical methods, the essentials of which were also introduced here. This chapter discussed the concepts of non-Newtonian fluids and some of the different flow-curves which may categorise different rheological behaviour. We then explained how such fluids, as well as being non-Newtonian, often display elastic properties.

We then introduced the two types of flow instability of interest to us in this thesis. The first of these was the instability of a 1D base state to 2D perturbations. We discussed how if a base state is linearly unstable, infinitesimally small perturbations may grow exponentially to form secondary flows, thus leading to non-linear behaviour at large time-scales. The next instability of interest to us in this thesis is shear-banding, and we introduced both steady-state and transient shear-banding here.

Finally, we go through the various numerical techniques used in the studies conducted in this work. This acts as a background to the specific methods used in each chapter which are discussed in turn. With this prerequisite knowledge now in place, we move on to our first study: the linear instability of viscoelastic pressure driven channel flow.

Chapter 3

Linear Instability of Shear-Thinning Pressure-Driven Channel Flow

3.1 Introduction

The appearance of complex behaviour arising from initially simple flow is widely observed in many viscoelastic flows [53]. Unlike the case of many instabilities in Newtonian fluids, these instabilities may manifest in the creeping flow regime, where inertial effects are small. This behaviour is often found in flow geometries with curved streamlines, such as in Taylor-Couette flow [82], cone plate [83] and in plate-plate geometries [84]. Instabilities have also been studied in curved streamlines in a channel flow, both theoretically [85, 86] and in experiment [87, 88]. An examination of these instabilities in a range of geometries led to the development of a criterion based on the curvature of the streamlines and the Weissenberg number, Wi [89]. The Weissenberg number is defined as $Wi = \dot{\gamma}_c \tau_c$, where $\dot{\gamma}_c$ and τ_c are the characteristic shear-rate of the flow and viscoelastic relaxation time of the material respectively [90].

A great deal of research has also been conducted into instabilities that arise in geometries with straight streamlines. It has been found that an Oldroyd B fluid, which describes a viscoelastic fluid with constant viscosity, is stable to small amplitude perturbations in a Couette [91] and pressure driven Poiseuille flow [92]. Similar results were found for the Upper-Convected Maxwell fluid by Gorodtsov and Leonov in their analytical study of 1967 [93]. Studies into layered fluids have revealed instabilities to be widespread in flows with spatially varying viscoelastic properties. Instabilities in multi-fluid flow have been studied theoretically in both pressure driven Poiseuille flow [91, 94, 95] and Couette flow [96].

Shear-banded flows have also been shown to exhibit interfacial instability in both theoretical studies [97–99] and in experiment [100, 101]. These studies have demonstrated that instabilities in shear banded flows appear to be driven by large variations in normal stress differences and variations in shear-rate similar to those seen in flows of layered viscoelastic fluids. We discuss this similarity further in this chapter when we consider the nature of unstable channel flow in the Johnson-Segalman and Rolie-Poly models.

In this study we examine shear thinning viscoelastic fluids, which exhibit decreasing viscosity with increasing shear rate, but retain a monotonic flow curve and so do not have a shear-banded base state. In pressure driven flows instability was first predicted theoretically in this type of fluid by Wilson and Rallison performing linear stability analysis on such a system descibed using a White-Metzner model [14]. This model has the same form as the Upper-Convected-Maxwell model, but uses a shear-rate dependent relaxation time [102]. The relaxation time for this model is given by $\tau\left(\dot{\gamma}\right) = K_M\dot{\gamma}^{n-1}$, where n is the exponent controlling the degree of shear-thinning of the fluid, $\dot{\gamma}$ is the local frame invariant shear-rate and K_M is a constant of proportionality. The characteristic shear-rate for this study was determined by taking the flow velocity of the base state at the centre of the channel U_0 and dividing by the half channel width L. The Weissenberg number was then given by the the expression $Wi = K_M(U_0/L)^n$. They found that given a sufficiently high Weissenberg number and for sufficiently low shear-thinning exponent n, the calculated eigenvalues demonstrated the one-dimensional base state to be unstable to two dimensional perturbations along the flow direction. We replicate the basic results of this study in this chapter using a method of linear stability analysis novel to this work, and cast the results of this original study into a generalised framework for predicting the onset of instability.

Subsequent studies of shear thinning pressure driven channel flow performed by Grillet and collaborators using the Phan-Thien-Tanner (PTT) and Giesekus models [103] also found instability at sufficiently high Weissenberg numbers. The Weissenberg number at which instability was observed was found to depend on the degree of shear thinning of the model in question. In this study the characteristic shear rate is calculated by taking the average velocity in the base state divided by the half channel width. The authors found that the instability was predicted at all studied values of the anisotropic drag parameter, $0 < \alpha \leq 0.5$, using a Weissenberg number calculated from the wall shear-rate, $\dot{\gamma}_{wall}$ as opposed to the average shear-rate. The principal wavevector q^* in this study, which corresponds to the most unstable wavevector at the threshold of instability, was found to shift to lower wave-vectors with decreasing α. Previous studies of the Giesekus model performed by Blonce [104] and Lim and Schowalter [105] failed to find instability by only looking at the high wave-number regime. Instability to two-dimensional perturbations at small wavenumbers in the the Giesekus model was also observed in work by Palmer [106] with the addition of a solvent viscosity. In the PTT model Grillet's study found the trend to be different, with the critical wall Weissenberg number decreasing with non-linear relaxation parameter ϵ, but with non-monotonic variation in critical average Weissenberg number. This marked difference in behaviour between the models suggest that either the instabilities are unrelated or that some other means is necessary to characterise the onset of instability.

Later work by Bogaerds showed the eXtended Pom-Pom to be stable in pressure driven Poiseuille flow [107]. It was found that despite the model displaying strong shear thinning, the flow is stable to linear perturbations within the regime studied $Wi \sim \mathcal{O}(1)$. Their study also suggested that the presence of a second normal stress difference further stabilises the system to two dimensional perturbations. One can show that an incompressible, two dimensional flow field is not affected by second normal stress differences, therefore it is unclear why the presence of second normal stress difference should influence the flow stability.

Following over a decade of theoretical work, experimental evidence for instability of viscoelastic shear thinning channel flow was presented by Bodiguel et al. [18] and by Poole [19]. Both of these studies examined the stability of hydrolysed polyacrylamide (HPAC) solutions in two dimensional flow. They characterised the degree of shear thinning of the fluid by taking a power law fit of the shear thinning region of the flow curve, with all concentrations studied having shear thinning exponent $0.1 \leq n \leq 0.21$. Further examination of the fluids showed that unlike the original theoretical work by Wilson [14], a second shear thinning exponent on the shear modulus better modelled their rheology within the shear-thinning part of the shear-stress curve. The experimental design used by Bodiguel examined this instability at the micro-fluidic scale, while Poole used apparatus at larger scales thus mitigating the effects of slip. Two systems were studied by Poole to examine this instability, a channel and a circular pipe. The onset of instability was observed at similar flow rates in both geometries, suggesting that fluctuations in the vorticity direction may be unimportant to the emergence of instability. Poole also analysed the power spectrum of the flow at long timescales. He showed that the amplitude of the Fourier modes of velocity fluctuations followed a power-law distribution in the channel well beyond onset of instability. Both studies observe instability at a Weissenberg number similar to that predicted by Wilson's original work with the White-Metzner model ($Wi = 2$). Observed in these studies was the apparent increase in flux through the pipe after the onset of instability. This phenomenon has since been observed in other experiments of viscoleastic turbulent channel flow at low Reynold's number [108, 109]. Another experimental observation of instability in a similar geometry was in extruded flow of a shear-thinning sodium alginate solution [20]. In this study a helical gyration of the extruded fluid above some critical flow rate was observed at a critical Weissenberg number similar to those seen by other experimental studies, but for a higher shear-thinning exponent ($n = 0.3$). More recent work examining the instability of shear-thinning viscoelastic solutions of polyethylene glycol in microtubials has examined the onset of turbulence at very high elasticity numbers, the ratio of elastic to inertial effects in the flow, El [110]. Their findings showed that with increasing polymer concentration, the threshold Reynolds number for instability decreased. From this they inferred that the instability is primarily elastic in origin.

In order to examine this work further, Wilson and collaborators studied the stability of a modified White-Metzner model, using both a shear thinning relaxation time, described by the expression $\tau(\dot{\gamma}) = K_M \dot{\gamma}^{n-1}$ and shear-modulus $G(\dot{\gamma}) = G_M \dot{\gamma}^{m-n}$ [15]. The special case of $m = n$ corresponds to the model used in the original study by Wilson and Rallison. In this new model the fluid was found to be most unstable near the parameters which best fit the experimentally studied fluid ($n = 0.2$, $m = 0.43$). However the model predicted that the unstable modes would be *varicose*, symmetric within the channel, as in the original theoretical study. In experiments however *sinuous*, anti-symmetric, modes are observed. Following this work, another modification was made [16], this time with the inclusion of a shear-thinning inelastic solvent, such that the flow curves of shear stress and first normal stress difference are described by

$$\Sigma(\dot{\gamma}) = G\tau^m \dot{\gamma}^m + \mu \dot{\gamma}^m \tag{3.1}$$

$$N_1(\dot{\gamma}) = 2G\tau^{m+n} \dot{\gamma}^{m+n}. \tag{3.2}$$

This study showed the flow to become more stable with increasing solvent viscosity coefficient μ suggesting the instability is primarily of elastic origin, i.e. that shear-thinning alone without viscoelasticity is not sufficient to give instability. In both this study, and in that performed without the addition of solvent there is an unusual behaviour observed when $m = n$. The stability of the flow drops suddenly as m approaches the value of n from either direction. This sudden change in stability, as well as the absence of unstable sinuous modes, suggest that White-Metzner type models cannot capture a completely physically accurate description of channel flow behaviour.

The most recent theoretical study of shear thinning channel flow, also by Castillo and Wilson [17], used the Bautista-Manero-Puig fluidity model. The form of this model is quite different from others studied so far [111]. Since the stress evolution is modelled by a conventional UCM equation, the normal stress profile is always parabolic. By varying the model parameters the authors were able to determine the influence of thixotropy on the instability, and find that the thixotropic timescale does not affect the sign of the unstable eigenvalue, only its magnitude, which increases as the fluid becomes less thixotropic. It was found in this study that the most unstable eigenvalues are found for wavenumbers $0.35 < q < 0.6$, much lower than seen in their previous work with the White-Metzner model. The authors also showed that the position of the shear thinning regime within the channel influences the stability of the flow, with the eigenvalue increasing as the region of shear thinning moves close to the wall. This suggests that the onset of instability may be linked to the underlying base state.

In this study, we characterise the onset of this instability in several models to determine the possible generality of instability of shear-thinning pressure driven flow in models of shear-thinning viscoelastic fluids to two dimensional perturbation. We perform this study within a number of constitutive models widely used to describe the evolution of viscoelastic stress. In partiular we consider the microscopically motivated non-stretch Rolie-Poly (RP) model [112] and the phenomenological Johnson-Segalman (JS) [113] and White-Metzner (WM) [102] models. Using linear stability analysis, we calculate the threshold imposed pressure drop for the onset of instability in each model as a function of the model parameters. From this we determine a general functional form based on the steady state flow curves which predicts the onset of instability in each of the models studied based on the underlying steady state shear-stress $\Sigma\left(\dot{\gamma}\right) = \sigma_{xy}\left(\dot{\gamma}\right) + \eta\dot{\gamma}$ and first normal stress difference $N_1\left(\dot{\gamma}\right) = \sigma_{xx}\left(\dot{\gamma}\right) - \sigma_{yy}\left(\dot{\gamma}\right)$ flow curves. We also analyse and discuss how the linear behaviour may offer insight into how instability manifests itself across apparently dissimilar models. We observe instability in each model below some critical logarithmic slope of the flow curve at its shallowest point, $n = \frac{d\log\Sigma}{d\log\dot{\gamma}}|_{min}$. We demonstrate that the critical pressure drop for the onset of instability is well described by a criterion expressed in terms of the degree of shear-thinning n, and the maximum value of the derivative within the channel of the first normal stress difference with respect to shear-stress $\frac{dN_1}{d\Sigma}|_{max}$. In the case of the Rolie-Poly and Johnson-Segalman models, we perform non-linear simulations to observe long-timescale behaviour. The observation of instability in the Rolie-Poly and Johnson-Segalman models is novel to this study as far as this author is aware. We also reproduce the basic findings of the work of Ref. [14], and demonstrate that instability in the WM model can be predicted by the same functional form as in the case of the RP and JS.

Characterising Pressure Driven Flow

Weissenberg numbers are used widely to characterise the onset of instability in viscoelastic fluids, including in channel flow as is of interest here. In the original work of Wilson and collaborators [14], the Weissenberg number was defined by considering the average shear-rate across the channel, such that

$$Wi = K_M (U_0(0)/L)^n. \tag{3.3}$$

Here K_M is the relaxation time coefficient such that $\tau\left(\dot{\gamma}\right) = K_M \dot{\gamma}^{n-1}$, $U_0(0)$ is the velocity at the centre of the channel and L is the channel halfwidth. The flow profile $U_0(y)$ can be calculated analytically, thereby allowing the pressure drop P' to be selected such that the centreline velocity is 1. The stability is then assessed by varying Weissenberg number for a given model parameter n by varying K_M.

In the work of Grillet and collaborators in Refs. [103, 107] the average velocity in the channel, $< U(y) >$, divided by the channel halfwidth, is used to obtain a characteristic shear-rate. Poole used this definition in his experimental study, with the average velocity taken from the velocimitry data within the channel. Grillet separately defined a wall Weissenberg number (taken as the wall shear-rate multiplied by the relaxation time τ) to characterise the flow.

In the experimental studies in Ref. [18, 20], the Weissenberg number is defined from the flow curves as

$$Wi = \frac{N_1(\dot{\gamma}_{wall})}{\Sigma(\dot{\gamma}_{wall})}. \tag{3.4}$$

All of these definitions seek to characterise the onset of instability by defining for a pressure driven flow a characteristic shear-rate in the channel. We choose in this study not to define a Weissenberg number and instead relate the onset of instability to the applied pressure drop P'.

Critical Pressure Drop

In this study we are motivated to define the onset of instability by using the quantities readily available to experimentalists. Included in this are the steady-state shear-stress curves, first normal stress difference curves and the applied average pressure drop along the channel. We show in this chapter that these quantities may predict the stability properties of a 1D base state to two-dimensional perturbations in pressure driven channel flow. We do not utilise a Weissenberg number to characterise the onset of instability in our study, but the critical pressure drop P'^{*}. This acts to the same effect as the Weissenberg number, since it characterises the strength of the flow, but also offers key insights into how the steady state rheology of the fluid in question presents itself in the channel.

We note firstly that force balance requires the total shear stress to vary across the channel as $\Sigma = P'y$ for a 1D flow. The magnitude of the wall shear stress in the channel (in the 1D base state) is determined by the applied pressure gradient in the channel P' via the relation $\Sigma = P'L_y/2$, where L_y is the channel-width. The shear-rate between the centre of the channel and the wall is then set by the homogeneous shear-stress curve $\Sigma\left(\dot{\gamma}\right)$. This value of shear-rate as a function of position $\dot{\gamma}\left(y\right)$ is set by the inverse function of the flow curve $\dot{\gamma}\left(\Sigma = P'y\right)$. We shall see this when come to examine more closely the flow curves and base states of each model in this chapter.

As well as determining the base-state profile, other important quantities are set by the applied pressure drop. The variation of the first normal stress-difference and shear-rate within the channel are then given by

$$\frac{dN_1}{dy} = \frac{d\Sigma}{dy}\frac{dN_1}{d\Sigma} = P'\frac{dN_1}{d\dot{\gamma}}/\frac{d\Sigma}{d\dot{\gamma}}. \tag{3.5}$$

and

$$\frac{d\dot{\gamma}}{dy} = \frac{d\Sigma}{dy}\frac{d\dot{\gamma}}{d\Sigma} = P'\frac{d\dot{\gamma}}{d\Sigma}. \tag{3.6}$$

respectively. We shall see that these quantities, combined with the shear-thinning nature of the fluid, leads to the instability of the base state to two dimensional perturbations.

3.2 Flow Geometry

The flow considered is between two infinite flat parallel static boundaries, at which we impose boundary conditions of no-slip and no-permeation. These boundaries are set at $y = +L_y/2$ and $y = -L_y/2$, and throughout we work in units of length such that the channel width $L_y = 1$. The flow is driven along the channel in the positive $\hat{\mathbf{x}}$ direction by a constant negative applied pressure gradient per unit length, P' which we measure in units of G/L_y, where G is the shear-modulus of the fluid. The flow is assumed to remain translationally invariant in the vorticity direction $\hat{\mathbf{z}}$, with zero velocity component in $\hat{\mathbf{z}}$. (These assumptions are in accordance with Squire's theorem, which holds that a shear flow of the form $\mathbf{v} = (U_0(y), 0, 0)$ is less stable to two-dimensional perturbations of the form $\tilde{\mathbf{v}} = (\tilde{u}(x, y, t), \tilde{v}(x, y, t), 0)$ rather than to three-dimsensional perturbations [114]. This should be checked in future fully 3D studies in order to consider the potential influence of second normal stress differences [115].) The numerical methods used to simulate this system are outlined in Appendix I of this chapter.

3.3 Models

Many different constitutive models are used by rheologists to describe the dynamics of polymeric fluids [47]. These may be phenomenologically motivated, such as White-Metzner [102] and Johnson-Segalman [113] or developed based on molecular dynamics, such as the GLaMM [116], Rolie-Poly [112] or Pom-Pom model [117].

We make use of three constitutive models to study the stability of an initially 1D shear-thinning channel flow profile to two dimensional perturbations. These are the Rolie-Poly, Johnson-Segalman and White-Metzner models. In addition to the viscoelastic or polymeric stress that is described by each of the models, we also include a Newtonian solvent. This is due to several reasons motivated by the physical properties of the fluids we seek to study and in order to facilitate our calculations. As we see in Figure 3.1 for the Johnson-Segalman model, some constitutive models display sufficient shear-thinning such that the shear stress curve becomes non-monotonic. This may also occur in the Rolie-Poly model. With the addition of a Newtonian solvent stress $\eta\dot{\gamma}$ to the polymeric stress σ_{xy}, the total shear stress Σ is monotonic. As discussed in Chapter 2, this non-monotonic constitutive curve is linked to the formation of shear-bands. The stability of such a shear banded flow was studied for pressure driven channel flow in Ref. [118]. In this study we restrict ourselves to non-banded flows. Therefore we include for each model a solvent component to the stress, with solvent viscosity such that the flow curve is monotonic. The addition of a solvent viscosity also allows us to calculate the resulting flow field via the Stokes equation. The methods used for this are described in detail in Appendix I of this chapter.

An important feature of these models is their steady state rheology. In the case of shear flow, this refers to the values of shear-stress (shear rate) obtained due to an imposed shear rate (shear stress) following the subsidence of transient dynamics. This is an extremely important means by which experimentalists characterise the properties of complex fluids, and theoretical constitutive curves are often fitted to experimentally measured data for the purposes of simulating complex flow behaviour. In each of the models used we focus strongly on the steady state behaviour in each of the models used and show how the properties of the flow curves relate to the onset of instability.

Although the Oldroyd B model is not used in this study, both the Johnson-Segalman and White-Metzner models are equivalent to the Oldroyd B model for some values of their rheological parameters. It is therefore beneficial that we introduce it here. We shall now introduce each of the models used in this study, as well as the Oldroyd B model. For comparison purposes, the steady state constitutive curves of the four models are plotted together in Figure 3.2.

3.3.1 The Oldroyd B model

We do not study explicitly the stability of an Oldroyd B fluid in pressure driven channel flow, because this model has been found to be linearly stable to perturbations in previous work examining pressure driven channel flow [92,119]. We however make reference to Oldroyd B frequently as two of the models used in this study (Johnson-Segalman and White-Metzner) recover Oldroyd B dynamics at some value

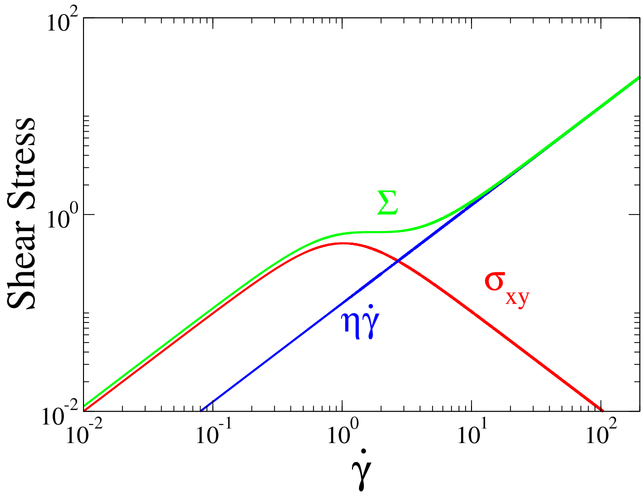

Figure 3.1: The polymeric stress σ_{xy}, Newtonian solvent stress $\eta\dot{\gamma}$ and total shear stress $\Sigma = \sigma_{xy} + \eta\dot{\gamma}$ plotted as a function of applied shear-rate $\dot{\gamma}$ for the Johnson-Segalman model with parameters $a = 0.2$ and $\eta = 0.125$.

of their rheological parameters. The model is motivated here using a kinetic theory approach, i.e, an approach in which the elements of a constitutive model can be defined in terms of molecular properties.

The Oldroyd B constitutive equation models each polymer chain as a dumbbell, two beads connected by a linear elastic spring [120]. The displacement between beads, known as the end-to-end vector, is denoted $\mathbf{R}$. The polymer chains are in a solvent with viscosity η. The model considers the dilute limit where interactions between the polymers can be neglected and only interactions between the polymer and the solvent are important. The polymer stress tensor σ is calculated by considering the dumbbells crossing a small surface element δS of unit normal $\mathbf{n}$. If the force on a single dumbbell is proportional to the magnitude of $\mathbf{R}$, then the polymer stress exerted by the dumbbells crossing the surface element is given by

$$\sigma = G \langle \mathbf{RR} \rangle = G(\mathbf{W} - \mathbf{I}). \tag{3.7}$$

Here $\langle ... \rangle$ denotes the ensemble average and $\mathbf{W}$ is defined as the conformation tensor which describes the configuration of polymer chains under deformation. For an elastic dumbbell in a solvent, there are three forces acting upon it: the viscous drag, the elastic spring force and a random Brownian force. It is assumed that the centre of mass of the dumbbell moves with the velocity of the solvent at that position. One can therefore show by considering these effects that the evolution of the conformation tensor in a flow field $\mathbf{v}$ obeys the equation

$$\partial_t \mathbf{W} + \mathbf{v}\nabla \cdot \mathbf{W} = \nabla\mathbf{v}\mathbf{W} + \mathbf{W}\nabla\mathbf{v}^T - \frac{1}{\tau}(\mathbf{W} - \mathbf{I}). \tag{3.8}$$

Here τ is the relaxation time of the polymer stress. Without a solvent contribution to the stress (which we have assumed for all models in this study), this equation also describes the evolution of the Upper-Convected-Maxwell model [47].

The homogeneous shear stress and first normal stress difference curves are given as a function of shear-rate by the expressions

$$\Sigma = G\tau\dot{\gamma} + \eta\dot{\gamma} \tag{3.9}$$

and

$$N_1 = 2G\tau^2\dot{\gamma}^2 \tag{3.10}$$

respectively. As we can see, the Oldroyd B model describes a constant viscosity viscoelastic fluid, or Boger fluid [49]. This can be used describe low concentration polymeric fluids which may display minimal shear-thinning. In Figure 3.2 we see that for low shear-rates both the shear-stress and first normal stress difference in the Johnson-Segalman and Rolie-Poly models behave as for Oldroyd B. At higher shear-rates we see that shear-thinning effects become more pronounced and their behaviour diverges.

3.3.2 Johnson-Segalman Model

The Johnson-Segalman (JS) model is a spring and dumbell model closely related to the Oldroyd B model [113], but extends it by introducing a "slip parameter" a, which controls how the dumbbells can deform in a non-affine way relative to the background flow field. The dynamic equation of the stress tensor is then

$$\partial_t \mathbf{W} + \mathbf{v} \cdot \nabla\mathbf{W} = (\mathbf{\Omega}\mathbf{W} - \mathbf{W}\mathbf{\Omega}) + a(\mathbf{D}\mathbf{W} + \mathbf{W}\mathbf{D}) - \frac{1}{\tau}(\mathbf{W} - \mathbf{I}). \tag{3.11}$$

Here $\mathbf{D} = \frac{1}{2}(\nabla\mathbf{v} + \nabla\mathbf{v}^T)$ and $\mathbf{\Omega} = \frac{1}{2}(\nabla\mathbf{v} - \nabla\mathbf{v}^T)$ are the symmetric and anti-symmetric part of the rate of strain tensor respectively.

For $a = 1$ the deformation of the dumbbells is purely affine with the background flow, and the Oldroyd B model is recovered. For $|a| < 1$ the steady state polymeric stress is a non-monotonic function of shear-rate. In this study we set the solvent viscosity $\eta > G\tau/8$ to ensure that the constitutive curve remains monotonic. This leads to a much higher value of solvent viscosity being used in our calculations for JS compared to others in our study. In Figure 3.2 a) we see that this leads to a more pronounced high-shear rate Newtonian regime than for the other models shown. The analytical form of the steady state shear stress as a function of shear flow for a state of stationary homogeneous shear is given by

$$\Sigma(\dot{\gamma}) = \frac{G\tau\dot{\gamma}}{1 + (1 - a^2)\tau^2\dot{\gamma}^2} + \eta\dot{\gamma}, \tag{3.12}$$

where η is the Newtonian solvent viscosity. The corresponding steady state first normal stress difference is given by

$$N_1(\dot{\gamma}) = \frac{2G\tau^2\dot{\gamma}^2}{1 + (1 - a^2)\tau^2\dot{\gamma}^2}. \tag{3.13}$$

A limitation of the Johnson-Segalman model is its tendency to give unphysical transient behaviour at high shear rates, leading to high frequency oscillations of the start-up curve values. Our focus in this study is on the impact of the steady state behaviour on secondary flow and does not relate to this transient behaviour. We therefore deem it to be a suitable model for use in this study.

As stated previously, at low shear-rates the flow curve of the Johnson-Segalman model will be equivalent to that for Oldroyd B. For shear-rates $\dot{\gamma} \gtrsim \frac{1}{\sqrt{1 - a^2}}$, the model displays very strong shear-thinning. At higher shear-rates the solvent stress dominates and the flow curve displays a high shear-rate Newtonian regime also seen in polymer solutions, such as those used in the experiments of Ref. [18]. When we examine the flow curve of first normal stress difference, we again see in Figure 3.2 b) that at low shear-rates the model imitates Olrdoyd B. At higher shear-rates however, the first normal stress difference ceases to grow quadratically with the applied shear-rate and saturates. While the Johnson-Segalman model is a phenomenological model, we see that many of its features are also observed in the molecularly motivated Rolie-Poly model.

3.3.3 Rolie-Poly Model

The modelling of fluids composed of entangled polymers - a chain of repeating monomer units - is often done by considering a single polymer molecule which is constrained by a mean field of entanglements with other polymers. It was proposed by Edwards [121] that this creates a tube of confinement around the chain, the contour of which approximates a random walk with step size equal to the tube diameter. This random walk is called the primitive path, the contour length of which is much less than the chain itself [38]. De Gennes suggested that the polymer would thereafter diffuse along its length and escape the constraints of the tube. This process was termed "reptation" due to its similarity to the motions of a snake. The Doi-Edwards model [122] was among the first of these tube-like models which was widely used successfully to model polymeric fluids.

The theory did not however incorporate the relaxation mechanism of convective constraint release (CCR), which describes how the constraints on a polymer can be lost due to neighbouring polymers themselves reptating through points of entanglement [123]. The theory also did not allow for chain stretch during strongly nonlinear flows with deformation rates approaching the inverse Rouse time $\dot{\gamma} \approx \tau_R^{-1}$. Chain stretch denotes the effects of elongational displacement of the polymer chains. τ_R is the Rouse relaxation time, which corresponds to the timescale on which the chain stretch relaxes. The GLAMM model [116] was developed from the original Doi-Edwards tube model to incorporate such mechanisms. It provides a stochastic microscopic equation of motion for the chain and the surrounding tube. It is however highly intensive computationally, and so a single mode approximation to GLAMM was derived. This single mode approximation is the Rolie-Poly (ROuse LInear Entangled POLYmers or "RP") model [112]. The stress tensor in the Rolie-Poly model is defined such that $\sigma = G\mathbf{W}$, where $\mathbf{W}$ is the microscopic viscoelastic conformation tensor. The constitutive equation for the viscoelastic conformation tensor of this model is given by

$$\partial_t \mathbf{W} + \mathbf{v} \cdot \nabla \mathbf{W} = \nabla \mathbf{v} \cdot \mathbf{W} + \mathbf{W} \cdot \nabla \mathbf{v}^T - \frac{1}{\tau_d} (\mathbf{W} - \mathbf{I}) - \frac{2(1-A)}{\tau_R} \left[\mathbf{W} + \beta A^{-2\delta} (\mathbf{W} - \mathbf{I}) \right], \tag{3.14}$$

where $A = \sqrt{3/T}$ and $T = \mathrm{tr}(\mathbf{W})$ denotes the magnitude of the chain stretch in the system. The timescale τ_d is the "reptation" time, defined as the timescale on which the polymer chain escapes the tube of entanglements along which it undergoes diffusion along its own length. τ_d and τ_R are related via the number of entanglements of the polymer Z, where

$$Z = \frac{\tau_d}{3\tau_R}. \tag{3.15}$$

In this study we make use of the highly entangled limit, where $Z \to \infty$, such that $\tau_R = \tau_d/Z \to 0$ This yields the non-stretch version of the Rolie-Poly model, as the timescale for the polymers to relax from displacement along their own length is infinitely less than the corresponding timescale of reptation. This has the constitutive equation

$$\partial_t \mathbf{W} + \mathbf{v} \cdot \nabla \mathbf{W} = \nabla \mathbf{v} \cdot \mathbf{W} + \mathbf{W} \cdot \nabla \mathbf{v}^T - \frac{1}{\tau} (\mathbf{W} - \mathbf{I}) - \frac{2}{3} \mathrm{Tr}(\nabla \mathbf{v} \cdot \mathbf{W}) \left[\mathbf{W} + \beta(\mathbf{W} - \mathbf{I}) \right]. \tag{3.16}$$

Here β is the convective constraint release parameter which describes the number of constraint release events required to result in some portion of the tube moving a distance of the tube parameter. We drop the subscript, writing simply $\tau = \tau_d$, which is then the characteristic timescale for our study with this model.

Unlike the other models used in this study, the Rolie-Poly model lacks a known analytical expression for its steady state behaviour. We see in Figures 3.2 a) and b) that many features of the steady state rheology of the Rolie-Poly are similar to those of Johnson-Segalman. In the shear stress curve we observe a low shear-rate Oldroyd B like regime, a shear-thinning plateau, and high shear-rate Newtonian behaviour. Likewise, we see that at low shear-rates that $N_1 \sim \dot{\gamma}^2$ before saturating at higher shear-rates. These similarities will become significant when we come to describe the influence of the flow curves on how channel flow instability manifests in each model. These features are, however, lacking in the next model we introduce.

3.3.4 White-Metzner Model

The White-Metzner model uses an Upper-Convected-Maxwell type equation with a relaxation time τ set as a function of the frame invariant shear-rate [102]. The constitutive equation is then given by

$$\partial_t \mathbf{W} + \mathbf{v} \cdot \nabla \mathbf{W} = \nabla \mathbf{v} \mathbf{W} + \mathbf{W} \nabla \mathbf{v}^T - \frac{1}{\tau(\dot{\gamma})}(\mathbf{W} - \mathbf{I}). \tag{3.17}$$

Here $\tau(\dot{\gamma}) = \tau^n \dot{\gamma}^{n-1}$ where $\dot{\gamma}$ is the frame invariant shear-rate defined as

$$\dot{\gamma} = \sqrt{2\mathbf{D} : \mathbf{D}}, \tag{3.18}$$

where $\mathbf{D}$ is the symmetric rate of strain tensor previously defined. The power law index $0 < n \leq 1$ gives shear-thinning for $n < 1$.

The steady state flow curves of shear-stress and first normal stress difference are described for the White-Metzner model respectively by

$$\Sigma = G\tau\dot{\gamma}^n + \eta\dot{\gamma}. \tag{3.19}$$

and

$$N_1 = 2G\tau\dot{\gamma}^{2n}. \tag{3.20}$$

We see in Figures 3.2 a) that this leads to very different behaviour from other models in this study. We note that the White-Metzner model gives shear-thinning power law fluid behaviour even in the limit $\dot{\gamma} \to 0$, thereby not displaying any Newtonian regime at low shear-rates. This is unlike the other models studied in this chapter. Therefore caution is needed if this model is to be applied to the simulation of experimental polymeric solutions in channel flow, as is our concern here, because near the centre of the channel low shear-rates will always be observed. By symmetry, the base state shear-rate is always zero along the channel centreline. The behaviour of N_1 is also quite different in this model. We see neither the low shear-rate $\dot{\gamma}^2$ dependence nor the high shear-rate saturation.

Within the White-Metzner model an initially 1D base state of a pressure driven flow was found to unstable to perturbations originally in Ref. [14]. In this study we seek to understand this already known instability in the context of other models we have studied. By making direct comparison with previous studies we also seek to validate the novel method we have used to perform linear stability analysis. Unlike in the prior study, we require the addition of a solvent viscosity to calculate the flow field, which introduces minor differences to the base state.

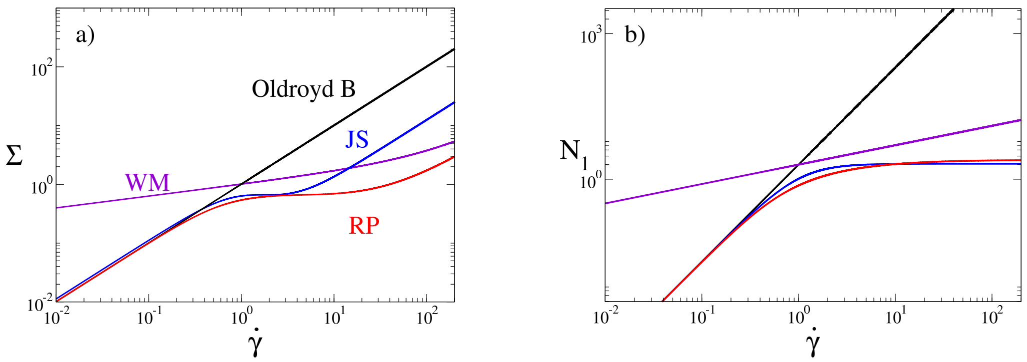

Figure 3.2: 1 Constitutive curves of a) shear-stress and b) first normal stress difference for the Oldroyd B, Johnson-Segalman (JS), Rolie-Poly (RP) and White-Metzner (WM). The model parameters are Oldroyd B:$\eta = 0.0125$. Johnson-Segalman: $a = 0.2$, $\eta = 0.125$. Rolie-Poly: $\beta = 0.2$, $\eta = 0.0125$. White-Metzner:$n = 0.2$, $\eta = 0.0125$.

3.4 Model Parameters and units

We report all results in this chapter in units of length in which the channel width $L_y = 1$; units of stress in which the polymeric shear modulus $G = 1$; units of time in which the basic polymeric relaxation timescale $\tau = 1$. In the case of the White-Metzner model the polymeric relaxation time is a function of the frame invariant shear-rate $\dot{\gamma} = \sqrt{2\mathbf{D} : \mathbf{D}}$ such that $\tau(\dot{\gamma}) = \tau_0^n \dot{\gamma}^{n-1}$. Therefore the time unit for this model is defined in terms of this coefficient τ_0.

In these units we need only consider four parameters for each model. The first of these is the model parameter controlling the viscoelastic behaviour of the model in question: the CCR parameter β for Rolie-Poly, the slip parameter a for Johnson-Segalman and the power law exponent n for the White-Metzner model. The second parameter in the Newtonian background solvent viscosity which is always small on the scale of the polymeric viscosity $G\tau = 1$. The third is the channel length L_x. Our linear stability analysis calculates the growth rate of perturbations as a continuous function of the magnitude of the wavevector $q\hat{\mathbf{x}}$. However in reality this is quantised as $q = 2\pi q^{'}/L_x$ for any channel of finite length L_x. In non-linear simulations L_x is an explicit parameter. The last parameter which we vary in this study is the imposed pressure drop, P', which characterises the strength of the imposed flow.

3.5 Linear Stability Analysis

We now outline the method by which the linear stability analysis was conducted in this study. Credit for derivation of this method is given to Professor Suzanne Fielding.

By using linear stability analysis, we aim to determine the stability of an initial 1D base state to a perturbation with some wavevector $q\hat{\mathbf{x}}$. All the constitutive models used in this study have the same basic form outlined as follows. The total stress is given by

$$\mathbf{\Pi} = \sigma + 2\eta\mathbf{D} - p\mathbf{I}, \tag{3.21}$$

where the viscoelastic stress $\sigma = \sigma(\mathbf{W})$. Within the zero Reynolds number flow regime, force balance requires:

$$\nabla \cdot \mathbf{\Pi} = 0, \tag{3.22}$$

and the condition of incompressibility gives:

$$\nabla \cdot \mathbf{v} = 0. \tag{3.23}$$

The constitutive equations used to model the evolution of the conformation tensor $\mathbf{W}$, and hence the viscoelastic stress tensor σ, are all of the general form

$$\frac{\partial \mathbf{W}}{\partial t} + \mathbf{v} \cdot \nabla \mathbf{W} = F\left(\mathbf{W}, \nabla \mathbf{v}, \xi\right). \tag{3.24}$$

Here ξ is a model parameter controlling the rheology of the model. This parameter varies depending on the model in question, with $\xi = n$ in White-Metzner, $\xi = a$ in Johnson-Segalman and $\xi = \beta$ in Rolie-Poly. These equations must be solved subject to a constant imposed average pressure gradient P' per unit length in $\hat{\mathbf{x}}$.

In order to study the instability of the flow to two dimensional perturbations, we first must calculate a one dimensional stationary solution to Eqs. 3.21-3.24. This is done by evolving the equations numerically to steady state, allowing spatial variation only in the $\hat{\mathbf{y}}$ direction. We denote the base state as

$\mathbf{v}_0(y), \mathbf{W}_0(y), \sigma_0(y), p_0(y), \mathbf{\Pi}_0(y)$. The base state is therefore defined such that

$$0 = \eta\nabla^2\mathbf{v}_0 + \nabla\cdot\sigma_0 - P'\hat{\mathbf{x}} \tag{3.25}$$

$$0 = F(\mathbf{W}_0, \nabla\mathbf{v}_0, \xi). \tag{3.26}$$

These quantities each depend on ξ and η, but these dependencies are dropped for ease of notation. The base state velocity $\mathbf{v}_0$ is non-zero only in the $\hat{\mathbf{x}}$ direction, such that $\mathbf{v}_0(y) = U_0(y)\hat{\mathbf{x}}$, where $U_0(y)$ is the magnitude of the base state velocity field.

In order to study the linear stability of a 1D base state, we apply small perturbations to the base state of the form,

$$\sigma(x,y,t) = \sigma_0(y) + \tilde{\sigma}_q(y)e^{iqx+\omega_q t} \tag{3.27}$$

$$p(x,y,t) = p_0(y) + \tilde{p}_q(y)e^{iqx+\omega_q t} \tag{3.28}$$

$$\mathbf{v}(x,y,t) = \mathbf{v}_0(y) + \tilde{\mathbf{v}}_q(y)e^{iqx+\omega_q t}, \tag{3.29}$$

$$\mathbf{\Pi}(x,y,t) = \mathbf{\Pi}_0(y) + \tilde{\mathbf{\Pi}}_q(y)e^{iqx+\omega_q t} \tag{3.30}$$

$$\mathbf{W}(x,y,t) = \mathbf{W}_0(y) + \tilde{\mathbf{W}}_q(y)e^{iqx+\omega_q t} \tag{3.31}$$

The eigenvalue ω_q then describes the temporal evolution of the perturbation for a given wavenumber q. The perturbations $\tilde{\mathbf{v}}_q(y), \tilde{\mathbf{W}}_q(y), \tilde{\sigma}_q(y), \tilde{p}_q(y), \tilde{\mathbf{\Pi}}_q(y)$ develop into the eigenfunctions corresponding to the most unstable eigenvalue for the given wavenumber q. Therefore, when a perturbation is added to the constitutive equation we obtain

$$\begin{aligned}\omega_q\tilde{\mathbf{W}}_q e^{iqx+\omega_q t} + (\mathbf{v}_0 + \tilde{\mathbf{v}}_q e^{iqx+\omega_q t})\cdot\nabla(\mathbf{W}_0 + \tilde{\mathbf{W}}_q e^{iqx+\omega_q t}) = \\ F(\mathbf{W}_0 + \tilde{\mathbf{W}}_q e^{iqx+\omega_q t}, \nabla\mathbf{v}_0 + \nabla\tilde{\mathbf{v}}_q e^{iqx+\omega_q t}, \xi).\end{aligned} \tag{3.32}$$

Expanding in powers of the amplitude of perturbation, retaining only terms of first order in that amplitude, and multiplying across by $e^{-iqx-\omega_q t}$ we obtain a set of linearised equations that govern the dynamics of the perturbations. In the linear regime, where perturbations remain small, these equations are valid and the q-modes evolve independently of each other. In this study the main quantities of interest are, for each value of q, the eigenvalue ω_q with the largest real part and the corresponding eigenfunction $\tilde{\mathbf{v}}_q(y), \tilde{\mathbf{W}}_q(y), \tilde{\sigma}_q(y), \tilde{p}_q(y), \tilde{\mathbf{\Pi}}_q(y)$. The sign of the real part of the eigenfunction $Re(\omega_q)$ determines whether the mode with corresponding eigenfunction grows or decays. A positive value $Re(\omega_q) > 0$ signifies the one dimensional base state to be linearly unstable to two dimensional perturbations $\propto \exp(iqx)$, while the converse is true if $Re(\omega_q) < 0$. If $Re(\omega_q) < 0$ for all modes, the base state is linearly stable against all such perturbations.

The fully linearised method outlined above is an exact method for calculating the eigenmodes of the instability. In practice however, it is rather cumbersome. Instead we use the following semi-linearised equation to describe the evolution of a single mode q, which gives the following form

$$\partial_t\tilde{\mathbf{W}}_q+iqU_0\tilde{\mathbf{W}}_q+\tilde{u}_q iq\mathbf{W}_0+\tilde{v}_q\partial_y\mathbf{W}_0 = F\left(\mathbf{W}_0+\tilde{\mathbf{W}}_q, \nabla\mathbf{v}_0 + e^{-iqx-\omega_q t}\nabla\tilde{\mathbf{v}}_q e^{iqx+\omega_q t}, \xi\right). \tag{3.33}$$

Here $\tilde{u}_q(y)$ and $\tilde{v}_q(y)$ are the magnitude of perturbation to the flow field in the $\hat{\mathbf{x}}$ and $\hat{\mathbf{y}}$ directions respectively. Note that the advective terms in Eq. 3.33 are linearised while the rest are left in non-linear form. While the perturbations remain small, this method is equivalent to the fully linearised form. The perturbation to the velocity field is of the form

$$\tilde{\mathbf{v}}_q e^{iqx+\omega_q t} = \begin{pmatrix} \tilde{u}_q(y) \\ \tilde{v}_q(y) \end{pmatrix} e^{iqx+\omega_q t}. \tag{3.34}$$

The perturbation rate of strain tensor $\nabla\tilde{\mathbf{v}}_q e^{iqx}$ is then given by

$$\nabla\tilde{\mathbf{v}}_q e^{iqx+\omega_q t} = \begin{pmatrix} \partial_x u_q(y)e^{iqx+\omega_q t} & \partial_x v_q(y)e^{iqx+\omega_q t} \\ \partial_y u_q(y)e^{iqx+\omega_q t} & \partial_y v_q(y)e^{iqx+\omega_q t} \end{pmatrix}. \tag{3.35}$$

Multiplying through by $e^{-iqx-\omega_q t}$ yields

$$e^{-iqx-\omega_q t}\nabla\tilde{\mathbf{v}}_q e^{iqx+\omega_q t} = \begin{pmatrix} iq\tilde{u}_q(y) & iq\tilde{v}_q(y) \\ \partial_y\tilde{u}_q(y) & \partial_y\tilde{v}_q(y) \end{pmatrix} \tag{3.36}$$

The force balance equation of the perturbation flow field $\tilde{\mathbf{v}}_q$ is given by

$$\eta\nabla^2\tilde{\mathbf{v}}_q + \nabla\cdot\tilde{\sigma}_q - \nabla\tilde{p}_q = 0. \tag{3.37}$$

Into these equations we substitute the stationary base state for $\sigma_0(y)$ and $\mathbf{v}_0(y)$ calculated above and initialise the system with small amplitude spatially random perturbations of $\tilde{\sigma}_q(y), \tilde{\mathbf{v}}_q(y)$ before evolving the semi-linearised equations with time. The amplitude of the perturbation at any time t is then given by

$$|\tilde{\sigma}_q| = \frac{1}{4}\sum_{i=1}^{2}\sum_{j=1}^{2}\int_{-L_y/2}^{L_y/2} |\tilde{\sigma}_{ij}| dy. \tag{3.38}$$

The value of $Re(\omega_q)$ is then calculated by taking the slope the growth of $\log(|\tilde{\sigma}_q|)$ with respect to time. By performing this calculation over a range of wavevectors the growth rate of the perturbations as a function of q, or *dispersion relation* is calculated. The *stability threshold* for a given set of values of ξ and η is the value of P' for which the largest real part of any eigenvalue $Re\,(\omega_q) = 0$ for some value q. $Im\,(\omega_q)$ describes the advection of the perturbations along the channel and does not relate to the stability of the mode and as such is not reported here. The calculated functions $\tilde{\sigma}_q(y)$ and $\tilde{\mathbf{v}}_q(y)$ correspond to the perturbation stress tensor and velocity from which the eigenfunctions for a given wave-vector q emerge.

There are associated advantages and disadvantages to using this method of linear stability analysis compared to root finding methods such as in Refs. [16, 91, 92, 94]. A disadvantage of the method is that for a given value of q only the most unstable, or least stable, eigenvalue can be easily calculated. Therefore, even if multiple eigenvalues are unstable for a single mode, only the largest may be determinable.

In several studies by Wilson and collaborators [91,94], the authors are able to examine the limit of a discontinuously banded, or layered, base state of the flow. Given that the method used here requires spatial resolution of the base state and eigenfunctions, the addition of a diffusion term as used in Ref. [97] is necessary to study the evolution of a shear-banded flow. The method also cannot explore the limit of zero solvent viscosity, since the perturbation flow field $\tilde{\mathbf{v}}_q$ must be solved at each timestep via Eq. 3.37.

An advantage to using this method however is that it allows for the study of a variety of constitutive models, without the necessity for cumbersome linearisation of the model equations of each one. Secondly, while only able to capture the most unstable mode, unlike the root finding methods used in other studies no initial estimate is required to determine the eigenvalue. Therefore one can determine that a mode is conclusively stable or unstable via this method and not need to worry about having “missed” the mode due to inaccurate initial estimates.

3.6 Criterion For Instability

We aim to show that the instability of pressure driven channel flow can be understood and predicted via the properties of the base state. As we have discussed the applied pressure drop determines the wall shear-stress in the channel. By considering force balance we know that the divergence of the total stress tensor $\nabla \cdot \mathbf{\Pi} = 0$. This leads to the expression for the shear-stress $\Sigma = \sigma_{xy} + \eta\dot{\gamma}$ such that

$$\partial_y \Sigma - P' = 0. \tag{3.39}$$

We can therefore deduce that the total shear-stress is linear with respect to position in the channel, with $\Sigma = 0$ at the centre, increasing to $\Sigma = P' L_y/2$ at $y = L_y/2$. The variation in the shear-stress as a function of position is then linear, with slope P'.

The $\Sigma(\dot{\gamma})$ and $N_1(\dot{\gamma})$ curves give the steady state shear-stress and first normal stress difference as a function of shear-rate. The corresponding shear-rate can also therefore be determined as a function if applied shear-stress $\dot{\gamma} = \dot{\gamma}(\Sigma)$. Within the channel, this varies as a function of position with dependence $\Sigma(y) = P'y$. Following from this one can determine the local shear-rate in the channel as a function of position $\dot{\gamma}\,(y) = \dot{\gamma}(\Sigma = P'y)$ using the steady state shear-stress curve. We see how the base-state in each of the models studied in this chapter then varies with the corresponding flow curves.

Similarly we can combine the shear and normal stress flow curves $\Sigma(\dot{\gamma})$ and $N_1(\dot{\gamma})$ to give the first normal stress difference as a function of position across the channel using $N_1(\Sigma = P'y)$. The slope of the variation in normal stress across the channel is then given by

$$\frac{dN_1}{dy} = \frac{d\Sigma}{dy}\frac{dN_1}{d\Sigma} = P'\frac{dN_1}{d\Sigma} = P'\frac{dN_1}{d\dot{\gamma}} / \frac{d\Sigma}{d\dot{\gamma}}. \tag{3.40}$$

We observe from this that the regime of strong shear-thinning (small $d\Sigma/d\dot{\gamma}$) may lead to large variation in normal stress gradients within the channel. In previous work by Wilson examining layered Oldroyd B fluids [91, 94] and shear-banded

Johnson-Segalman fluids [118], instability was attributed to large variations in first normal stress difference between fluid layers or shear-bands. We postulate that for a shear-thinning fluid, given sufficiently high normal stress gradient within the channel, the base state is predisposed to instability to two dimensional perturbations.

The gradient in N_1 increases with applied pressure drop P'. However, even the normal stress gradient of an Oldroyd B fluid (a constant viscosity viscoelastic fluid) will increase indefinitely with increasing pressure drop P', yet we know channel flow in Oldroyd B to be stable to perturbations along the flow direction beyond large gradients in $\frac{dN_1}{dy}$ [92]. We therefore postulate the presence of shear-thinning to be a necessary condition. For a regime of high shear-thinning to occupy the space between the walls in the channel we must have

$$P' \frac{L_y}{2} - \Sigma^* > 0. \tag{3.41}$$

Here Σ^* is the shear-stress of the quasi-plateau, the flat regime of the flow curve, which marks the shear-thinning region of the flow curve of many fluids (see Figure 3.3). This value on the flow curve corresponds to the minimum logarithmic slope of the flow curve $\frac{d \log \Sigma}{d \log \dot{\gamma}}|_{min}$. In order to observe instability the applied pressure drop must exceed twice this plateau value, such that the shear-thinning region is within the channel.

We next assume that given the presence of shear-thinning within the channel, the normal stress gradient required is a function of the degree of shear-thinning, calculated as the minimum logarithmic slope of the flow curve

$$\frac{dN_1}{dy}|_{max} > f \left(\frac{d \log \Sigma}{d \log \dot{\gamma}}|_{min} \right), \tag{3.42}$$

where f is some unknown increasing adimensional function of its argument. In our chosen units the necessary prefactor to the right hand side G/L_y is equal to one. This equation can be written as the equivalent expression

$$P'^* \frac{dN_1}{d\Sigma}|_{max} > f \left(\frac{d \log \Sigma}{d \log \dot{\gamma}}|_{min} \right), \tag{3.43}$$

where $\frac{dN_1}{d\Sigma}|_{max}$ is the maximised value of $\frac{dN_1}{d\Sigma}$ in the base state flow within the channel. We will show for several of the models studied we find a reasonable collapse to the function

$$f(\zeta) = \alpha_0 + \alpha_1/(\alpha_2 - \zeta). \tag{3.44}$$

Here $\alpha_0, \alpha_1, \alpha_2$ are parameters fitted to the data calculated for each model. The parameter α_2 corresponds to the maximum degree of shear-thinning at which instability can be observed. We see that for each model studied here the calculated data fit reasonably well to this functional form, but that the parameters vary with each model studied. We shall discuss the effectiveness of these criteria with respect to each model studied in this chapter.

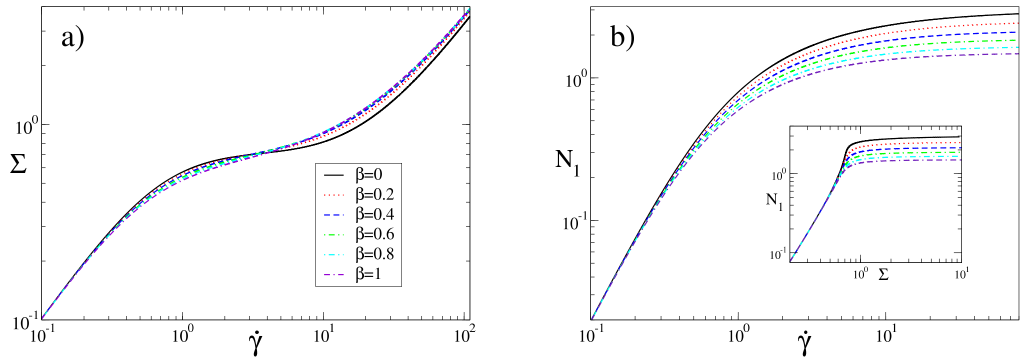

Figure 3.3: a) Flow curves of shear stress as a function of shear rate $\dot{\gamma}$ in homogeneous (0D) shear flow, computed in the Rolie-Poly model for several values of the convective constraint release parameter β, with solvent viscosity $\eta = 0.03$. b) The corresponding normal stress as a function of shear rate and (inset) plotted parametrically as a function of shear stress Σ.

3.7 Rolie-Poly model

3.7.1 Flow Curves

The shear stress and first normal stress difference curves of the 0D Rolie-Poly model, computed with the assumption of a homogenous shear flow are plotted in Figure 3.3. The shear stress as a function of shear rate is plotted in Figure 3.3 a). We observe for strain rates roughly between $\dot{\gamma} = 1 - 10$ a region of very strong shear thinning. The stress plateau corresponding to this region is $\Sigma^* \approx 0.75$ for all values of the CCR parameter β shown. Curves of first normal stress shown in Figure 3.3 b) show a steep rise within this range of shear-rates, before each converges asymptotically to a constant as $\dot{\gamma} \to \infty$. This asymptotic value decreases with increasing CCR parameter β.

3.7.2 Base State

As noted to previously, the homogeneous flow curves just discussed relate directly to the 1D base state in pressure-driven channel flow. The requirement that the shear stress be linear across the channel means that, for any set of values of the

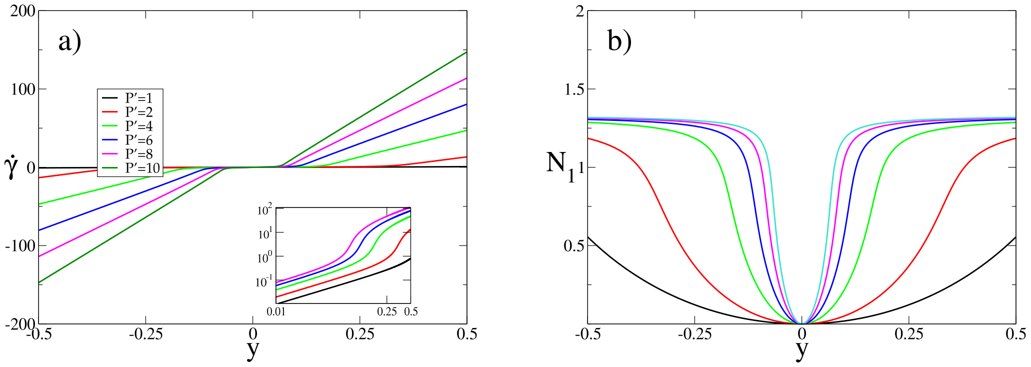

Figure 3.4: a) Base state profiles of shear-rate as a function of position across the channel in the Rolie-Poly model for $\beta = 0.5, \eta = 0.03$. Inset shows the same data for $y > 0$ on a log-log scale. b) Corresponding base state profile of the first normal stress as a function of position across the channel.

model parameters, the variation of the shear-rate as a function of position across the channel is an inversion $\dot{\gamma}(y) = \dot{\gamma}(\Sigma = P'y)$ of the flow curves as shown in Figure 3.4 a). In the same way, combining the shear and first normal stress difference flow curves $\Sigma(\dot{\gamma})$ and $N_1(\dot{\gamma})$ into the parametric plot $N_1(\Sigma)$, as shown inset in Figure 3.3 b), gives the normal stress as a function of position across the channel $N_1(y) = N_1(\Sigma = P'y)$. The result of this in the Rolie-Poly model is the creation of a pseudo-interfacial region at some location across the channel, where N_1 and $\dot{\gamma}$ both change steeply. The interface position is given by Σ^*/P', which corresponds to the shear thinning plateau discussed previously.

3.7.3 Linear Behaviour

Linear stability analysis of the Rolie-Poly model demonstrates a 1D base state to be unstable to 2D perturbations. The dispersion relations shown in Figure 3.5 a) show $Re(\omega_q)$ as a function of wavevector q. As mentioned previously, the existence of $Re(\omega_q) > 0$ for any q demonstrates the 1D base state to be unstable to 2D perturbation $\propto e^{iqx}$. We observe the transition between stable and unstable flow as with increasing applied pressure drop the peak of the dispersion relation crosses from negative to positive. The transition shown here for the given values of β and η occurs for $P'^* \approx 7.8$. The values of critical pressure drop for a range of β describe

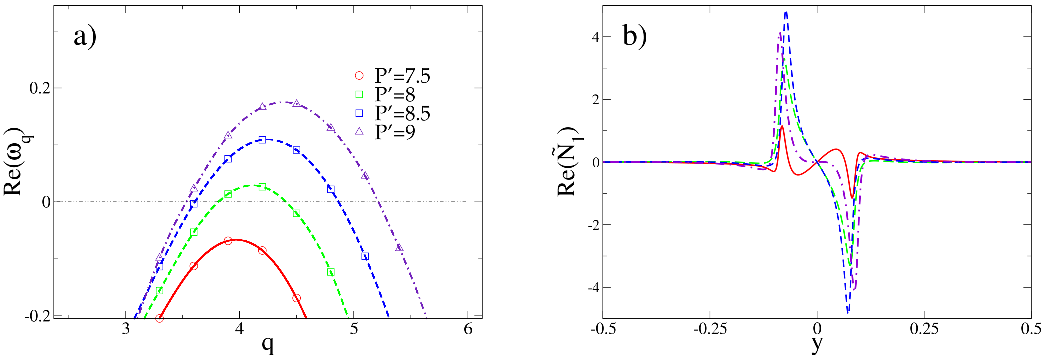

Figure 3.5: a) Dispersion relation of growth rate $Re(\omega_q)$ as a function of wavevector for several values of the applied pressure drop in the Rolie-Poly model for a CCR parameter $\beta = 0.5$ and solvent viscosity $\eta = 0.03$. Numerical grid and timestep $N_y = 1024$ and $dt = 10^{-4}$. b) The real part of the normalised eigenfunction in the first normal stress difference, $Re(\tilde{N}_1)$ at wavevector $q = 4.5$.

the neutral stability curve. The dispersion relation $Re(\omega_q)(q)$ is shown in Figure 3.5 a). For the given parameter values β and η, instability is observed for imposed pressure drops exceeding a critical threshold value, $P' > P'^{*}(\beta, \eta) \approx 7.8$.

The corresponding normal stress part of the eigenfunction is shown in Figure 3.5 b) for wavevector $q = 4.5$. The peaks of the eigenfunction have been found to correspond to the location of the pseudo-interface within the channel, with the same properties of symmetry, $y \to -y$ as the interface position of the shear-rate or first normal stress difference. This indicates that the mode of instability corresponds to a displacement of the base state. This displacement is in the same direction in both halves of the channel. This corresponds to a sinuous mode, as opposed to a varicose mode which would show an equal and opposite displacement in the two halves of the channel. Although the definition of sinuous and varicose usually refer to the symmetry of the perturbation to the flow velocity, we have checked that this accords with the perturbation in N_1. We have performed linear stability calculations over a full range of values of the convective constraint release parameter, $0 \leq \beta \leq 1$, for several values of solvent viscosity η. The calculated curves of neutral stability are shown by the solid curves in Figure 3.6 b). For fixed β the flow is always stable at low P'. This is to be expected as the Rolie-Polie model will behave as an Oldroyd B fluid in this limit. For the lowest value of solvent viscosity studied, $\eta = 0.025$, instability is observed for all values of β for some critical pressure drop P'^{*}. As the solvent viscosity is increased, the range of β for which instability is observed narrows. At very high values of pressure drop, re-entrant stability is observed, leading to a region of the parameter space P', β where the flow is unstable. The kinks apparent in some of the solid curves arise not from numerical difficulties but due to the most unstable mode switching as β and η are varied.

3.7.4 Criterion for Instability Onset

Within the Rolie-Poly model, we have shown that an initially 1D base state flow is linearly unstable to the onset of 2D perturbations. We have shown this to be the case over a wide range of pressure drops and model parameter values. We now aim to link these results to the criterion introduced at the start of this chapter. As stated previously the criterion we propose relates the minimum logarithmic slope of the 0D shear flow curve $\frac{d\log\Sigma}{d\log\dot{\gamma}}|_{min}$ to the maximum normal stress gradient across the channel $\frac{dN_1}{dy}|_{max}$. To test this we plot in Figure 3.6 a) the critical normal stress gradient $\frac{dN_1}{dy}$ across the channel against the minimum logarithmic slope of the shear flow curve $\Sigma\left(\dot{\gamma}\right)$. To do this, for each pairing β, η plotted as solid lines in Figure 3.6 b) we read off the critical pressure drop calculated from the corresponding flow curve. The maximised value of $dN_1/d\Sigma$ is taken from the parametric plot of N_1 against Σ. The product of this quantity and the critical pressure drop then gives the maximum normal stress gradient within the channel.

These results are collected into Figure 3.6 a) where we observe a reasonable curve collapse onto the function in Eq. 3.44. The parameters found to best fit this function are $\alpha_0 = 25.81$, $\alpha_1 = 0.33$ and $\alpha_2 = 0.21$ for all β,η. Following this we reconstruct the critical pressure drop for any pair of parameter values β, η using these values. By taking Eq. 3.44 and multiplying both sides by $\frac{dN_1}{d\Sigma}|_{max}$, we obtain an expression for the critical pressure drop predicted by the fitted criterion. These are shown as dashed lines in Figure 3.6 b). We find that these values indeed fit the numerical data quite well, but fail to capture the region of re-entrant stability,

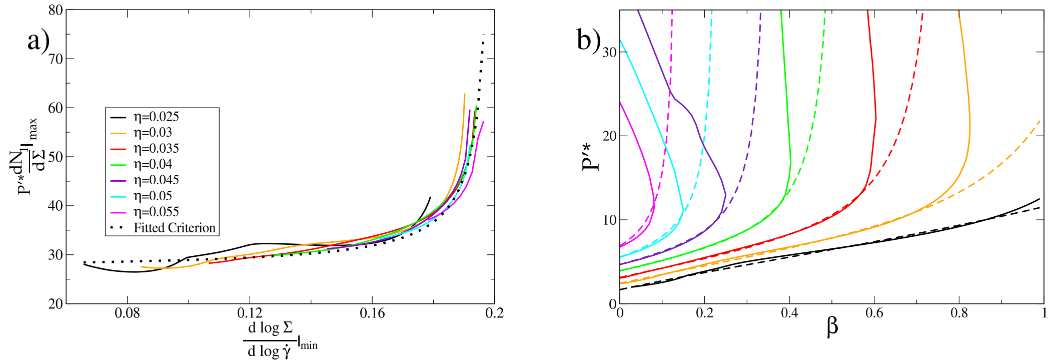

Figure 3.6: a) The expression $P'^* \frac{dN_1}{d\Sigma}|_{max}$ corresponding to the maximum normal stress gradient within the channel plotted as a function of the minimum logarithmic slope $\frac{d \log \Sigma}{d \log \dot{\gamma}}|_{min}$. Dashed line: function $y = f(\zeta)$ of Eq. 3.44 with $\alpha_0 = 25.81$, $\alpha_1 = 0.332$ and $\alpha_2 = 0.21$. b) Solid lines: curves of neutral stability $P'^*(\beta, \eta)$ as a function of the CCR parameter β in the Rolie-Poly model for several values of the solvent viscosity $\eta = 0.025, 0.03, 0.035, 0.04, 0.045, 0.05, 0.055$. Dashed lines: fits using Eqs.3.44 and 3.43 (which we note does not capture the regime of re-entrant stability).

and so depart from the numerical data near the turning point of the data where the onset of instability and re-onset of stability meet.

According to the form of the criterion, we should not expect to see instability for any flow curve for which the minimum logarithmic slope $\frac{d \log \Sigma}{d \log \dot{\gamma}}|_{min}$ exceeds the fitted parameter $\alpha_2 \approx 0.21$. We construct the plot in Figure 3.7 depicting contours of $\frac{d \log \Sigma}{d \log \dot{\gamma}}|_{min}$ as dotted lines in the plane of β and η. We also show the maximum values of solvent viscosity for which instability has been observed in our numerical calculations. The region of instability appears indeed to be found for values of minimum logarithmic slope below about 0.21. The contour described by α_2 is shown as a solid red line and follows a trend just above the numerically calculated values. The black highlighted contour represents $\frac{d \log \Sigma}{d \log \dot{\gamma}}|_{min} = 0$, below which the flow curves of stress against strain-rate is non-monotonic and the corresponding base state profile will be shear-banded. Within this regime we have checked that the 1D shear banded base state is indeed unstable to 2D perturbations. To extend our study into the shear banded regime, a stress diffusion term was added to the right hand

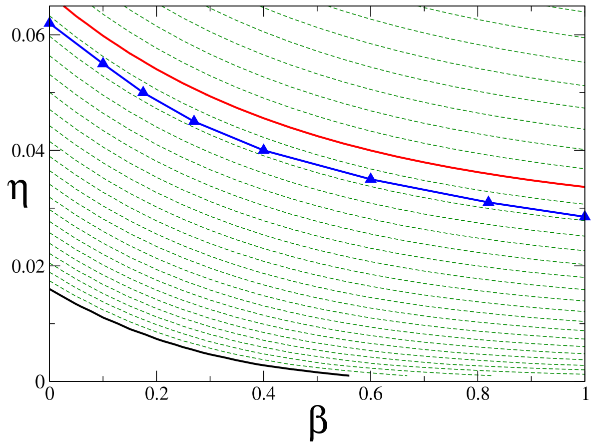

Figure 3.7: Dotted lines: Contours of minimum logarithmic slope of the flow curve, $d\log\Sigma/d\log\dot{\gamma}|_{min}$ increasing in increments of 0.01 in contours upward. The lowest (black) contour has $d\log\Sigma/d\log\dot{\gamma}|_{min} = 0$ (below which the flow curve is non-monotonic and the base state is shear-banded). The contour 0.21 is shown as a solid red line. The solid blue triangles show numerical data for the maximum solvent viscosity η that admits instability at any value of CCR parameter, β, consistent with a contour value $d\log\Sigma/d\log\dot{\gamma}|_{min} \approx 0.21$.

side of Eq. 3.16. The addition of a stress diffusion term outside the banding regime would have the effect of reducing the steepness of variation of normal stress and would potentially have a stabilising effect on the flow. The instability in strongly shear-thinning but not shear banded flow may be understood as the destabilisation of a quasi-interface, similar to the instability of a true interface in shear-banded flow.

Critical Wavevector

It is observed in the Rolie-Poly model that as the solvent viscosity and CCR parameter β are varied, the critical pressure drop changes. Also observed are abrupt changes in principal wave-number q^*. We see this in Figure 3.6 b), where there are sudden changes in direction of the stability curves. An example of this shift is shown in Figure 3.8 a), whereby a secondary peak to the dispersion relation emerges and exceeds the former peak. As we are unable to explore all but the most unstable

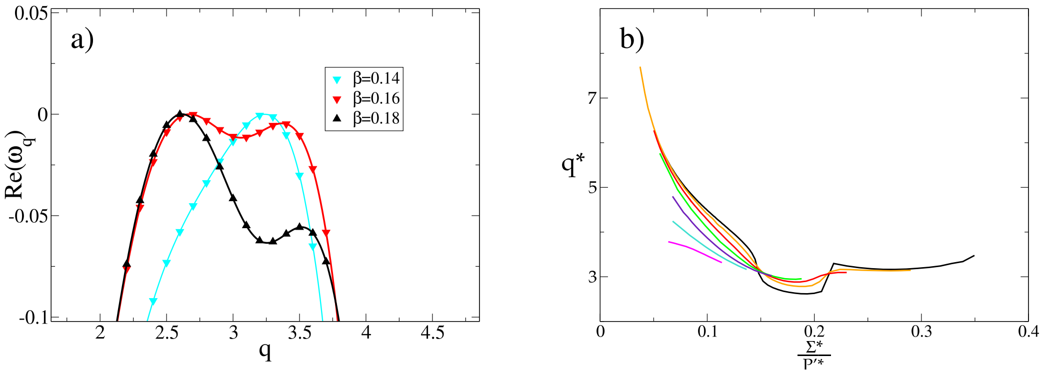

Figure 3.8: a) Dispersion relations, $Re(\omega_q)$ vs q, for several values of β calculated at corresponding critical pressure drop $P'^*(\beta)$ for $\eta = 0.025$ with $N_y = 1024$, $dt = 10^{-4}$. b) Principal wave-vector versus interface position at critical pressure drop $P'^*(\beta)$ for different values of solvent viscosity $\eta = 0.025, 0.03, 0.035, 0.04, 0.045, 0.05, 0.055$.

eigenvalue for each set of values β, η and P', we cannot look more closely at how this mode switch develops, but indications are given by examining properties of the base state.

In Figure 3.8 b) the principal wavenumber is plotted as a function of the position of the interface at the onset of instability (calculated as Σ^*/P'^*). We observe a reasonable curve collapse of critical wavenumber for different values of solvent viscosity. The sudden shift in wavenumber, observed for lower values of solvent viscosity, appears to occur at $P'^*/\Sigma^* \approx 0.25$, where the higher and lower shear rate Newtonian regimes occupy equal proportions of the channel. This result suggests that the pseudo-interfacial behaviour has a strong influence on the most unstable wave-vector and the form of the dispersion relation.

Stability Re-onset

We observe in the Rolie-Poly model that at high pressure drops, flows are once again stable. This re-onset of stability creates a region of P' and β for each value of solvent viscosity wherein the flow is linearly unstable to perturbations.

This behaviour may be understood by considering once again the base state prior to the onset of instability and the steady state flow curves. As we have discussed previously, the shear-rate in the channel directly corresponds to the 0D shear stress flow curve due to the linear variation in shear-stress in the channel $\dot{\gamma}\,(\Sigma = P'y)$. In the Rolie-Poly model, the flow curve consists of a low shear-rate Newtonian regime, a shear-thinning plateau and a high shear-rate Newtonian regime which corresponds to the solvent shear-stress becoming dominant. This then leads to parabolic flow profile near the centre of the channel, an interface like region with large variation in shear-rate, and a high shear-rate parabolic Newtonian flow profile towards the channel edge. As the applied pressure drop increases the proportion of the flow dominated by the high shear-rate Newtonian regime also increases.

In the Rolie-Poly model, the flow curve of the first normal stress difference saturates at high shear-rates. This is replicated in the base state of first normal stress difference in the channel. At high applied pressure drops, the value of the first normal stress difference varies very little towards the edge of the channel. The shear-stress, however, continues to increase linearly across the channel. At high pressure drops, therefore, the shear-stress may dominate the flow. It is therefore possible that this dominance of the shear-stress over the normal stress (or the viscous over the elastic stress) leads to the re-stabilisation of the flow at high pressure drops. In order to characterise relative magnitude of shear versus normal stress in the channel we define the wall Weissenberg number

$$Wi_{wall} = \frac{N_1\left(\dot{\gamma}_{wall}\right)}{\Sigma\left(\dot{\gamma}_{wall}\right)}. \tag{3.45}$$

Here $\dot{\gamma}_{wall}$ is the shear-rate at the edge of the channel.

We plot the value of Wi_{wall} at the re-onset of stability as a function of the logarithmic slope of the shear-stress flow curve $\frac{d\log\Sigma}{d\log\dot{\gamma}}$ in Figure 3.9 a). We observe the surprising result that for the largest values of solvent viscosity $\eta = \{0.045, 0.05, 0.055\}$, the reonset curves appear to overlap, suggesting that the reonset of stability can be explained in terms of the viscous stresses becoming dominant in the flow at high pressure drops.

However, for the lower values of solvent viscosity $\eta = \{0.03, 0.035, 0.04\}$, no overlap is observed and the stability reonset Weissenberg numbers are lower than those for the other curves. This rather strange result may be connected to the critical (most unstable) wavevector q^*. In Figure 3.9 b), q^* at the re-onset

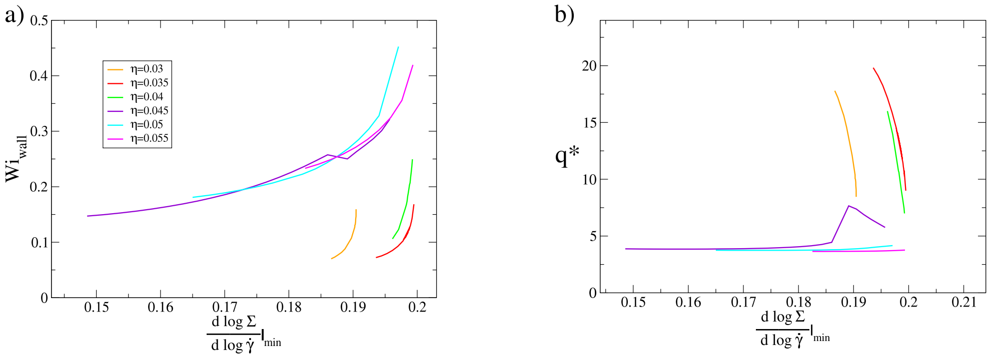

Figure 3.9: a) Wall Weissenberg number versus logarithmic slope at the re-onset of stability for several values of solvent viscosity η. b) Critical wave-vector q^* versus logarithmic slope of the flow curve at the re-onset of stability for several values of solvent viscosity η.

of stability is plotted as a function of the logarithmic slope of the flow curve for values corresponding to Figure 3.9 a). For the lower values of solvent viscosity η, the values of the critical wave-vector are quite different to those for the high values. This suggests a mode switch at high values of β, similar to those discussed previously. This appears to lead to different dynamics governing the re-onset of stability to those at lower values of β. It is unclear why this should be the case and further study is required to uncover the connection between the most unstable wave-vector q^*, the re-onset stability wall Weissenberg number Wi_{wall} and the CCR parameter β.

3.7.5 Non-linear Simulation

The linear analysis thus far performed on the Rolie-Poly model is valid where the perturbations remain small. In order to study the dynamics of these perturbations once they have grown to some finite amplitude, we perform full non-linear 2D simulations. An example of the results of these simulations is shown in Figure 3.10.

The flow is initialised similar to the linear study with a 1D base state subject to a small perturbation expressed in terms of Fourier modes. In Figure 3.10 a) the full xx-component of the stress tensor is shown. In panel Figure 3.10 b) this is shown with the initial base state subtracted off. Even in the long time-scale behaviour, the system's state retains a clear interface, with variations of the Σ_{xx} terms of the stress tensor displaying the greatest deviation from the base state near the interface. The flow field with the base state subtracted is shown in Figure 3.5

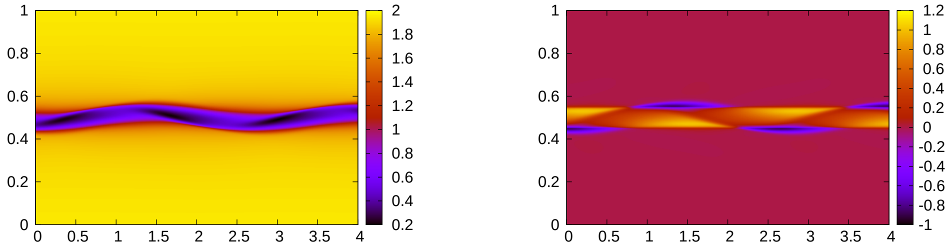

(a) Σ_{xx}

(b) $\Delta\Sigma_{xx}$

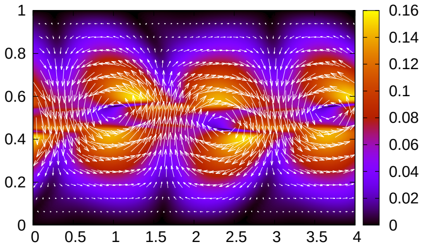

(c) $\Delta\mathbf{v}$

Figure 3.10: Non-linear simulations of unstable flow in the Rolie-Poly model for parameter values $P' = 15$, $\beta = 0.0$, $\eta = 0.03$ and $L_x = 16$, $N_x = 512$, $N_y = 1024$, $dt = 0.0005$. a) The xx component of the viscoelastic stress tensor. b) The xx component of the stress tensor with the 1D base state subtracted $\Delta\Sigma_{xx} = \Sigma_{xx} - \Sigma_{0xx}$. c) The magnitude of the velocity of the flow field with the base flow field subtracted $\Delta\mathbf{v} = \mathbf{v} - \mathbf{v}_0$. The arrows show the direction of the velocity perturbation with the magnitude scale being shown by the colourbar. Only 1/4 of the simulation box is shown in the $\hat{\mathbf{x}}$ direction.

c), displaying the channel spanning vortices that are formed in the unstable flow. We note however that the magnitude of the secondary flows are much smaller than the base state, despite the applied pressure drop being quite high relative to the threshold of instability ($P'^*(0, 0.03) \approx 2.45$). This is in contrast to the results seen in Ref. [18, 19], which show larger secondary flows in experiment.

3.8 The Johnson-Segalman Model

3.8.1 Flow Curves

The homogeneous shear stress flow curves of the Johnson-Segalman model are plotted for a range of values of the slip parameter a in Figure 3.11 a). These have the same basic form as the flow curves of the Rolie-Poly model discussed previously, possessing a low and high shear-rate Newtonian regime, with a shear thinning plateau for intermittent values of shear-rate. A notable difference however is that the height of the plateau regime, where $\Sigma\left(\dot{\gamma}\right)$ varies slowly with $\dot{\gamma}$, varies considerably as a function of the slip parameter a. To demonstrate this we consider the analytical solution for the shear-stress flow curve

$$\Sigma(\dot{\gamma}) = \frac{G\tau\dot{\gamma}}{1+(1-a^2)\tau^2\dot{\gamma}^2} + \eta\dot{\gamma}. \tag{3.46}$$

In order to determine the plateau stress, we must first determine the shear-rate $\dot{\gamma}^*$ at which $d\log\Sigma/d\log\dot{\gamma}$ is minimised. The analytical form of the minimum logarithmic slope is given by the expression

$$\frac{d\log\Sigma}{d\log\dot{\gamma}} = \frac{\dot{\gamma}}{\Sigma}\frac{d\Sigma}{d\dot{\gamma}} = \frac{1}{\dfrac{G\tau}{1+(1-a^2)\tau^2\dot{\gamma}^2}+\eta}\left(\frac{G\tau}{1+(1-a^2)\tau^2\dot{\gamma}^2} - \frac{2(1-a^2)G\tau^3\dot{\gamma}^2}{(1+(1-a^2)\tau^2\dot{\gamma}^2)^2}\right). \tag{3.47}$$

Minimising this with respect to $\dot{\gamma}$ we find that the plateau shear-rate and shear-stress are respectively

$$\dot{\gamma}^* = \frac{1}{\tau\sqrt{1-a^2}}(\frac{G\tau}{\eta}+1)^{1/4} \tag{3.48}$$

$$\Sigma^* = \frac{G}{\sqrt{1-a^2}}\left[\eta^{1/4}(G\tau+\eta)^{3/4}\right] \tag{3.49}$$

We see that the plateau stress diverges as $a \rightarrow 1$, corresponding to the limit at which JS is equivalent to the Oldroyd B model. Using this expression, as well as the analytical solution of the flow curve in Eq. 3.47, we are able to obtain an analytical expression for the logarithmic slope for $|a| < 1$

$$\frac{\dot{\gamma}}{\Sigma}\frac{d\Sigma}{d\dot{\gamma}}|_{min} = -\frac{4\eta}{G\tau} + \frac{4\sqrt{\eta}\sqrt{\eta+G\tau}}{G\tau} - 1. \tag{3.50}$$

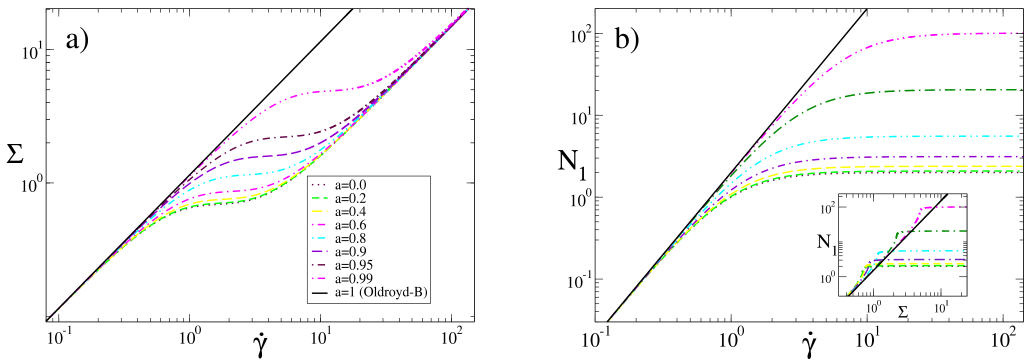

Figure 3.11: a) Flow curves of shear stress as a function of shear-rate for states of homogeneous shear flow in the Johnson-Segalman model, for a solvent viscosity $\eta = 0.15$, and several values of the slip parameter a b) The corresponding curves of normal stress as a function of shear rate, and (inset) parametrically plotted as a function of shear stress.

Unlike the Rolie-Poly model for the CCR parameter β, we see that the logarithmic slope for JS is independent of slip parameter a. In Rolie-Poly it depends strongly on the CCR parameter β.

3.8.2 Base State

As we showed in the case of the Rolie-Poly model, the steady state shear-stress and first normal stress difference flow curves of the Johnson-Segalman model correspond directly to the 1D base state of pressure driven channel flow. Examples of these base states in shear-rate and first normal stress difference are shown in Figure 3.12 a) and b) respectively. We also observe in this model a steep gradient in shear-rate and first normal stress difference at the position which corresponds to the plateau stress of the steady state flow curves. The highly localised nature of this region creates a pseudo-interface in the channel between the high-shear-rate and low-shear-rate regimes. Based on the analytical expression Eq. 3.49, the value of the shear-stress plateau will diverge as $a \rightarrow 1$. This means that, for fixed pressure drop, as the non-affine parameter a increases towards 1, the corresponding position of the interface will also move away from the centre of the channel towards the wall. The base state will then only retain a shear-thinning region if $P' < 2\Sigma^*/L_y$, since the shear

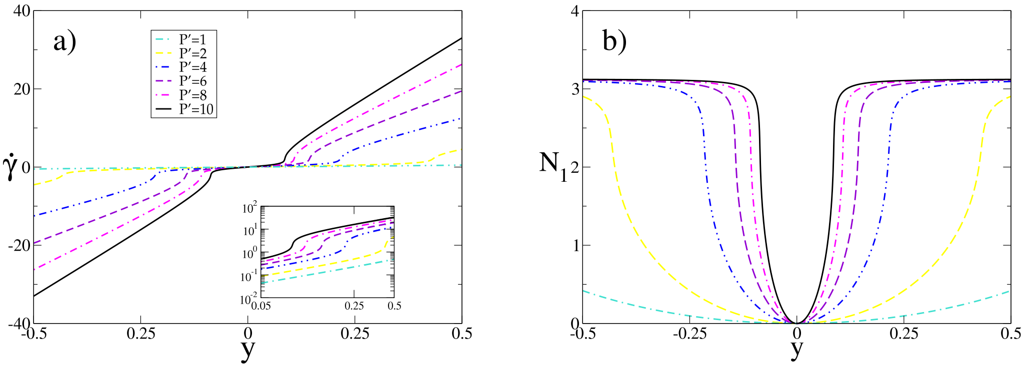

Figure 3.12: a)The base state profile of shear rate as a function of position for the Johnson-Segalman model for $a = 0.6$, $\eta = 0.15$, $N_y = 2048$. Inset shows the same data for $y > 0$ on a log-log scale. b) The corresponding base state profile of first normal stress difference as a function of position in the channel.

stress at the wall must exceed the plateau stress for the shear-thinning regime to be located within the channel. The corresponding base state for first normal stress difference will also change in response to the variation in non-affine parameter a. If the shear-thinning region is not within the channel, the form of the base state normal stress difference will be a parabola as in the case of the Oldroyd B model.

3.8.3 Linear Behaviour

As in the Rolie-Poly model, we perform linear stability analysis on the Johnson-Segalman model for different combinations of parameters a and η. Figure 3.13 a) shows for a single set of a and η the dispersion relation of the growth rate $Re(\omega_q)$ as a function of wavenumber q for a range of applied pressure drops. We observe that above a certain pressure drop the 1D base flow becomes unstable to 2D perturbations. We observe the transition from stable to unstable flow between $P' = 3.25$ and $P' = 3.5$, with the most unstable wavenumber observed to be $q \approx 2.25$. The dispersion relations have a similar form to those seen in the Rolie-Poly model, as do the eigenfunctions of first normal stress difference $\tilde{N}_1$ shown in Figure 3.13 b). The eigenfunctions of N_1 therefore resemble $\dfrac{dN_1}{dy}$ of the base state, indicating that the instability corresponds to a shift of the interface in the underlying base state.

Earlier studies of shear banded flow in the Johnson-Segalman model have

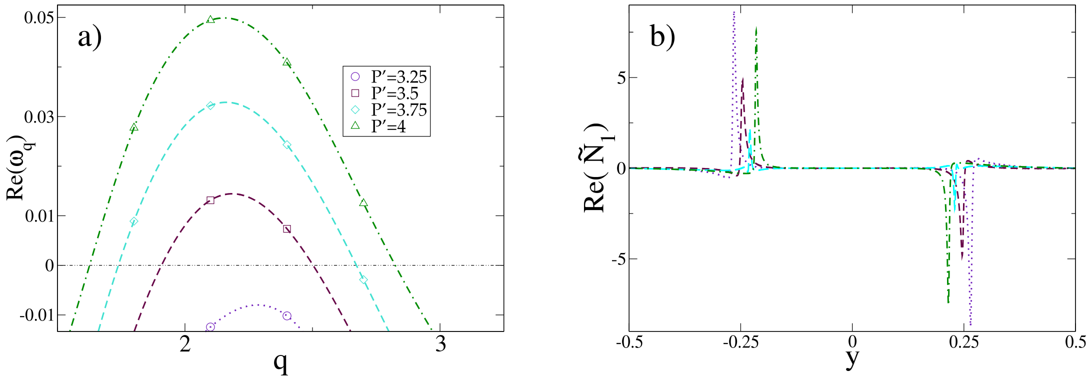

Figure 3.13: a) Dispersion relations of growth rate $Re(\omega_q)$ as a function of wavevector for a range of applied pressure drops for the Johnson-Segalman model with slip parameter $a = 0.6$ and solvent viscosity $\eta = 0.15$. Numerical grid $N_y = 2048$ and timestep $dt = 10^{-4}$. b) The real part of the normalised eigenfunction of the first normal stress difference $Re(\tilde{N}_1)$, with wave-vector $q = 2.7$.

shown a 1D shear-banded flow to be unstable to 2D undulations along the interface between the bands [97–99], consistent with what we observe here. We do not consider the shear banded regime here, and restrict ourselves to values of solvent viscosity for which the flow curves remain monotonic.

We perform linear stability calculations for several values of solvent viscosity η over a range of values of the slip parameter $0 \leq a \leq 1$. The calculated curves of neutral stability are shown as solid curves in Figure 3.14 b). For fixed a the flow is always stable at low values of applied pressure drop P', since only the low shear-rate Newtonian portion of the flow curve is within the channel. For the lowest four values of solvent viscosity we observe that the flow is unstable at sufficiently high pressure drops for all values of a. For the highest viscosity explored, only a portion of the range of a is unstable. Although re-entrant stability was found to be present in the Jonhson-Segalman model, it was not found at pressure drops low enough for the numerical calculations to be considered reliable and so is not shown here.

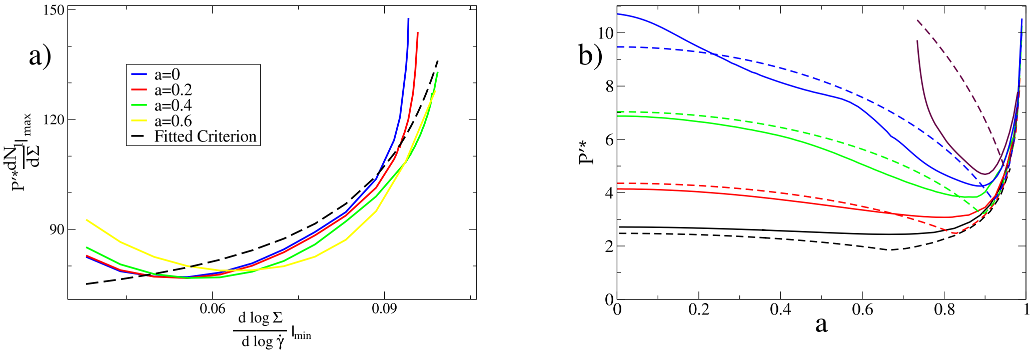

Figure 3.14: a) Dashed line: function $f(\zeta)$ of Eq. 3.44 with $\alpha_0 = 60.81$, $\alpha_1 = 1.15$ and $\alpha_2 = 0.11$. The expression $P'^* \frac{dN_1}{d\Sigma}|_{max}$ corresponding to the maximum normal stress gradient within the channel plotted as a function of the minimum logarithmic slope $\zeta = \frac{d\log\Sigma}{d\log\dot{\gamma}}|_{min}$. b) Corresponding neutral stability curves for different values of solvent viscosity $\eta = 0.14, 0.15, 0.16, 0.165, 0.17$(curves upwards). An initially 1D base flow is stable below each curve, and unstable above it (until a region of re-entrant stability is reached at much larger pressure drops, not shown). Dashed lines: predicted thresholds based on Eq. 3.56.

3.8.4 Criterion for Instability Onset

We seek to determine if the criteria shown to be reasonably successful in the Rolie-Poly model applies also to Johnson-Segalman.

Recall that the criterion is of the basic form

$$\frac{dN_1}{dy}|_{max} > f\left(\frac{d\log\Sigma}{d\log\dot{\gamma}}|_{min}\right), \tag{3.51}$$

where

$$f(\zeta) = \alpha_0 + \alpha_1/(\alpha_2 - \zeta). \tag{3.52}$$

We reiterate the additional criterion that is

$$P'\frac{L_y}{2} - \Sigma^* > 0. \tag{3.53}$$

This was not of great concern in the Rolie-Poly model since the plateau stress Σ^* did not vary a great deal with β. However as previously discussed, this is not the case in Johnson-Segalman. This may be found by maximising the analytical expression of the derivative of the first normal stress difference with respect to shear-stress

$$\frac{dN_1}{d\Sigma} = \frac{dN_1}{d\dot{\gamma}} / \frac{d\Sigma}{d\dot{\gamma}} = \frac{4\dot{\gamma}\tau}{\eta(1-(1-a^2)\dot{\gamma}^2\tau^2)^2 + 1 - (1-a^2)\dot{\gamma}^2\tau^2}. \tag{3.54}$$

Maximising the value of the expression in Eq. 3.54 with respect to shear-rate yields the following expression

$$\frac{dN_1}{d\Sigma}|_{max} = \frac{6\sqrt{3}G\tau}{\sqrt{1-a^2}} \left(\sqrt{\frac{\eta}{1+\eta}} \frac{1}{(8\eta - 1)} \right), \tag{3.55}$$

Using this equation, as well as the expression for the stress plateau in Eq. 3.49 we suggest a means to understand the shape of the stability curves in Figure 3.14. At lower values of slip parameter a, we postulate that the stability threshold is defined by the normal stress gradient within the channel as in RP. Since $\frac{dN_1}{d\Sigma}|_{max}$ will increase with a, the normal stress gradient across the channel will also increase for a fixed pressure drop. The minimum logarithmic slope $\frac{d\log\Sigma}{d\log\dot{\gamma}}|_{min}$ is however constant with respect to a, therefore the threshold normal stress gradient should also be invariant with a for a fixed value of solvent viscosity η. Accordingly, if Eq. 3.51 is valid, the minimum normal stress gradient required to cause the base state to become unstable should also not change with a. The critical pressure drop will therefore decrease as a function of increasing non-affine parameter a. This appears valid according to the results plotted in Figure 3.14, however for $a \gtrsim 0.8$ we see that the threshold pressure drop begins to increase. We propose that this is due to the variation in the plateau stress Σ^*, which diverges as $a \to 0$.

To test these postulates we must check that Eq. 3.51 accounts for the stability thresholds at low values of a. In order to do this we plot in Figure 3.14 a) curves of the critical normal stress gradient in the channel (calculated from a combination of the steady state state flow curves and the numerical measured critical pressure drop). This was performed by measuring the threshold pressure drop for varying solvent viscosity η at several fixed values of $0 \leq a \leq 0.6$. We observe that the curves collapse reasonably well onto each other, although possess more variation that was seen in the Rolie-Poly model. To this collapsed data, we then fit the functional form of Eq. 3.52. As we can see the functional form appears to follow the trend of the curves moderately well with fitting parameters $\alpha_0 = 60.81$, $\alpha_1 = 1.15$ and $\alpha_2 = 0.11$. To check how well this reflects the measured stability curves we perform the same process as in the Rolie-Poly model to calculate the predicted threshold pressure drop, but we make one modification. Since we have asserted that there are two regimes dictating the critical value of P', we determine the predicted value by solving the roots of the quadratic expression

$$\left[P' - \frac{2}{L_y}\Sigma^*\right]\left[P' - \left(\frac{dN_1}{d\Sigma}|_{max}\right)^{-1} f\left(\frac{d\log\Sigma}{d\log\dot{\gamma}}|_{min}\right)\right] = 0, \tag{3.56}$$

where $f\left(\frac{d\log\Sigma}{d\log\dot{\gamma}}|_{min}\right)$ has the parameters in Eq. 3.52 as best fit to the data plotted in Figure 3.14 a). By only considering the roots of this equation for which the non-zero factor of Eq. 3.56 is positive we obtain the values plotted as dashed lines in Figure 3.14 b). As we see this performs reasonably well for the lowest values of solvent viscosity studied, where the pressure drop values are modest. It performs less well at higher solvent viscosities, for which the critical values of P' are much higher. This may be attributable to the proximity of the quasi-interface to the centre of channel. However, we are unable to take this into account in the studies performed here.

The value of $\alpha_2 = 0.11$ obtained by fitting to the data in Figure 3.14 means that the Johnson-Segalman model should not admit instability if the minimum logarithmic slope of the flow curve exceeds $\frac{d\log\Sigma}{d\log\dot{\gamma}}|_{min} = 0.11$. The contours of $\frac{d\log\Sigma}{d\log\dot{\gamma}}|_{min}$ as plotted in the parameter space η and a are shown in Figure 3.15, with all numerically measured values of $\frac{d\log\Sigma}{d\log\dot{\gamma}}|_{min}$ admitting instability in JS lying below this value. This shows the Johnson-Segalman model predicts, overall, much greater stability than the Rolie-Poly model, which has $\alpha_2 = 0.21$, since a fluid has to shear thin much more strongly to be unstable.

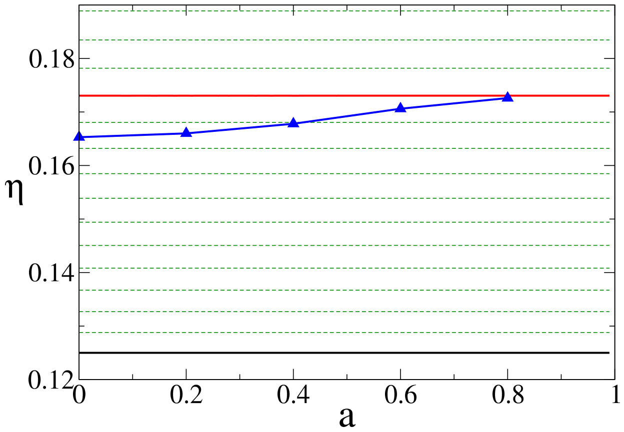

Figure 3.15: The region of instability mapped out with respect to non-affine parameter a and solvent viscosity η. Dotted lines: contours of minimum logarithmic slope of the flow curve, $\frac{d\log\Sigma}{d\log\dot{\gamma}}|_{min}$. The lowest (black) contour line corresponds to $\frac{d\log\Sigma}{d\log\dot{\gamma}}|_{min} = 0$ (below which the the flow curve is non-monotonic and the base profile is shear-banded. The contour 0.11 is also shown as a solid red line. Blue triangles show numerical data for the maximum solvent viscosity η that admits instability at any value of the slip parameter a, showing a reasonable agreement with an approximate contour range $0.095 \leq \frac{d\log\Sigma}{d\log\dot{\gamma}}|_{min} \leq 0.11$.)

.

3.8.5 Non-linear Simulations

To study the longer timescale behaviour in JS, we perform full nonlinear 2D simulations. Plots of the xx-component of the stress tensors (both its full value and with the value in the base flow subtracted) are shown in Figure 3.16. Figure 3.16 b) confirms that the instability takes the form of a quasi-interface, as in the Rolie-Poly model. We likewise see that the velocity field, with the subtracted base state reveals, a system-spanning vortex as in the non-linear simulations of the Rolie-Poly model in Figure 3.10.

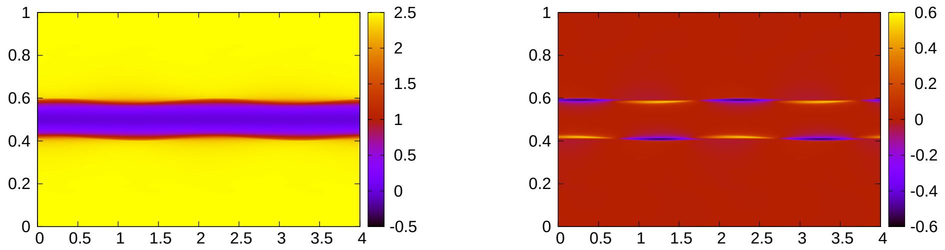

(a) Σ_{xx} (b) $\Delta\Sigma_{xx}$

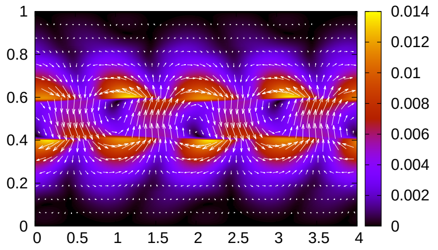

(c) $\Delta\mathbf{v}$

Figure 3.16: Non-linear simulations of the unstable flow in the Johnson-Segalman model $P' = 10$, $a = 0.6$, $\eta = 0.16, L_x = 8$ with $N_x = 512$, $N_y = 1024$, $dt = 0.0005$. a) The full Σ_{xx} component of the viscoelastic stress tensor. b) The $\Delta\Sigma_{xx}$ component of the stress with the base state subtracted $\Delta\Sigma_{xx} = \Sigma_{xx} - \Sigma_{0xx}$. c) The magnitude of the velocity of the flow field with the base flow field subtracted, $\Delta\mathbf{v} = \mathbf{v} - \mathbf{v}_0$. The arrows show the direction of the velocity perturbation with the magnitude scale being shown by the colourbar. Only 1/2 of the simulation box is shown in the x direction.

3.9 The White-Metzner Model

3.9.1 Flow Curves

Flow curves in the White-Metzner model follow a power law behaviour up to a correction due to Newtonian solvent and are written analytically as

$$\Sigma\left(\dot{\gamma}\right) = G\tau_0^n\dot{\gamma}|\dot{\gamma}|^{n-1} + \eta\dot{\gamma} \tag{3.57}$$

with

$$N_1\left(\dot{\gamma}\right) = 2G\tau_0^{2n}|\dot{\gamma}|^{2n}. \tag{3.58}$$

The flow curves are shown for a number of values of the shear thinning exponent n in Figure 3.17. In the limit of zero solvent viscosity, this exponent is also the logarithmic slope of the shear stress flow curve for all values of $\dot{\gamma}$ shown in Figure 3.17 a). The addition of a solvent however means that this is only exactly true at the centre of the channel. In fact the logarithmic slope (assuming positive shear) is given by

$$\frac{d\log\Sigma}{d\log\dot{\gamma}} = \frac{\dot{\gamma}}{\Sigma}\frac{d\Sigma}{d\dot{\gamma}} = \frac{G\tau_0^n n\dot{\gamma}^n + \eta}{G\tau_0^n\dot{\gamma}^n + \eta}. \tag{3.59}$$

The flow curves follow a power law behaviour up to very high shear rates where the Newtonian behaviour due to the presence of solvent is recovered. Unique among the models studied in this work, the White-Metzner model lacks a low shear-rate Newtonian regime. Given that the polymeric stress does not saturate as it does in other models, an explicit high shear-rate Newtonian regime is only recovered when $G\tau^n\dot{\gamma}^n \ll \eta\dot{\gamma}$. Another difference between White-Metzner and the other models in this study is the behaviour of the flow curve of first normal stress difference $N_1(\dot{\gamma})$, which does not saturate at high values of $\dot{\gamma}$. The parametric plot of N_1 versus Σ in the inset of Figure 3.17 b) shows that, for all values of n, $N_1 \propto \Sigma^2$ up to the higher shear rate regime, where the solvent effects become important. This will be significant when considering the form of the base state.

3.9.2 Base State

The base state profile of the shear-rate across the channel $\dot{\gamma}\left(y\right)$ in the White-Metzner model in the limit of zero solvent viscosity is given by the expression

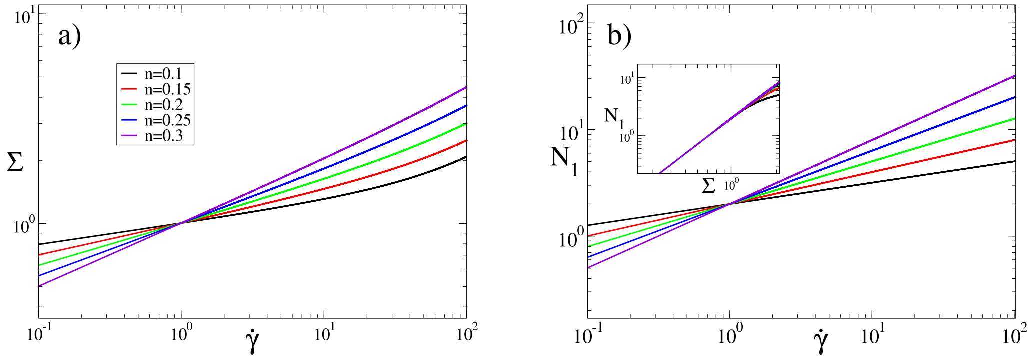

Figure 3.17: a) Flow curves of shear stress as a function of shear rate for states of homogeneous shear flow in the White-Metzner model for several values of power law exponent n and solvent viscosity $\eta = 0.005$. b) The corresponding curves of first normal stress difference for the equivalent range of power law exponent n. Inset: Plot of normal stress versus shear stress.

$\dot{\gamma} = \mathrm{sgn}(y)(P'/G\tau_0)^{\frac{1}{n}}|y|^{\frac{1}{n}}$. With the addition of solvent viscosity this is no longer the case, but we consider the correction to the base state to be small as it pertains to the following discussion. Combining the analytical expression for the base state shear rate as a function of position with the expression for the first normal stress difference, we obtain the analytical expression for the base state of normal stress difference as a function of position in the channel

$$N_1\left(y\right) = 2\frac{P'^2 y^2}{G}. \tag{3.60}$$

This expression remains valid while $\eta\dot{\gamma}$ remains small.

An important consequence of the absence of a plateau in the shear-flow curve $\Sigma\left(\dot{\gamma}\right)$ is that no interfacial region is found within the channel at which the shear rate can rapidly vary as a function of position. This distinguishes White-Metzner from the Rolie-Poly and Johnson-Segalman models. As a result we should expect the basic physics to differ from those in the models considered previously in this chapter.

The gradient of the first normal stress difference varies linearly across the channel, obtaining its largest value at the wall. Unlike the other models in this study, the location within the channel of the minimum logarithmic slope of the flow curve does not correspond to the location of the greatest normal stress gradient

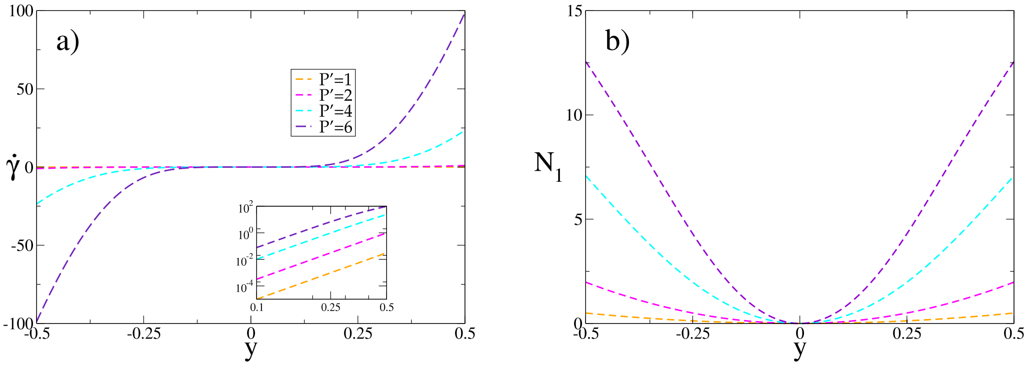

Figure 3.18: a) The base state profile of shear-rate as a function of position at a range of applied pressure drops for the White-Metzner model for $n = 0.2$, $\eta = 0.005$, $N_y = 1024$. Inset shows same data for $y > 0$ on a log-log scale. b) The corresponding profiles of first normal stress difference as a function of position across the channel.

$\frac{dN_1}{dy}$. This and the absence of a defined interface makes WM different to other models studied. Base state shear rate and normal stress are plotted in Figure 3.18 a) and b) respectively.

3.9.3 Linear Behaviour

Wilson and collaborators have shown in extensive previous investigations that the White-Metzner model is unstable to 2D perturbations in pressure driven channel flow both in its form as presented in this work [14] and in variants of the model [15, 16]. We study the same model again for the purposes of establishing whether or not the results obtained can be understood in the same context as those for the Rolie-Poly and Johnson-Segalman models. Thereby, we hope to establish the level of generality or otherwise for our criteria of instability of shear-thinning pressure driven channel flow across constitutive models.

We therefore consider whether the 1D base states just discussed are unstable to 2D perturbations for some value of imposed pressure drop. We plot, for a particular set of values of η and n, the growth rate of the most unstable eigenvalue $Re(\omega_q)$ as a function of wavenumber q in Figure 3.19 a). As in the previous models studied, we observe positive values of $Re(\omega_q)$ above some critical value of P', indicating the base state flow to be unstable. The dispersion relations we observe

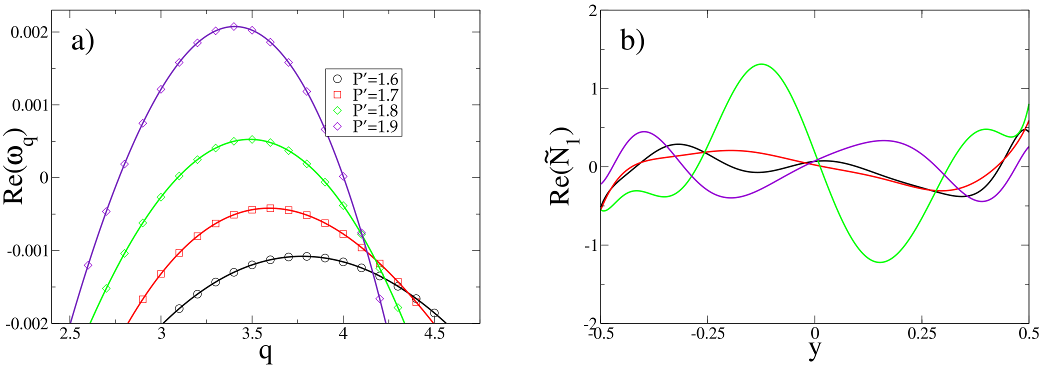

Figure 3.19: a)Dispersion relations of growth rate $Re(\omega_q)$ as a function of wavenumber for a range of applied pressure drops for the White-Metzner model with power law exponent $n = 0.2$ and solvent viscosity $\eta = 0.005$. Numerical grid $N_y = 2048$ and timestep $dt = 10^{-4}$. b) The real part of the normalised eigenfunction of the first normal stress difference $\tilde{N}_1$, $q = 3.5$.

to be reasonably similar to those of the other models studied (recall Figures 3.5 a) and 3.13 a)).

A difference is observed however when we consider the eigenfunction of the first normal stress difference $\tilde{N}_1$, as shown in Figure 3.19 b). Rather than being localised, as in the previous models considered, the eigenfunction is diffusely spread across the channel in White-Metzner. This is consistent with the model lacking either a shear-thinning plateau region, or a steep normal stress gradient localised within the channel. Instability in the White-Metzner model therefore does not appear as a displacement of a tightly focussed interfacial region, but as a disturbance that affects the flow right across the channel.

As in the other models considered in this study, we have performed a linear stability analysis for a range of η and shear thinning exponent n. The stability thresholds for WM are shown in Figure 3.20 b) for several values of solvent viscosity for $0.1 \leq n \leq 0.3$. We are not able in this study to access values of shear-thinning exponent below $n = 0.1$. The region shown demonstrates that our results agree with those from the original studies, which found that instability does not appear above $n = 0.3$ for this form of the White-Metzner model in Ref. [14].

3.9.4 Criterion for Instability Onset

In the models considered previously in this study we have constructed a criterion for the critical pressure drop based on the maximum normal stress gradient in the channel and the minimum logarithmic slope of the homogeneous flow curve $\Sigma\left(\dot{\gamma}\right)$. In the White-Metzner model, the shear thinning exponent n itself corresponds to the logarithmic slope $\frac{d\log\Sigma}{d\log\dot{\gamma}} = n$, which is constant in $\dot{\gamma}$, up to small corrections from the solvent. With the addition of a solvent viscosity this is exactly true only at the centre of the channel, but we will assume that the correction remains small for the range considered. (We discuss later where this assumption may break down for some larger values of solvent viscosity.) Accordingly we drop the subscript "min" from $\frac{d\log\Sigma}{d\log\dot{\gamma}}|_{min}$. As noted previously, the form of the flow curves and the corresponding base states means that there exists no highly localised large gradient in first normal stress across the channel. The maximum value of $\frac{dN_1}{dy}$ is now located at the wall of the channel. The derivative $\frac{dN_1}{d\Sigma}$ is therefore not taken simply from the parametric function of N_1 as a function of Σ, but by computing the stress at the wall of the channel and calculating the gradient from the corresponding value on the parametric plot.

Recall that in the RP and JS models, we have built the criterion on the basis of the existence of a quasi-interface within the channel, and in turn linking this to the shape of the homogeneous shear flow curves. The form of this criterion is given by the equations

$$\frac{dN_1}{dy}|_{max} > f\left(\frac{d\log\Sigma}{d\log\dot{\gamma}}|_{min}\right), \tag{3.61}$$

where

$$f(\zeta) = \alpha_0 + \alpha_1/(\alpha_2 - \zeta). \tag{3.62}$$

Given the absence of a quasi-interface in this model should not expect this to work for White-Metzner. However, when performing the same process as for the previously discussed models, we suprisingly do find a reasonable fit for the criterion with parameters $\alpha = 1.21$, $\alpha = 0.55$ and $\alpha_2 = 0.31$, see Figure 3.20. In the original study in Ref. [14], no instability was found for shear thinning exponents exceeding $n \approx 0.3$. Our results here confirm this finding with $\alpha_2 = 0.31$. We then reconstruct

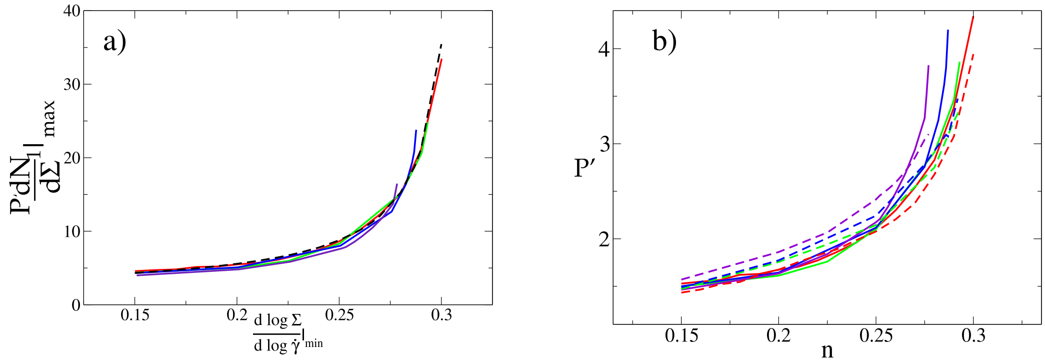

Figure 3.20: a) The expression $P'^* \frac{dN_1}{d\Sigma}|_{max}$ corresponding to the maximum normal stress gradient within the channel plotted as a function of the minimum logarithmic slope $\frac{d \log \Sigma}{d \log \dot{\gamma}}|_{min} = n$ for the White-Metzner model at different solvent viscosities $\eta = 0.005, 0.01, 0.02, 0.04$. Black dashed line: function $y = f(n)$ of Eq. 3.44 with $\alpha_0 = 1.21$, $\alpha_1 = 0.55$, $\alpha_2 = 0.31$. b) Solid lines: the corresponding curves of neutral stability $P'^*(\eta, n)$ as a function of the power law exponent n in the White-Mezner model. The flow is stable for P' below the lines and unstable for P' above. (We have not explored higher values of P' for this model so we do not know if this model will display re-entrant stability akin to the other models studied in this chapter.) Dashed lines: predicted critical pressure drop using Eqs. 3.44 and 3.43.

the pressure drops as before, finding that at low values of n the pressure drops correspond reasonably well to the numerically calculated values as shown by dashed lines in Figure 3.20. At larger values of n we see that the predicted pressure drops deviate somewhat from the measured values, possibly due to the effects of solvent becoming more significant.

Plotting the contours of n as vertical dotted lines in Figure 3.21, we see that the region of instability is not hugely affected by the presence of solvent. This is not surprising as the solvent remains a small contribution to the total stress $\Sigma = G\tau_0^n \dot{\gamma}|\dot{\gamma}|^{n-1} + \eta\dot{\gamma}$ for the range of values of solvent considered and the pressure drops explored. One may conclude therefore that the collapse in Figure 3.20 a) is a relatively trivial result. What is surprising however, is that the functional dependency observed of normal stress gradient to logarithmic slope follows the same form for White-Metzner as in Rolie-Poly and Johson-Segalman, albeit with different

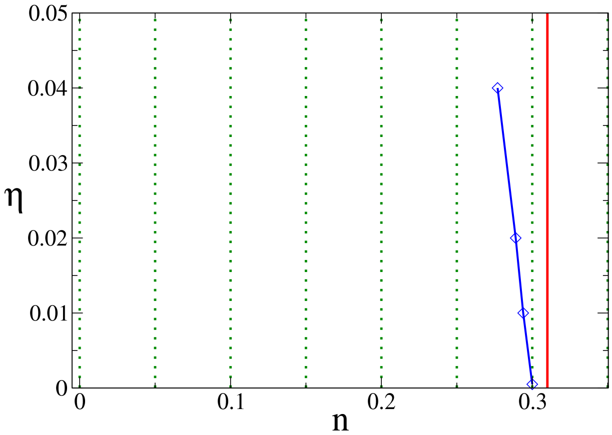

Figure 3.21: Dotted lines: contours of minimum logarithmic slope of the flow curve, $n = \dfrac{d\log\Sigma}{d\log\dot{\gamma}}|_{min}$, increasing in increments of 0.05 in contours rightwards for the White-Metzner model. The contour $n = 0.31$ is the solid red line. The maximum calculated values of logarithmic slope at which instability is observed for a given solvent viscosity (blue diamonds). This is consistent with a contour value in the range 0.277 to 0.3.

fitted parameters for α_0, α_1 and α_2.

3.10 Conclusions and Future Work

In this chapter we have combined full numerical simulation and linear stability analysis to study shear thinning viscoelastic fluids in pressure-driven channel flow using four commonly used constitutive models. We demonstrate that a 1D base state, describing a flow which is initially uniform in the channel direction, is unstable to 2D perturbations for a combination of high enough degree of shear thinning and sufficiently high pressure drop. We may speculate that the observation of instability in all models suggests that the instability may be generic for all models of shear thinning polymeric fluids.

We define the degree of shear thinning within each model as the minimum logarithmic slope of the homogeneous 1D flow curve $\frac{d\log\Sigma}{d\log\dot{\gamma}}|_{min}$. The minimum degree of shear thinning (highest value of $\frac{d\log\Sigma}{d\log\dot{\gamma}}|_{min}$ that admits instability) was determined

Model	α_0	α_1	α_2
Rolie-Poly	25.81	0.33	0.21
Johnson-Segalman	60.81	1.15	0.11
White-Metzner	1.21	0.55	0.31

Table 3.1: The fitting parameters for the three models of this chapter for which the general criterion described by Eq. 3.44 was found to fit well to the numerically calculated results. The parameter α_2 corresponds to the threshold minimum logarithmic slope for a given model of the 0D homogeneous flow curve below which a 1D base flow is found to admit instability to 2D perturbations at some value of applied pressure drop P'. Above this value the model no longer admits instability for any applied pressure drop.

to be $\frac{d\log\Sigma}{d\log\dot{\gamma}}|_{min} \approx 0.21$ for Rolie-Poly, $\frac{d\log\Sigma}{d\log\dot{\gamma}}|_{min} \approx 0.11$ for Johnson-Segalman and $\frac{d\log\Sigma}{d\log\dot{\gamma}}|_{min} \approx\approx 0.31$ for the White-Metzner model.

We find a generalised criterion by which we are able to predict to onset of instability using rheological properties taken directly from the steady state flow curves, within a reasonable approximation. That functional form is given by

$$\frac{dN_1}{dy}|_{max} > f\left(\frac{d\log\Sigma}{d\log\dot{\gamma}}|_{min}\right), \tag{3.63}$$

and

$$f(\zeta) = \alpha_0 + \alpha_1/(\alpha_2 - \zeta), \tag{3.64}$$

where the parameters α_0,α_1 and α_2 are taken from fitting numerical data. In the case of each of the three models, different fitting parameters are found to match the data. These fitting parameters are shown in Table. 3.1.

Although the functional form remains consistent, that each model requires different fitting parameters conveys that the analysis performed here is only a partial success. A true general criterion should be independent of the model to which it is applied. Future studies may shed light on how these parameters vary according to the generalisable dynamics of each model, yet this may prove unfeasible in practice.

The shear-thinning plateau region that is present in the shear-stress flow curves of both models leads to the the 1D base state having a quasi-interfacial region within the channel. In turn we see the instability presenting itself as a destabilisation of the quasi-interface in the Johnson-Segalman and Rolie-Poly models. This result suggests a similarity between the shear-thinning fluid instability studied here and those observed in shear-banded and stratified flows. In Refs. [91, 94] it was shown that instabilities between layers of fluid with differing viscosities are driven by large gradients in normal stress differences and shear rate. It was shown however in Ref. [95] that this is not the case if the viscosities are matched. The immediate question then arising is why such a criterion also applies to the White-Metzner model, which lacks such a quasi-interfacial behaviour. Our findings may then suggest that a shear thinning flow may in fact be equivalent to a very smeared interfacial flow between fluids of varying viscosities.

To test this hypothesis we consider our findings in the context of other work in literature. In a recent study by Castillo and Wilson, the authors state that "We can characterise the instability in terms of the thixoplastic number; in doing so, we found that the instability is strongest if the base-state [plateau stress Σ^*] is located near the channel-wall (at $y \approx 0.98$)." As mentioned in the introduction to this chapter, the N_1 base state of the BMP model is parabolic, with the largest gradient in first normal stress difference at the wall. We therefore suggest that the effect of the proximity of the shear-thinning plateau to the wall in fact relates to the normal stress gradient near this plateau. In the Wilson and Castillo study using a modified White-Metzner model in Ref. [16], the addition of a non-viscoelastic shear thinning solvent was found to stabilise the flow, despite retaining the same form for the base state shear rate as a function of position. Since the addition of a solvent parameter of this form will decrease the gradients of first normal stress within the channel, we may conclude that this result is consistent with our findings in this chapter. In contrast to this finding however, Refs. [95, 96] considered layered viscoelastic fluids with matched viscosities, but different relaxation times, and so normal stresses. The interface was found to be unstable even with the addition of surface tension to mitigate the effects of normal stress gradients. It therefore remains unclear whether all instabilities of this form can be directly related to the base state shear rate, normal stress and viscosity or whether or not there is some underlying dynamical property which drives the formation of secondary flows.

The spatial behaviour of the eigenfunctions seen in various studies may also suggest the underlying nature of the instability. In the case of the Rolie-Poly and Johnson-Segalman models in this study, the eigenfunctions are localised near the quasi-interfacial region of shear thinning in the channel, while in White-Metzner they are highly delocalised. In Ref. [17], the eigenfunctions are highly localised near the region of shear thinning. This suggests that although normal stress gradients may drive the instability, it is the span of the region of shear thinning within the channel that determines the form of the eigenfunctions.

In experimental studies which motivated this work we can see a number of comparisons and similarities to our own findings. The experiments of Refs. [18–20] all observe instability within a range of values of $d\log\Sigma/d\log\dot{\gamma}|_{min}$ similar to our own findings. This ranges from $\dfrac{d\log\Sigma}{d\log\dot{\gamma}} = 0.12$ in Ref. [18] to 0.29 in Ref. [20]. All three studies also report instability only when the shear-thinning region of the flow curve is within the channel, in accordance with Eq. 3.53. Finally we note that in the Ref. [18], it is observed that tracer particles begin to undulate close to the walls of the channel, near the region of shear thinning, before unsteady flow develops throughout the channel. This is similar to what is observed in RP and JS, which show the perturbation to the flow field highly localised to the region of shear-thinning in the base state.

While these aspects of our study and prior experimental work are in agreement, discrepancies exist which we must address. The foremost of these is the absence of a drag reduction in our non-linear simulations. This was observed by both Bodiguel [18] and Poole [19], who measured a flux increase (for a pressure controlled flow) and a pressure decrease (for a flow rate controlled flow). We do not observed this in our simulations. This may be attributable to a number of factors. It may be that this drag reduction is a microscopic effect and therefore not observable in a continuum model, or that some aspect of the polymer dynamics which causes this drag reduction is not replicated in RP or JS. Another factor however may relate to the location of the shear-thinning region within the channel itself. In all the experimental studies, instability appears to occur when the shear-thinning portion of the flow curve is at the channel wall, rather than some distance from it within the channel, as in our calculations. This may be due to the higher value of solvent viscosity used in our simulations as compared to experiment. In our simulations $\eta/G\tau > 10^{-3}$ for all models studied, while the equivalent values in Refs. [18–20] are $O\left(10^{-4}\right)$. Further non-linear studies, using smaller solvent viscosities, may be able to resolve these differences in our findings.

Finally, we make some remarks about how the time dependent 2D perturbations may grow. In an experiment, one may be interested to determine what length a channel must be for the fluid carried through it to become unstable. One may estimate this by considering a an average flow rate V within the channel and the magnitude of the most unstable eigenvalue $Re(\omega)$, which gives the timescale for the growth of the instability. One may estimate then that a flow will show instability if the channel length is of the order $L_x = V/Re(\omega)$. This means that any study examining the onset of such instability must ensure that channel is of sufficient length for perturbations to grow. Any study performed in an overly short channel may therefore appear stable, despite the base flow being unstable to perturbations in experiments performed in longer channels.

Further study is required to determine if our criterion predicting the onset of instability as a function of flow curve properties proposed in this work is in fact applicable to previous studies of shear thinning channel flow. In order to do this, results from the previous studies would need to be recast in terms of pressure drop and logarithmic slope. If this functional form determines the onset of instability in most models, but not all, it may yield insight into the differences between models for which this criterion works and those for which it does not. This may also offer additional benefits to the construction of constitutive models in future. In this work, we have ignored 3D effects and have assumed that Squire's theorem holds true in the regime studied. It would be worthwhile, particularly in light of the experimental results shown by Ref. [20], to perform a linear stability analysis of a fully three-dimensional flow, taking into account perturbations in both the flow and vorticity directions.

Lastly we acknowledge that due to numerical limitations we were unable to conduct fully non-linear simulations of a White-Metzner fluid. It would be interesting to see in particular if the non-linear behaviour seen in JS and RP was similar in White-Metzner, thereby showing whether or not the secondary flows developed in the same manner, despite the very different flow curves.

3.11 Appendix I - Numerical methods

The system studied in this chapter couples a dynamical equation describing the evolution of a viscoeleastic polymeric fluid to a Newtonian flow field. This study is performed using linear stability analysis and full non-linear simulation. We here describe how these systems of equations were solved numerically.

Linear Stability Analysis. The initial calculation performed as part of the linear stability analysis determines the 1D base state to which perturbations will be added. This was done by evolving to steady state the dynamical equation of the 1D conformation tensor $\mathbf{W}(y,t)$

$$\partial_t \mathbf{W}(y,t) = F(\mathbf{W}(y,t), \partial_y \mathbf{v}(y,t), \xi). \tag{3.65}$$

from which the 1D stress tensor $\sigma(y,t)$ may be calculated depending on the constitutive equation. This is coupled to the force balance condition

$$0 = \eta \nabla^2 \mathbf{v}(y,t) + \nabla \cdot \sigma(y,t) - P'\hat{\mathbf{x}}. \tag{3.66}$$

This reduces to

$$\eta \partial_y^2 U(y,t) + \partial_y \sigma_{xy}(y,t) - P' = 0 \tag{3.67}$$

The flow field is modelled using a stream-function formulation such that

$$\mathbf{v} = \nabla \times \psi. \tag{3.68}$$

The 1D stream-function is therefore related to the base velocity field by the expression

$$\mathbf{v}(y) = U(y)\hat{\mathbf{x}} = \partial_y \psi(y)\hat{\mathbf{x}}. \tag{3.69}$$

which in turn obeys the third order equation

$$\partial_y^3 \psi(y) = -\frac{1}{\eta}\partial_y \sigma_{yx}(y) - \frac{1}{\eta}P'. \tag{3.70}$$

We impose no-slip boundary conditions on the flow field such that $\mathbf{v}(y=0) = \mathbf{v}(y=L_y) = 0$ and zero-gradient on the stress perpendicular to the boundary such that $\partial_y \sigma(y=0) = \partial_y \sigma(y=L_y) = 0$.

At each time-step the flow field is solved to ensure force balance. A discretised mesh of N_y elements describes the spatial variation in $\psi\left(y\right)$ and $\sigma\left(y\right)$ with points indexed $j = 0, \cdots, N_y$, where the element j corresponds to the position $y = jL_y/N_y$. A finite difference method is used to solve the value of ψ_0 at each timestep.

The 1D stream-function described in Eq. 3.70 is solved on staggered half grid points such that

$$\partial_y^3 \psi|_{j+1/2} = \frac{1}{(\Delta y)^3}(\psi_{j+2} - 3\psi_{j+1} + 3\psi_j - \psi_{j-1}) \tag{3.71}$$

and

$$\partial_y \sigma_{yx,j} = \frac{1}{\Delta y}\left(\sigma_{yx,j+1} - \sigma_{yx,j}\right) \tag{3.72}$$

where $\Delta y = L_y/N_y$. Performing this method ensures that Eq. 3.66 is satisfied, including boundary conditions and setting the value of ψ_0 up to an arbitrary constant. To obtain the 1D base state, the Eqs. 3.65 and 3.66 are evolved to steady state. Given that there is initially no viscoelastic stress, the flow field will adopt a Newtonian profile on the first timestep such that

$$U_0(y) = -\frac{1}{2}P'(y - L_y/2)(y + L_y/2). \tag{3.73}$$

The velocity gradient tensor $\nabla\mathbf{v}$ is then calculated and the constitutive equation evolved using Euler time-stepping. This performed for each time t such that

$$\mathbf{W}\left(y, t + \Delta t\right) = \mathbf{W}\left(y, t\right) + \Delta t F\left[\mathbf{W}\left(y, t\right), \nabla\mathbf{v}\left(y, t\right)\right]. \tag{3.74}$$

The flow field is then recalculated at each time-step. This process is repeated until the system has reached a steady state. This is done by comparing the stress tensor at each time $\sigma\left(t, y\right)$ to the previous timestep $\sigma\left(t - \Delta t, y\right)$. The system is deemed to be in steady state when $\max(|\sigma\left(t, y\right) - \sigma\left(t - \Delta t, y\right)|) < \epsilon$ for all values of y, where epsilon is some small value $\epsilon \ll 1$.

This base state is used for calculating the evolution of the perturbations $\tilde{\sigma}\left(y, t\right)$ and $\tilde{\mathbf{v}}\left(y, t\right)$ and is assumed not to vary while these perturbations evolve. The evolution of these perturbations is measured during t_{lin}, where $t_{lin} = 0$ corresponds to the timestep at which the perturbations are first added to the base state. The following equation describes the evolution of the perturbation to the conformation tensor

$$\partial_t \tilde{\mathbf{W}} + iqU_0\tilde{\mathbf{W}} + \tilde{u}iq\mathbf{W}_0 + \tilde{v}\partial_y\mathbf{W}_0 = F\left(\mathbf{W}_0 + \tilde{\mathbf{W}}, \nabla\mathbf{v}_0 + e^{-iqx-\omega t}\nabla\tilde{\mathbf{v}}e^{iqx+\omega t}, \xi\right). \tag{3.75}$$

where $\tilde{\mathbf{W}}_q$ and $\tilde{\mathbf{v}}_q$ are the perturbation conformation tensor and velocity field respectively corresponding to wavenumber q. The perturbation streamfunction $\tilde{\psi}_q$ then obeys the equation

$$(q^4 - 2q^2\partial_y^2 + \partial_y^4)\tilde{\psi} = \frac{1}{\eta}[(-q^2 - \partial_y^2)\tilde{\sigma}_{xy} - iq\partial_y(\tilde{\sigma}_{xx} - \tilde{\sigma}_{yy})]. \tag{3.76}$$

This fourth order differential equation solves the perturbation flow field according to the evolution of the perturbation stress tensor. Over time the perturbation stress-tensor and stream-function will correspond to the eigenfunction of the mode for the largest value of $Re\,(\omega_q)$. If $Re\,(\omega_q) > 0$ the amplitude of these modes will grow in time. The evolution of the eigenfunction will also depend on the imaginary part of the eigenvalue $Im\,(\omega_q)$. The value of the imaginary part of the eigenvalue determines oscillation in amplitude of the real and imaginary parts of the eigenfunction.

The flow field is solved using a finite difference method at each timestep. Following this the perturbation velocity gradient tensor $\nabla\tilde{\mathbf{v}}$ and hence the perturbation stress tensor $\tilde{\sigma}$ are updated. The local terms on the right hand side of Eq. 3.75 are evolved using Euler time-stepping, while those of the left hand side which correspond to the advective quantities are evolved using a fourth order Runge-Kutte method. This combination of time-stepping methods ensures numerical stability while preventing the calculations becoming numerically expensive.

Non-linear Simulation. The non-linear simulations in this study are performed using a combination of finite difference and Fourier methods. The channel is periodic along the $\hat{\mathbf{x}}$ direction, with fixed walls at the points defined by $y = -L_y/2$ and $y = L_y/2$. In both directions this is discretised on a grid, with index $i = 0, ..., N_x$ along the flow direction and $j = 0, ..., N_y$ in the cross channel direction. The method by which the system of equations are evolved may be outlined as follows;

Step 1: A Discrete Fourier transform along the channel direction is performed on the stress tensor $\sigma\left(x,y\right) \rightarrow \tilde{\sigma}_q\left(y\right)$.

Step 2: The flow field is solved using a stream-function formulation in Fourier space. The zeroth mode is solved at staggered half grid points, while non-zero modes are solved on each grid point.

Step 3: The stream-function is then inverse transformed to real-space and used to calculate the local velocity field: $\mathbf{v}(x,y)$ and rate of strain tensor: $\nabla\mathbf{v}(x,y)$.

Step 4: Local stress terms are updated by Euler time-stepping the local terms of the constitutive equation.

Step 5: Third order upwinding is used to calculate the derivatives of the stress tensor components. Following this advective terms are updated using a fourth order Runge-Kutte time-stepping method.

This is repeated until the system is deemed to have reached a steady state which is assessed via inspection of the amplitude of Fourier modes of the stress tensor components. The dynamics of the system are deemed to have reached a steady state once the mode amplitudes have saturated.

Chapter 4

Ductile to Brittle Yielding in Soft Glassy Materials

4.1 Introduction

Amorphous materials are defined by a lack of an ordered microstructure. This category includes soft materials such as dense colloidal suspensions, foams, gels and emulsions [44, 45, 124–126]. It also includes hard solids, such as molecular and metallic glasses [127, 128]. For these materials, an elastic regime at low deformations transitions to a plastic regime at high deformations. This may occur rapidly, which is known as brittle yielding [129, 130], or in a more gradual manner known as ductile yielding [27, 65, 131]. In this chapter, we study the effects of sample preparation and the rate of deformation on this process.

Many of these materials are what are known as yield stress fluids, which include foodstuffs such as ketchup [7] and mayonnaise [8]. Despite their ubiquity, the physical mechanisms behind their rheology remain an active area of study [31]. The flow curves of yield stress fluids often follow the Heschel-Bulkley model [132, 133],

$$\begin{aligned} \Sigma < \Sigma_y \Rightarrow &\quad \dot{\gamma} = 0 \\ \Sigma \geq \Sigma_y \Rightarrow &\quad \Sigma\left(\dot{\gamma}\right) = \Sigma_y + K\dot{\gamma}^n. \end{aligned} \tag{4.1}$$

The fluid described by these equations, when subjected to an applied shear stress Σ, only flows if the applied shear stress exceeds the "yield stress" Σ_y. At low applied shear-stress, the sample will deform reversibly. As the applied stress increases, creep may be observed [134]. For applied shear-stress above the yield stress Σ_y, the material will yield and fluidise [38]. The exponent n determines the shear-thinning properties of fluid. This model is an extension of the original proposed by Bingham, which first introduced the concept of yield stress fluids [46]. Bingham's original model is recovered for the Herschel-Bulkley model with $n = 1$.

This yield stress behaviour emerges effectively from the inability of the microstructure to deform quickly enough to release the stress created due to macroscopic deformation. The yield stress of these fluids is often a function of temperature [135] and packing fraction [136]. Soft glasses, such as dense colloidal systems, are among the best studied of these yield stress fluids.

"Non-Brownian" systems describe materials with microstructures that are large enough such that thermal effects become negligible. The emergence of a yield stress in soft athermal materials can sometimes be described as a static transition from a qualitiative change in the microstructural properties of the material [137].

While undergoing small deformation, elastoviscoplastic materials behave as elastic solids such that $\Sigma \sim G\bar{\gamma}$. At larger strain, the material transitions to a fluid like state, where the shear-stress Σ is a function of the shear-rate $\dot{\gamma}$. In some materials, this initial regime of elastic behaviour may dramatically overshoot the steady state stress before yielding. Following this, the stress decreases to its steady state value. This difference between the maximum value of the start-up curve and the steady state stress will be referred to as the overshoot height in the ensuing study.

"Brittle" and "Ductile" yielding

In the shear start-up protocol, a constant average shear-rate $\bar{\dot{\gamma}}$ is applied to a material sample for all times after some initial switch on time $t = 0$. The resulting shear-stress, Σ, is then measured as a function of the applied average strain $\bar{\gamma}$. If the induced flow remains homogeneous, every part of the sample undergoes an equal measure of strain $\gamma = \bar{\gamma}$. For a Newtonian fluid in the limit of zero inertia, the stress response is instantaneous and the shear-stress $\Sigma = \eta\bar{\dot{\gamma}}$, where η is the fluid

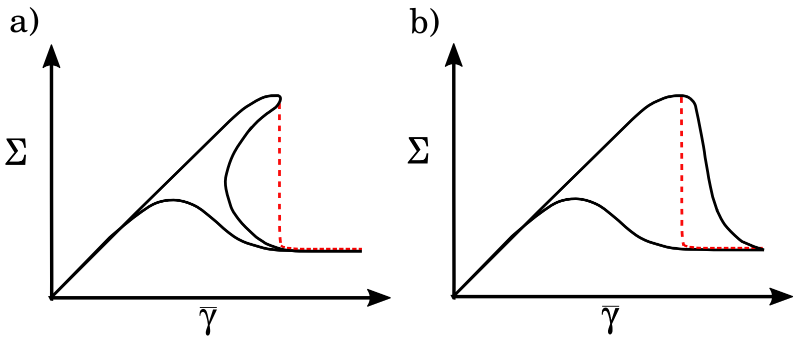

Figure 4.1: Schematic of shear stress versus strain in two possible scenarios for ductile versus brittle yielding: **a**) as suggested in Ref. [22] and **b**) as is suggested in this work. In each diagram the lower curve corresponds to a less well annealed sample, which shows "ductile" yielding. The upper curve displays brittle yielding and is better annealed. Solid line: theoretical curve in which homogeneous shear is artificially enforced. Dotted line: discontinuous change in stress overhang, or drop from homogeneous curve due to shear banding.

viscosity.

In particle simulations, yielding is associated with a decrease in stress during start-up [22–24, 138]. These simulations were performed in the limit $\bar{\dot{\gamma}} \rightarrow 0$, using a protocol known as Athermal Quasistatic Shear or AQS [139], as well as at finite shear-rates. Yielding was found to become increasingly sharp with decreasing shear-rate and better annealing prior to shear. The increasingly brittle nature of the yielding observed with decreasing shear-rate is such that simulations performed in the limit of $\dot{\gamma} \rightarrow 0$ show a discontinuous change in stress as a function of average shear-strain for well annealed samples.

Refs. [22, 23] proposed that the transition from ductile to brittle yielding was attributable to a reversal in the direction of the homogeneous stress-strain start-up curve as sketched in Figure 4.1 a). This theory describes the mechanism for yielding in terms of spinodal phase transition [140–144].

In this work, we present an alternative hypothesis to explain this phenomenon. We propose instead that brittle yielding results from a homogeneous flow becoming unstable to the formation of heterogeneous shear rate. As theorists, we are able to produce homogeneous start-up curves by enforcing a constraint upon the system, leading to no spatial variation within the flow geometry considered. We compare the evolution of the shear-stress of a homogeneous flow to the shear stress of a heterogeneous flow and show that abrupt yielding behaviour can be observed for materials with homogeneous start-up curves as sketched in Figure 4.1 b). We use the term brittle to characterise abrupt yielding in which the rate of failure is much larger than the rate of imposed deformation, and in which the strain becomes strongly localised within the sample. The term ductile is used to describe yielding which occurs more slowly compared to the rate of applied strain and in which we see no such strong localisation.

We show that the emergence of brittle yielding may be understood as a dynamical process caused by the emergence of flow heterogeneities during yielding, as observed in Ref. [145]. This occurs without any qualitative change in the homogeneous start-up curve. The transition from continuous to a discontinuous yielding, with corresponding formation of shear-bands, was recently observed in particle simulations performed by Singh, Ozawa and Bethier [24]. In this work, we examine the link between yielding and the formation of transient shear bands using a mesoscopic model, which we will show to be effective in reproducing the results of particle simulations.

Transient Shear Banding

When subject to an imposed average shear-rate, an initially homogeneous flow profile with shear-rate $\dot{\gamma}$ invariant in space, may become unstable to the emergence of spatially varying shear-rates. Parts of the sample yield and fluidise, while other unyielded regions of the sample continue to deform in the manner of a soft-solid. These yielded and unyielded regions of the sample then experience different shear-rates corresponding to their local material properties.

As the sample is subjected to further shear, the fluidised band grows until the system has reached an entirely fluidised plastic state. Subsequently, the shear-rate is once again uniform throughout the sample. Time dependent heterogeneous flow of this manner is known as transient shear-banding. Previous research has shown that during shear start-up, many soft materials, such as carbopol gels [13, 27, 64], foams [146, 147] and clay suspensions [73, 148] display this emergent flow heterogeneity.

The study undertaken here proceeds from the extensive theoretical work of Fielding and collaborators, who have used a wide variety of constitutive models to study transient shear banding [25, 68, 69]. In Ref. [68] they derived criteria for the formation of transient shear bands in polymeric materials. In a shear start-up protocol, this was found to require a stress overshoot and subsequent yielding of the material. This connection between the stress overshoot and the formation of shear bands has also been observed in soft glassy materials [149, 150]. Our work presented here aims to substantiate and quantify this connection. We do so using the soft glassy rheology model previously utilised to study transient shear-banding [25, 151], but with several novelties unique to this work.

4.2 The Soft Glassy Rheology Model

The "soft glassy rheology" or SGR model describes soft materials with a disordered structure such as emulsions and dense colloidal suspensions [152]. In this model, material locally deforms elastically until the local energy barrier for a plastic yielding event is overcome. The SGR model represents this in terms of a particle in an energy well which gains elastic energy through deformation. Given sufficient energy, the particle may hop out of its energy well.

A sample of material is described using an ensemble of these SGR elements. Each element has local deformation described by the quantity l. For every element, there is a corresponding energy well depth E and the local material strain is described by the microscopic conformation tensor $\mathbf{W}$. The complete local deformation is quantified as $l = \sqrt{(\mathbf{W} - \mathbf{I}) : (\mathbf{W} - \mathbf{I})}$. These particles gain energy per unit volume $\frac{1}{2}Gl^2$, via the application of external deformation to the element. The quantity $\dot{\gamma}$ is the macroscopic (global) rate of deformation and G is the microscopic elastic shear-modulus with units of stress. Throughout this chapter $G = 1$, thus setting the unit of stress for our calculations. In experimental studies, G may have

SI units of Pascals.

Before the onset of deformation, the macroscopic strain is zero: $\langle l \rangle = 0$. This is achieved by setting all the microscopic strains $\mathbf{W} = \mathbf{I}$, before strain is imposed. Between yielding events, $\dot{\mathbf{W}} = 2\mathbf{D} = \nabla \mathbf{v} + \nabla \mathbf{v}^T$. The quantified strain $\dot{l} \sim \dot{\gamma}$ until the particle escapes the energy well and the element yields. Upon yielding $\mathbf{W}$ is set to $\mathbf{I}$, and thus l is reset to zero. A new energy well depth $E^{'}$ is chosen from an exponential distribution $\rho(E^{'}) = e^{-E^{'}/T_g}$. A schematic of the particle picture is shown in Figure 4.2. T_{g} is defined as the *glass transition temperature* in the Bouchaud trap model [153–155], which corresponds to the SGR model without flow. $T_{\mathrm{g}} = 1$ for this study, providing the unit of temperature throughout.

The distribution of trap energies $P\left(E, l, t\right)$ obeys the governing equation

$$\dot{P} + \dot{\gamma}\partial_l P = -\Gamma(E, l)P + \rho(E)\delta(l)\left\langle \Gamma(t) \right\rangle . \tag{4.2}$$

The second term on the left hand side of this equation describes the increase in strain energy of particles in between hopping events due to external deformation. The first term on the right hand side describes particles hopping out of their traps and the right-most term describes the selection of a new trap energy for the particle post yielding event. $\langle \Gamma(t) \rangle$ is the average yielding rate over all elements

$$\langle \Gamma(t) \rangle = \int \Gamma(E, l, t)P(E, l, t)dEdl. \tag{4.3}$$

The hopping rate for each element is given by

$$\Gamma(E, l) = \Gamma_0 \mathrm{min}\{\exp\left[-(E - \frac{G}{2}l^2)/T\right], 1\}, \tag{4.4}$$

where T is the effective noise temperature and Γ_0 is the microscopic-hopping rate. Our unit of time for the system is set by fixing $\Gamma_0 = 1$.

Imposing a limit to the hopping rate (set to 1 for $E > Gl^2/2$) is an ammendment to the original soft glassy rheology model in line with the recommendations of Ref. [156]. This modification introduces thermodynamic self-consistency. This changes the behaviour of the model in only a minor fashion compared to the original SGR model, which had no limitation. This modification means that in the limit of $T \to 0$, this function becomes a Heaviside step, such that the rate of hopping is

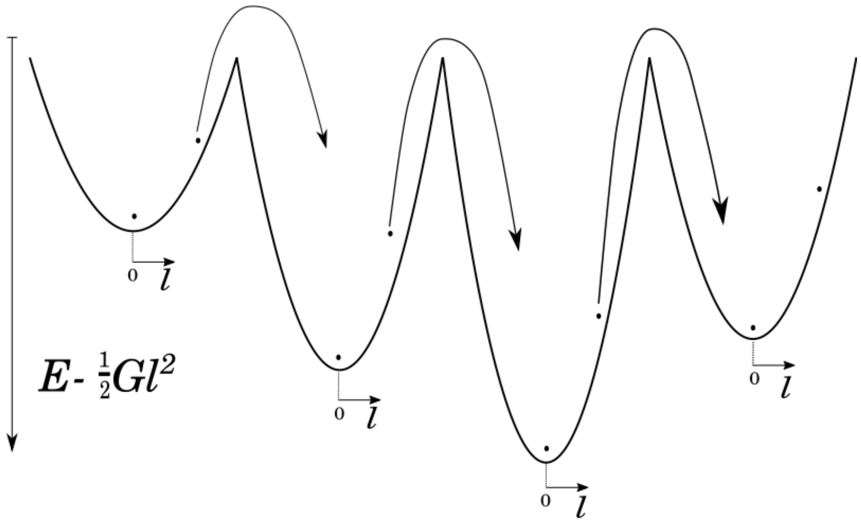

Figure 4.2: Particle hopping in the SGR model. Plastic strain energy $E = \dfrac{1}{2}Gl^2$ is gained via external deformation at a rate $\dot{l} \sim \dot{\gamma}$. The rate of "hopping" is dependent on the noise temperature T. After escaping an energy well, any particle then enters a new well with energy depth E' chosen from a prior distribution $\rho(E') = e^{-E'/T_g}$, which is uncorrelated to the previous energy well depth. Figure is adapted from Ref. [152].

zero below the energy threshold and 1 above. This enables us to explore the athermal limit of soft glassy systems, where previously such calculations could not be performed with this model.

The effective noise temperature T is a phenomenological factor which, when introduced, aimed to describe the interactions between yielding events in the system in a mean field manner. The noise is not generally thermal in origin, unless the depths of the energy wells are of comparable magnitude to k_BT. In this study, however, we consider T to be equivalent to a real thermal temperature. We see that this interpretation reproduces extremely well the results of simulations which model thermal effects on annealing prior to start-up [22,28,29,32]. Experiments on ageing soft materials also show similar results to those seen in the SGR model at non-zero noise temperature [21,73], so we may assume that the effective noise temperature used in this study is valid for modelling the properties of thermal materials.

The constitutive curve of the viscoelastic stress, depending on the effective noise temperature, follows the expression [156–158]:

$$\begin{array}{lll} \text{Newtonian regime } \Sigma \propto \dot{\gamma} & \text{for} & T > 2 \\ \text{Power law regime } \Sigma \propto \dot{\gamma}^{T-1} & \text{for} & 1 < T < 2 \\ \text{``Glass phase'' } \Sigma - \Sigma_y \propto \dot{\gamma}^{1-T} & \text{for} & T < 1 \end{array} \tag{4.5}$$

For an effective noise temperature below T_g, the constitutive curve displays a yield stress $\Sigma_y(T)$. For $T > T_g$, in the absence of applied shear, $P(E, l, t)$ evolves to a Boltzmann distribution as $t \to \infty$. For $0 < T < T_g$, the equilibrium distribution is non-normalisable. The system is considered to be in the glass phase and particles evolve into deeper traps over time. The average hopping-rate $\langle \Gamma(t) \rangle$ therefore decreases as a function of time. This corresponds to sample ageing.

When steady shear is applied, the process of ageing is interrupted by the evolution of the elastic energy so that particles in even the deepest wells can escape. Age dependent materials have been previously studied by Fielding and collaborators with SGR, using it to model shear start-up, step-strain, step-stress, large amplitude oscillatory shear and extensional flows [25, 69, 151, 159, 160]. The transient response during shear start-up has been previously found to be strongly age dependent in both experiment [21] and in previous calculations performed with the SGR model [25]. This transient behaviour is determined by the distribution of energy well depths of the ensemble of elements prior to the application of deformation. Later in this chapter, we see how the preparation of the sample prior to shear affects this distribution.

Particles cannot escape energy wells at $T = 0$ in absence of applied deformation, therefore the sample will not age. Yield stress fluids that do not exhibit ageing effects are considered to be athermal "non-Brownian" materials. We perform calculations in this limit for the first time using the SGR model and show that it is remarkably effective at replicating behaviours seen in simulations performed at the athermal limit [22, 24, 29, 32].

In this chapter, we perform all calculations in 1D. The flow is therefore assumed to only vary in the flow gradient direction $\hat{\mathbf{y}}$ and is invariant in the flow direction $\hat{\mathbf{x}}$. This tensorial representation therefore reduces to a scalar picture and

$l = \sqrt{W_{xy}^2 + W_{yx}^2}$. $W_{xy} = W_{yx}$ due to the required symmetry of the conformation tensor $\mathbf{W}$ for isotropic materials, hence the local deformation on each element is given by $l = \sqrt{2}W_{xy}$. The elastoplastic shear-stress σ_{xy} for each element is defined as $\sigma_{xy} = GW_{xy}$.

Using the soft glassy rheology model to study shear start-up, we examine the onset of yielding in amorphous thermal and athermal yield-stress fluids. Our study characterises the variation in the yielding process from a ductile, smooth transition, to rapid, brittle behaviour. We explore the stress response and the development of heterogeneous flow for samples subjected to different pre-shear protocols and imposed average shear-rates $\bar{\dot{\gamma}}$. Within the framework of each of these protocols, we demonstrate how the stress response of the materials varies with respect to sample preparation. We also characterise the effects of varying the applied average shear-rate $\bar{\dot{\gamma}}$.

We see that yielding is highly dependent on the degree of annealing that the sample undergoes prior to shear. This is true of systems with both zero and non-zero effective noise temperature. Our findings show that, depending on the applied shear-rate, thermal and athermal materials may behave quite differently during start-up. In all cases, we demonstrate that sudden yielding corresponds to the formation of shear-bands in the sample. Despite this, we see differences between protocols that apply to shear with and without $T = 0$.

4.3 Flow Geometry

In the study that follows, we assume the flow to vary only in the cross channel direction $\hat{\mathbf{y}}$ and to be uniform along the $\hat{\mathbf{x}}$ direction. To simulate this, we divide the flow into $j = 1, ..., N$ streamlines. On each streamline we take $i = 1...M$ SGR elements. The elastoplastic stress on each streamline is taken to be the average of the stress on each element along the streamline $\sigma_{xy}\left(j\right) = \frac{1}{M}\sum_{i=1}^{M}\sigma_{xy}(i, j)$.

It is important that we mitigate the stochastic effects of the SGR model on the measured quantities. We therefore perform multiple calculation for every set of parameters, using a different random number seed for each calculation. We perform each calculation fifty times for each set of parameters and take an average value of each measured quantity. To ensure the stress response of the system remains as consistent as possible between calculations performed, we increase the number of elements per streamline until we no longer observe a substantial variation in start-up behaviour between calculations performed for different random number seeds. Likewise, we introduce a fixed initial perturbation to the energy well depth from streamline to streamline such that $E(i,j)+\delta E\left(j\right) = E\left(i,j\right)\left[1+\epsilon\sin\left(2\pi j/N-\frac{\pi}{4}\right)\right]$, where $\epsilon = 10^{-3}$. This ensures the consistent formation of a single band in each calculation, further mitigating how stochasticity affects our results. The magnitude of the perturbation ϵ is selected to be sufficiently large that it overcomes any residual noise effects due to the finite number of particle elements per streamline.

For all data in this study $M = 8\times10^4$ elements are used for each streamline, with $N = 20$ streamlines to describe the spatial variation in the shear direction. Alongside the stress described by the SGR elements, we introduce a solvent with small Newtonian viscosity $\eta = 0.01$. This solvent may represent a true solvent in the system, such as that in a solution of particles. It may, however, also correspond to modes which evolve much more quickly than those which are described by the SGR dynamics.

In order to introduce diffusive coupling between streamlines, we apply a diffusivity parameter D with periodic boundary conditions. This creates a non-local coupling between streamlines, acting analogously to diffusive terms in continuum models used to study shear-banded systems [161, 162]. We set the diffusivity parameter $D = 0.05$ as in Ref. [25]. This is described in further detail in Appendix I of this chapter.

We calculate start-up curves for a homogeneous flow by evolving the shear-stress for each element at the imposed shear-rate $\overline{\dot{\gamma}}$. The corresponding start-up curves for a system where heterogeneous flow is permitted are calculated by allowing the shear-rate to vary between streamlines. For each streamline $j = 1,...,N$, every element on the streamline will experience a shear-rate $\dot{\gamma}\left(j\right)$. The value of $\dot{\gamma}\left(j\right)$ is determined by force balance, as described in Appendix I of this chapter. For simplicity, we shall refer to the start up curves for which homogeneous flow is enforced as homogeneous start-up curves. Start-up curves for which the flow is allowed to become heterogeneous are, in turn, referred to as heterogeneous start-up curves. We should note, however, that although the shear-rate may vary between streamlines, force balance means that the total shear-stress on each streamline $\Sigma\left(j\right) = \sigma_{xy}\left(j\right) + \eta\dot{\gamma}\left(j\right)$ is the same for all streamlines. The total shear-stress is therefore always homogeneous throughout the system.

The degree of banding and rate of yielding

The thesis of this work is to show that the emergence of shear-bands is closely related to the sudden stress drop observed during start-up for well annealed amorphous materials. We quantify these effects in the following manner.

In order to account for the presence of heterogeneity due to systemic noise in our model, we chose to define the degree of banding $\Delta\dot{\gamma}$ by the root-mean-squared deviation of the shear-rate

$$\Delta\dot{\gamma}\left(t\right) = \frac{1}{N}\sum_{j=1}^{N}\sqrt{\left(\dot{\gamma}\left(j,t\right) - \bar{\dot{\gamma}}\right)^2}. \tag{4.6}$$

The maximum degree of banding $\Delta\dot{\gamma}_m$ is the largest value obtained for $\Delta\dot{\gamma}$ during shear start-up. The normalised value $\frac{\Delta\dot{\gamma}_m}{\bar{\dot{\gamma}}}$ then reflects variation in the flow relative to the average shear-rate.

The yielding behaviour observed in this study varies as a function of annealing and shear-rate. To quantify this variation, we define the severity of yielding by the maximum negative slope of the start-up curve

$$\mathrm{M}^* = \max(-\frac{d\Sigma}{d\gamma}). \tag{4.7}$$

A similar measure is used in Ref. [24] to measure the severity of yielding in simulation. By use of these quantities, our study finds the variation in yielding and the degree of banding to closely follow one another for each protocol examined.

In order to account for the variation due to the use of different random number seeds, each calculation is performed 50 times, and the average value of M^* or $\Delta\dot{\gamma}_m/\dot{\gamma}$ plotted. The standard deviation has been included with each reported value and is represented by error bars in the subsequent figures.

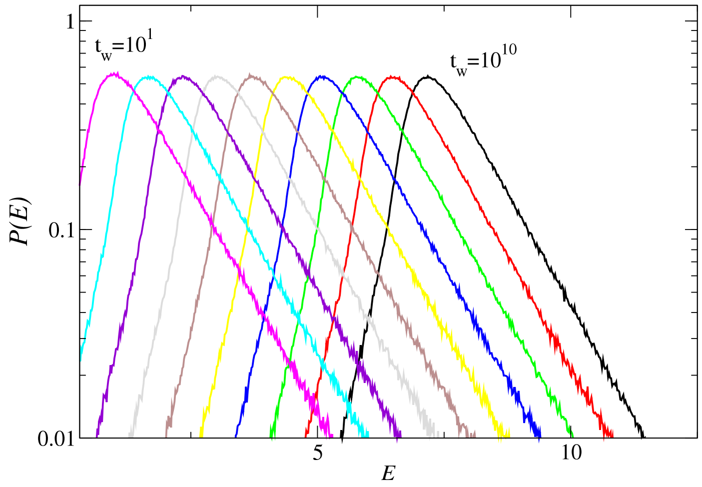

Figure 4.3: Distributions of energy well depths for the SGR model aged at $T = 0.3$ from a system quenched from $T = \infty$. The distributions move towards deeper wells with increasing age. Distributions shown correspond to ages, increasing left to right, of $t_w = \{10^1, 10^2, 10^3, 10^4, 10^5, 10^6, 10^7, 10^8, 10^9, 10^{10}\}$. The histogram is composed by sampling from a grid of $N = 1.6 \times 10^6$ elements.

In this study, we examine yielding in amorphous materials subject to three different preparation protocols prior to shear being applied. The first models an aged thermal material sheared at a fixed non-zero noise temperature. The second protocol entails cooling the material to the athermal limit from $T_{\text{init}} > T_{\text{g}}$ at a fixed rate prior to the application of shear. The final protocol we study models a material that is quenched infinitely quickly from $T_{\text{init}} > T_{\text{g}}$ to $T = 0$ before shear is applied. We explain in greater detail the particular aspects of each protocol in what follows.

4.4 Protocol I

This protocol models a thermal yield stress fluid aged for some waiting time t_w prior to start-up. The system is quenched from an initially infinite temperature, such that $P(E) = \rho(E) = e^{-E/T_g}$ for all energy wells, to some value $0 < T < T_g$. In all calculations performed here for this protocol, we set $T = 0.3$. The sample is

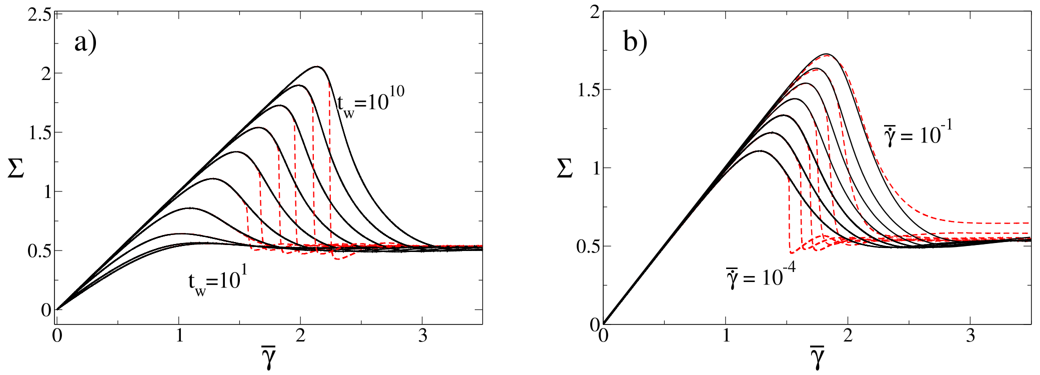

Figure 4.4: Shear start-up curves depicting homogeneous (solid lines) and heterogeneous (broken lines) start-up for a) fixed average shear-rate $\bar{\dot{\gamma}} = 0.001$ and a range of ageing times $t_w = 10^1, 10^2, 10^3, ..., 10^{10}$, with height of the stress overshoot height increasing with increasing sample age. b) fixed sample age $t_w = 10^6$ and varying shear rate, $\bar{\dot{\gamma}} = 10^{-4}, 10^{-3.5}, 10^{-3}, ..., 10^{-1}$. Height of the stress overshoot increases with increasing shear-rate.

allowed to evolve at this temperature without applied shear until the waiting time t_w has been reached. Following this, a fixed average shear rate $\bar{\dot{\gamma}} > 0$ is applied. The noise temperature is maintained at the same fixed value during both the ageing process and during start-up.

The distribution of energy well depths at the end of the ageing time and prior to the application of shear is shown in Figure 4.3 for several values of t_w. For each protocol, the distribution of energy wells prior to shear illustrates how the variation of the initial state of the system depends on how the sample is prepared. We observe that the mean of the distribution of energy wells increases with age, corresponding to more elements in deeper wells. With increasing average well depth, the sample becomes better annealed. We see that this causes the initial elastic regime to persist to larger strain, leading to a larger overshoot.

4.4.1 Stress Response

The evolution of the shear stress as a function of average strain $\bar{\gamma}$ is plotted in Figure 4.4 for both homogeneous and heterogeneous start-up curves. We reiterate that the homogeneous start-up curves represent the material stress response calculated by imposing the constraint that heterogeneities are not formed between streamlines. To calculate this, we enforce the imposed average shear-rate $\overline{\dot{\gamma}}$ upon every streamline (and by extension each element) in the sample. The heterogeneous curves allow for streamlines to have different shear-rates dependent on force balance as discussed. In so doing, we see how the heterogeneous dynamics differ from the theoretical homogeneous start-up curves.

We observe in Figure 4.4 a) that as the age of the sample increases at a fixed shear rate, so too does the height of the overshoot, as is seen in experiments of age-dependent materials [21]. Initially, all the homogeneous and heterogeneous curves overlap, demonstrating the flow to remain homogeneous at small strains. Behaviour at larger strains differs according to the sample age. For smaller values of waiting time t_w, the curves continue to overlap as the material yields, so the process is ductile. For longer ageing times, the heterogeneous curves break off from the homogeneous curves after the apex of the overshoot, showing more brittle behaviour.

In Figure 4.4 b) the start-up curves for a fixed sample age are plotted as calculated for different values of $\overline{\dot{\gamma}}$. We see that the overall height of the overshoot decreases as a function of the applied average shear-rate $\overline{\dot{\gamma}}$. Such behaviour is in line with the property that the overshoot for this protocol is set by the value of $\overline{\dot{\gamma}}t_w$ [163]. For the combination of shear-rate and sample age shown, we see the heterogeneous curve breaks off from the homogeneous curve at some value of strain after the peak of the overshoot. Despite the decreasing overshoot height, yielding for curves that permit heterogeneity is more brittle with decreasing shear-rate. We now characterise this yielding via the quantity M^* introduced previously.

The calculated values of M^* in Figure 4.5 are the average values taken from fifty start-up calculations. In Figure 4.5 a) these calculations are performed for a range of sample ages at fixed $\overline{\dot{\gamma}} = 10^{-2}$ and $\overline{\dot{\gamma}} = 10^{-3}$. For the shorter waiting times plotted, the curves follow similar trends, with the M^* being lower for the $\overline{\dot{\gamma}} = 10^{-3}$ curve. A transition occurs between $t_w = 10^4$ and $t_w = 10^5$, and M^* is larger for $\overline{\dot{\gamma}} = 10^{-3}$ than $\overline{\dot{\gamma}} = 10^{-2}$ for samples with longer waiting times. This occurs despite the overshoot height for the lower shear-rate curves being smaller that those for a larger shear-rate.

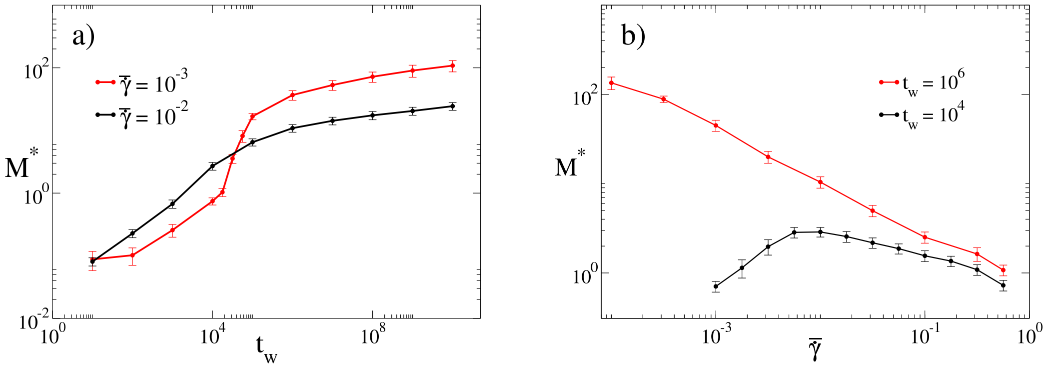

Figure 4.5: The maximum negative slope M* of the start-up curves averaged over 50 start up curves a) for fixed average shear-rate $\bar{\dot\gamma}$ and varying t_w. b) for fixed t_w and varying $\bar{\dot\gamma}$. Error bars depict standard deviation of calculated values.

Figure 4.5 b) plots M* over several decades of applied average shear-rate $\bar{\dot\gamma}$ for $t_w = 10^4$ and $t_w = 10^6$. The dependence observed is non-monotonic for $t_w = 10^4$, with a peak near $\bar{\dot\gamma} = 10^{-2}$. The yielding behaviour for this material, which is ductile at high shear-rates, becomes more brittle with decreasing shear-rate. It becomes ductile again as the shear-rate further decreases. We speculate that a similar trend could be observed for the $t_w = 10^6$ curve at smaller shear-rates. However, such values are inaccessible for this study.

4.4.2 Flow Heterogeneity

The evolution of the degree of banding $\Delta\dot\gamma\left(\bar\gamma\right)$ as a function of average strain is shown in Figure 4.6. We observe a large degree of banding upon yielding, followed by a persistent smaller value at larger strains. This second part of the evolution of the banding corresponds to the system gradually fluidising. We re-examine this protocol in Chapter 5 of this thesis to study the development of these bands with strain.

As the sample age increases, the duration of the peak becomes shorter, similar to the increasingly sudden yielding observed in the start-up curves. In Figure 4.6 a) we observe that for increasing sample age, the maximum degree of banding grows steadily, whereas the duration of the peak remains relatively constant. Figure 4.6 b) shows the evolution of the banding for several applied average shear-rates. As the

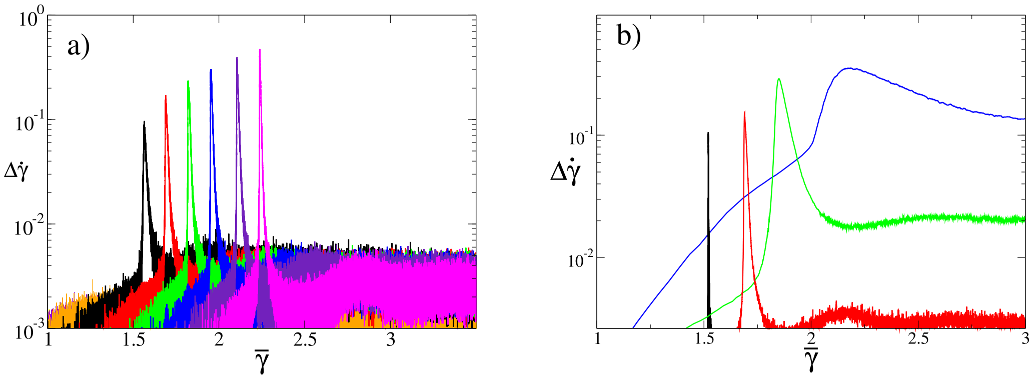

Figure 4.6: The unnormalised degree of banding during start-up as a function of average strain for a) fixed imposed average shear-rate $\bar{\dot{\gamma}} = 0.001$ for (varying left to right) $t_w = \{10^5, 10^6, 10^7, 10^8, 10^9, 10^{10}\}$. b) sample age $t_w = 10^6$ for applied average shear-rates $\bar{\dot{\gamma}} = \{10^{-4}, 10^{-3}, 10^{-2}, 10^{-1}\}$.

shear-rate decreases, the maximum amplitude of the banding also decreases slightly.

As for the case of M*, the maximum degree of banding $\Delta\dot{\gamma}_m$ is calculated 50 times for each set of parameters t_w and $\bar{\dot{\gamma}}$. We normalise this quantity relative to the applied average shear-rate to characterise the degree of banding relative to the flow. In Figure 4.7 we plot $\Delta\dot{\gamma}_m/\bar{\dot{\gamma}}$ for a range of values of t_w and $\bar{\dot{\gamma}}$. The values used in this figure are the same as those used in Figure 4.5 in relation to M*.

In Figure 4.7 a) we observe a similar trend in $\Delta\dot{\gamma}_m/\bar{\dot{\gamma}}$ as in M* in Figure 4.5 a). The cross over in yielding rate between $t_w = 10^4$ and $t_w = 10^5$ is also seen here for the degree of banding. The variation in $\Delta\dot{\gamma}_m$ as a function of shear-rate for fixed sample age is shown in Figure 4.7 b). We once again obtain the non-monotonic curves observed in Figure 4.5 b) for M* for $t_w = 10^4$.

The relationship observed here between M* and $\dot{\gamma}_m/\bar{\dot{\gamma}}$ for all values of $\bar{\dot{\gamma}}$ and t_w present the first evidence of a connection between brittle yielding and the formation of shear-bands. We performed these calculations for fixed shear-rate at varying sample age, and vice versa. Due to the computational intensiveness of the SGR model, we have not performed a full examination of the $\bar{\dot{\gamma}}$, t_w parameter space. We may, however, compare our findings to that of a fluidity model, which provides a simpler, less computationally expensive method of studying a yield stress fluid of this type.

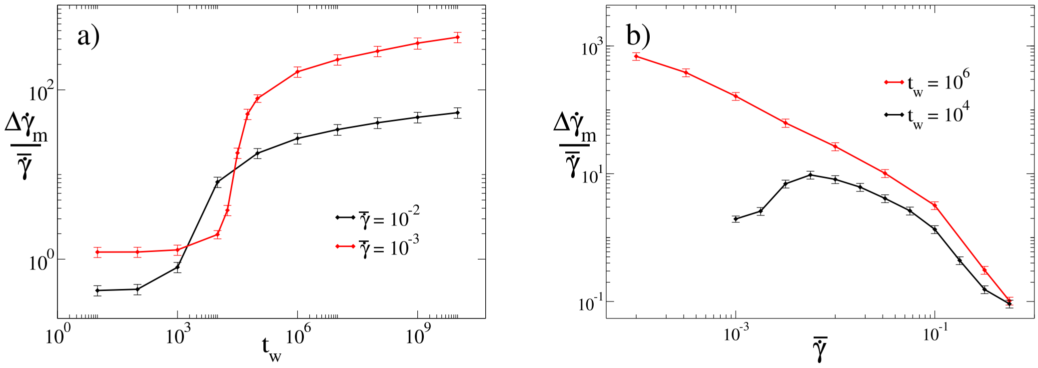

Figure 4.7: The normalised maximum degree of banding during start up $\Delta\dot{\gamma}_m/\bar{\dot{\gamma}}$ averaged over 50 start-up curves a) for varying age, t_w, at fixed average applied shear rate $\bar{\dot{\gamma}}$. b) varying shear-rate $\bar{\dot{\gamma}}$, at fixed sample age t_w. Error bars depict standard deviation of calculated values.

4.4.3 Comparison to Fluidity model

For Protocol I in this chapter we observe several interesting behaviours during start-up. M* and $\Delta\dot{\gamma}_m/\bar{\dot{\gamma}}$ are shown to be non-monotonically dependent on the applied average shear-rate $\bar{\dot{\gamma}}$. We also see that brittle yielding occurs some while after the peak of the overshoot, rather than as soon as yielding begins. In order to further examine this behaviour, and its dependence on sample age and shear-rate, we now turn to a simplified fluidity model. These results were obtained by Mr James Cochran [164], using the model we will now describe.

The elastoplastic stress evolves according to the Maxwell type constitutive equation

$$\partial_t \sigma_{xy} = G\dot{\gamma} - \frac{\sigma_{xy}}{\tau}, \tag{4.8}$$

where G is a constant elastic modulus and τ is a stress relaxation time, which evolves according to the dynamical equation

$$\partial_t \tau = 1 - \frac{|\dot{\gamma}|\tau}{\lambda + |\dot{\gamma}|\tau_0} + \frac{l_0^2}{\tau_0}\partial_y^2 \tau. \tag{4.9}$$

Here τ_0 is the fundamental relaxation time of the model. The constitutive curve $\Sigma(\dot{\gamma})$ of the model follows that of a Bingham fluid with yield stress $G\lambda$ and slope $G\tau_0$. For the purposes of this study, we set the parameters $G = 1$, $\tau_0 = 1$ and $\lambda = 1$. λ is a dimensionless parameter which sets the fluid yield stress and the rate of fludisation of the material in response to applied shear. For $\lambda = 0$, the material does not display a yield stress and will not age. We may therefore consider the effects of λ to be somewhat analogous to the effective noise temperature in the SGR model.

In absence of applied shear Eq. 4.9 reduces to $\partial_t \tau = 1$ meaning that the relaxation time τ grows linearly with the waiting time t_w. As in the SGR model, the value for this waiting time determines the transient response of a sample to applied strain. The diffusive term on the right-most side of Eq. 4.9 prevents the formation of unphysical heterogeneities on the lengthscale of the numerical grid, similar to the diffuse coupling implemented for SGR. The diffusion length l_0 sets the interface width between bands and is set $l_0 = 10^{-3}$ throughout this study.

The geometry in which we implement this model is a one-dimensional cell of size $L_y = 1$ in the flow gradient direction $\hat{\mathbf{y}}$. As in the calculations performed elsewhere in this chapter, the fluid is considered to only move along the $\hat{\mathbf{x}}$ direction. The shear-rate varies only along the $\hat{\mathbf{y}}$ direction. A finite difference method using $N_y = 3000$ lattice elements is used to approximate the spatial variation of the shear-stress and relaxation time in the cell. Each lattice site has a corresponding value $\sigma_{xy}(y)$ and $\tau(y)$, where $y = L_y \frac{j}{N_y}$. The shear-rate on each lattice site within the cell is calculated via the same method as in the SGR model, with solvent viscosity $\eta = 0.05$.

To seed the formation of the bands in this model, noise is added continuously as $\sigma_{xy}(y, t + \Delta t) = \sigma_{xy}(y, t) + r\delta\sqrt{\Delta t}\cos(\pi y/L_y)$. Δt is the time-step used to evolve the stress and relaxation time, and r is a random number taken from a uniform distribution between $-\frac{1}{2}$ and $+\frac{1}{2}$.

The relative simplicity of this model means that it is much less numerically expensive than SGR. Despite this simplicity, we see that the model exhibits many of the same behaviours seen for Protocol I in SGR. The smaller numerical cost of these calculations also means that we can explore a much larger parameter space, as we now discuss.

Start-up curves for aged samples in this model display a similar behaviour as in SGR. Example shear start-up curves are plotted in Figure 4.8 a) for both

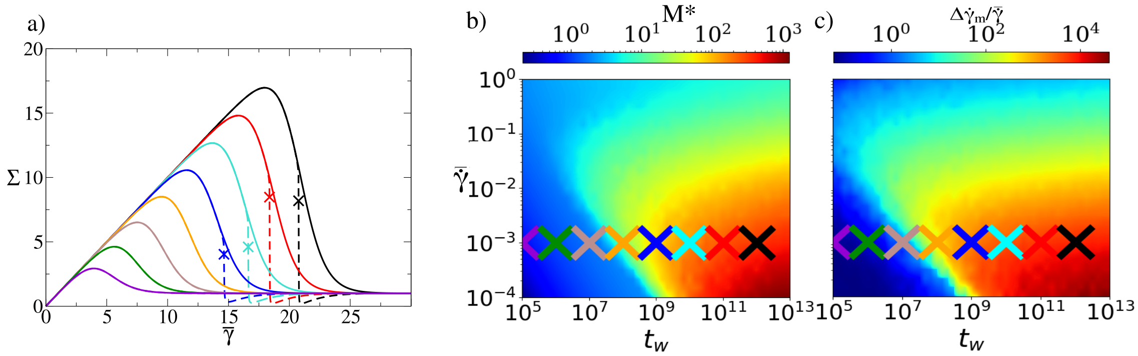

Figure 4.8: a) Start-up curves for homogenous (solid lines) and heterogeneous (broken lines) of the fluidity model showing increase in the height of the stress as a function of waiting time (curves left to right) $t_w = 10^5, 10^6, 10^7, ..., 10^{12}$. Colourmap of the b) maximum negative slope and c) maximum degree of banding. The crosses marked in these maps correspond to the start-up curves shown in a), with sample age increasing from left to right. Diffusion lengthscale $l_0 = 10^{-3}$, timestep $\Delta t = 0.01$, $N_y = 3000$.

homogeneous and heterogeneous flow. As is the case for SGR, increasing sample age leads to increasing overshoot height. For the plotted shear-rate, start-up curves break off from one another for $t_w > 10^8$, but overlap for younger systems. This mirrors the behaviour seen for the SGR model in Figure 4.4 a) . In both of these models, where the heterogeneous start-up curve breaks off from its homogeneous counterpart, it does so after the overshoot peak.

Colour-maps of the maximum negative slope M* and normalised maximum degree of banding $\Delta\dot{\gamma}_m/\bar{\dot{\gamma}}$ as a function of shear-rate and ageing time are shown in Figure 4.8 b) and c) respectively. Firstly, we note that both these quantities appear to be highly correlated, as we see in the results of the SGR data. This further affirms our hypothesis that the severity of yielding is related to the emergence of shear-bands in the sample. The trends observed for M* and $\dot{\gamma}_m/\bar{\dot{\gamma}}$ in this model are very similar to those for Protocol I in SGR. Both of these quantities increase with t_w for all values of $\bar{\dot{\gamma}}$, but vary non-monotonically with shear-rate at low values of t_w

In both of these models, non-monotonic dependence is possibly related to the competition between dynamics that result from ageing and those due to deformation. We may understand this by considering Eq. 4.9 in the limit in which $\dot{\gamma} \to 0$. As $\dot{\gamma}$ becomes small, so too do the right-most terms. This causes the ageing term to dominate. As a result, any variation in the relaxation time $\tau(y)$ within the system due to small heterogeneities in the flow remains small. When no shear bands develop, the heterogeneous and homogeneous start-up curves follow each other. The yielding process is therefore smooth. A mechanism similar to this may be at work in the SGR model, whereby the rejuvenation of elements at some timescale set by the finite noise-temperature prevents rapid fluidisation. We see from here forward that this does not occur in athermal systems.

4.5 Protocol II

In this protocol, the system is first equilibriated at a temperature $T_{\text{init}} > T_g$. Subsquently, the system is cooled at a constant rate α such that $\dot{T} = -\alpha$. At $T = 0$, the system is subjected to an average shear-rate $\bar{\dot{\gamma}}$. This method of annealing a sample was performed previously in simulations of Leonard-Jones glasses [29,32]. In this study we set $T_{\text{init}} = 5$ for all calculations performed with this protocol. To this author's knowledge, there exists no prior example of such a protocol being applied in a mesoscocopic model. The energy well distribution for different cooling rates is shown in Figure 4.9. At the highest cooling rate, the Boltzmann distribution of the initial temperature is well preserved. As the cooling rate is decreased, the distribution narrows and the average well depth increases. Ref. [30] shows similar distributions of activation energies for particle simulations. We now investigate if these similarities apply to the transient dynamics, when the sample is subjected to shear start-up.

4.5.1 Stress Response

The stress evolution after cooling is shown as a function of applied average strain in Figure 4.10. As in the previous protocol, we plot the start-up curves with homogeneity imposed and heterogeneity allowed. Overshoot heights increase for both homogeneous and heterogeneous start-up curves with decreasing cooling rate α.

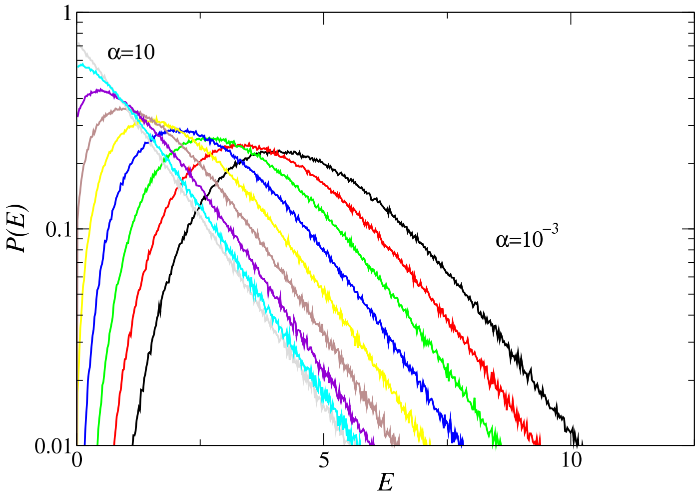

Figure 4.9: Distributions of energy well depths for the athermal SGR model for a system cooled from $T_{\rm init} = 5$. The distributions move towards deeper and deeper wells with decreasing cooling rate, with $\alpha = \{10, 3.162, 1, 0.3162, 0.1, 0.03162, 0.01, 0.003162, 0.001\}$. The histogram is composed from sampling from a grid of $N = 1.6 \times 10^6$ elements.

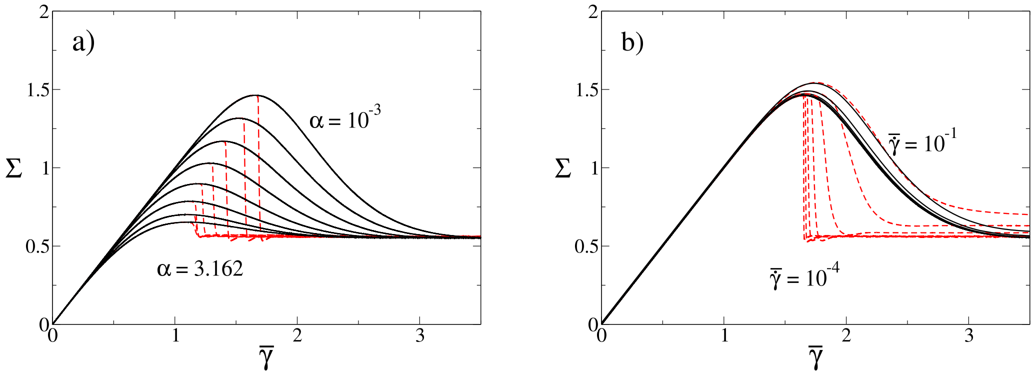

Figure 4.10: Start-up curves with imposed homogeneity (solid lines) and allowed heterogeneity (broken lines) for a) fixed shear-rate $\bar{\dot{\gamma}} = 0.001$ for a range of cooling rates $\alpha = \{10^{0.5}, 10^{0}, 10^{-0.5}, ..., 10^{-3}\}$. Increasing overshoots observed for start-up curves. b) at fixed $\alpha = 10^{-3}$ for varying applied shear-rate $\bar{\dot{\gamma}} = \{10^{-1}, 10^{-1.5}, 10^{-2}, ..., 10^{-4}\}$. Homogeneous curves converge to a shear-rate independent homogeneous curve while heterogeneous drop off becomes increasingly precipitous with decreasing shear-rate.

Near the apex of the overshoot, all the start-up curves of flows which permit heterogeneity cease to follow the homogeneous curves. We do not see the heterogeneous and homogeneous start-up curves overlay each other for small overshoots as was the case in Figure 4.4 a). Yielding in a heterogeneous flow for this protocol therefore appears to be always more brittle than for its homogeneous counterpart.

In Figure 4.10 b), we see another distinct difference from the previous protocol. The curves of shear-stress during start-up with homogeneity enforced vary only a small amount with $\bar{\dot{\gamma}}$. As the shear-rate decreases, the start-up curve becomes independent of the applied shear-rate. For the previous protocol, Figure 4.4 b) demonstrates the start-up curves to have a much greater dependence on applied shear-rate $\bar{\dot{\gamma}}$, even at low applied shear-rates.

With decreasing shear-rate $\bar{\dot{\gamma}}$, the yielding becomes more severe. For the largest plotted shear-rate $\bar{\dot{\gamma}} = 0.1$, the yielding is ductile and start-up curves for homogeneous and heterogeneous flow follow each other closely. As $\dot{\gamma} \rightarrow 0$, the heterogeneous yielding is increasingly brittle and we see the break off point converge near the apex of the homogeneous start-up curve.

Our calculated values of M^* in this protocol are plotted in Figure 4.10. For decreasing α in Figure 4.11 a), the value of M^* increases. This finding is consistent with start-up curves in Refs. [29, 32]. Samples cooled more gradually are better annealed, as with longer aged samples in the previous protocol.

We see M^* grow as a function of decreasing applied shear-rate in Figure 4.11 b). Fitting this to a power law produces a best fit $\mathrm{M}^* \; \bar{\dot{\gamma}}^{-0.9}$. This suggests that the slope may continue to increase indefinitely as a function of decreasing shear-rate. This is in contrast to the behaviour seen in Protocol I. In the thermal case, the value of M^* varies non-monotonically with decreasing shear-rate. We speculate that in the limit of $\bar{\dot{\gamma}} \rightarrow 0$, the system may exhibit discontinuous yielding, as observed in simulations performed using AQS in Refs. [22, 24, 145, 165].

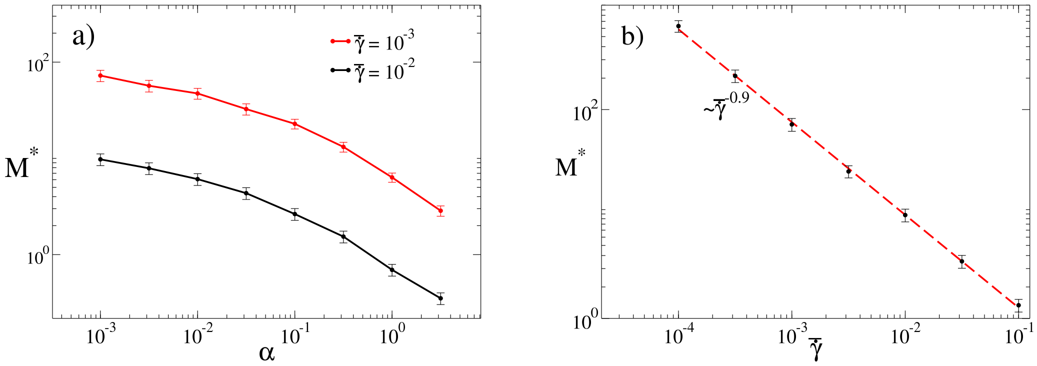

Figure 4.11: The maximum negative slope averaged over 50 start-up curves for a) fixed average shear-rate $\bar{\dot{\gamma}}$ and varying cooling rate α. b) fixed cooling rate $\alpha = 0.001$ and varying average shear-rate $\bar{\dot{\gamma}}$. Data shown in symbols (●), with line of best fit $\mathrm{M}^* \sim \bar{\dot{\gamma}}^{-0.9}$ (broken line). Error bars depict standard deviation of calculated values.

4.5.2 Flow Heterogeneity

The evolution of the degree of banding $\Delta\dot{\gamma}$ as a function of strain is shown in Figure 4.12 for the parameters which we discussed in the previous section. In Figure 4.12 a), this is plotted for different cooling rates. The maximum degree of banding increases with decreasing cooling rate. We do not see the same effect in the variation with shear-rate in Figure 4.12 b), noting that the maximum degree of banding is seen to be invariant with shear-rate. The onset of banding occurs sooner, similar to the yielding observed in Figure 4.10 b).

The maximum normalised degree of banding calculated during start-up is shown in Figure 4.13 for a) varying cooling rate and b) varying shear-rate. Once again we see that the variation of the degree of banding follows a similar trend to that of the calculated maximum negative slopes M*. The maximum normalised degree of banding varies with shear-rate as a power law, with an exponent very close to -1. This trend demonstrates the maximum value of the degree of banding within the sample to be invariant with the applied average shear-rate, as we saw in Figure 4.10 b).

It is worth noting how these results differ from those seen in the thermal Protocol I. Although we observe the same general behaviour, such as an increase in the degree of banding with annealing, some differences are apparent. The degree

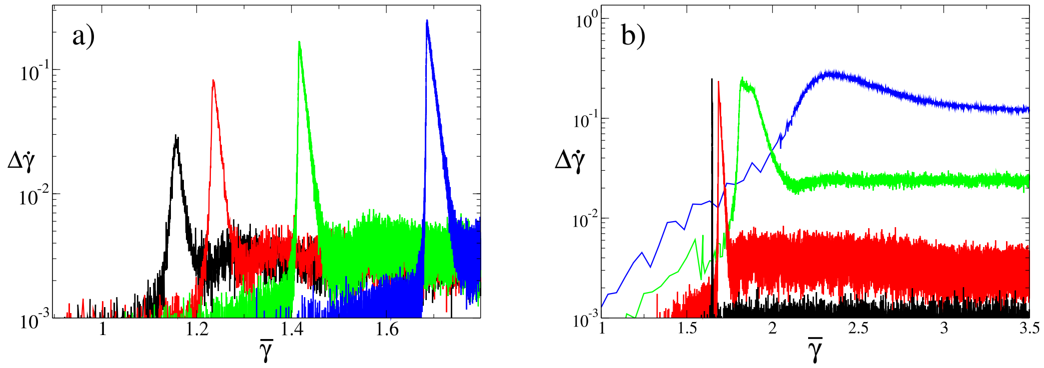

Figure 4.12: The unnormalised degree of banding as a function strain for a) a fixed average strain-rate $\bar{\dot{\gamma}} = 0.001$ and cooling rates $\alpha = \{1, 0.1, 0.01, 0.001\}$ and b) a fixed cooling rate $\alpha = 0.001$ and varying average shear-rates $\bar{\dot{\gamma}} = \{10^{-4}, 10^{-3}, 10^{-2}, 10^{-1}\}$.

of banding is invariant with shear-rate, leading to the normalised degree of banding being inversely proportional to the applied shear-rate. A similar trend is observed in the corresponding value of M*. We may infer from this that both the yielding and banding behaviour are dependent on the homogeneous start-up curves, which are also invariant with shear-rate as $\dot{\gamma} \to 0$.

An aspect of this protocol which is not seen in the previous case is the behaviour for less well annealed samples. In the protocol with non-zero noise temperature, the heterogeneous start-up curves for small overshoots follow the homogeneous curves almost exactly. In this case, we see that even for small overshoots, the curves for the heterogeneous flow break off from their homogeneous counterparts. We now see this same behaviour in our next protocol.

4.6 Protocol III

In this protocol, the system is initialised at some temperature $T_{\text{init}} > T_{\text{g}}$ and allowed to reach equilibrium. Following this, the system is instantaneously quenched to $T = 0$ and a fixed average shear-rate is then applied. This protocol may be considered as the limit of the previous cooling protocol with $\alpha = \infty$. This protocol was used previously in the simulations of Berthier and collaborators to examine yielding in

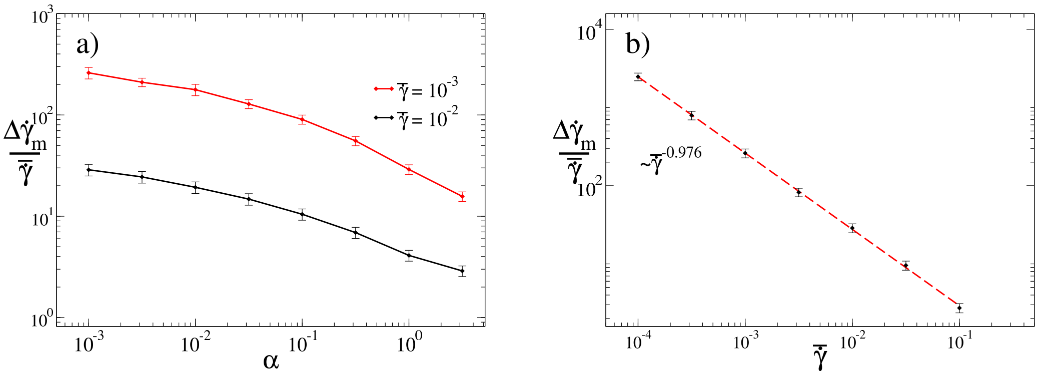

Figure 4.13: The maximum normalised degree of banding during start-up $\Delta\dot{\gamma}_m/\bar{\dot{\gamma}}$ averaged over 50 start-up curves for a) varying cooling rate α for fixed average shear-rates $\bar{\dot{\gamma}}$. and b) varying average shear-rate $\bar{\dot{\gamma}}$ for fixed cooling rate $\alpha = 0.001$. Data shown as symbols (◆) with line of best fit $\frac{\Delta\dot{\gamma}_m}{\bar{\dot{\gamma}}} \sim \bar{\dot{\gamma}}^{-0.976}$ (broken line). Error bars depict standard deviation of calculated values.

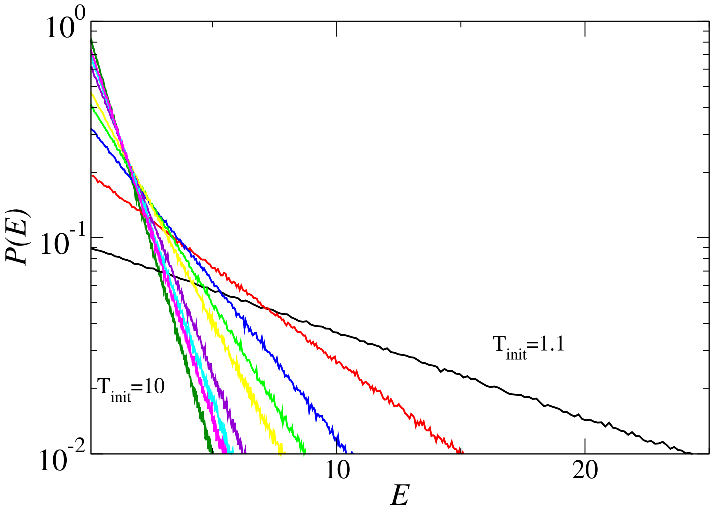

Figure 4.14: Distributions of energy well depths for samples equilibrated $T_{\text{init}} = \{10, 5, 4, 3, 2, 1.75, 1.5, 1.25, 1.1\}$, the distributions increase in steepness with decreasing T_{init}. The histogram is composed from sampling from a grid of $N = 1.6 \times 10^6$.

disordered systems [22,24,165]. Our findings agree qualitatively with these previous studies. The distributions shown in Figure 4.14 are described by the equation

$$P(E) = \frac{1}{1 - \frac{1}{T_{\text{init}}}} \exp\left[-E\left(1 - \frac{1}{T_{\text{init}}}\right)\right]. \tag{4.10}$$

Unlike both the thermal ageing protocol and the cooling protocol, the distribution of energy wells decreases monotonically over the full range of values of E. Despite these distributions appearing very different from those in the previous protocols, we observe similar behaviour during shear start-up to that seen in Protocol II.

4.6.1 Stress Response

The stress-strain curves for a range of initial temperatures at fixed shear rate are shown in Figure 4.15 a). We see increasing overshoot height with decreasing initial temperature T_{init}, in line with the findings of Ref. [22]. As in the previous protocol, the onset of yielding occurs near the apex of the overshoot. We observe the start-up curve for the heterogeneous flow break off from its homogeneous counterpart even for small overshoot heights. Likewise, we see similar behaviour with decreasing shear-rate at fixed $T_{\text{init}} = 1.1$ in Figure 4.15 b), as we see in Protocol II. The homogeneous start-up curves converge and the heterogeneous yielding becomes more brittle. This response was also observed for Protocol II in this chapter, despite the system having very different initial energy well distributions. This strongly suggests that the effect is connected with the samples being sheared at zero effective noise temperature.

In Figure 4.16, the average maximum negative slope of stress against strain M^* for varying T_{init} and $\overline{\dot{\gamma}}$ is shown. We find that with decreasing initial temperature, we see increasing maximum negative slope. This behaviour is in accordance with particle based simulations performed in Ref. [24]. As seen in the cooling protocol (Protocol II), the curves of lower and higher shear-rates resemble each other, with M^* being lower for all values of T_{init} at the higher shear-rate. The maximum negative slope M^* once again varies as a power law function of the shear-rate, with exponent close to -1. This is similar to that seen in the previous protocol.

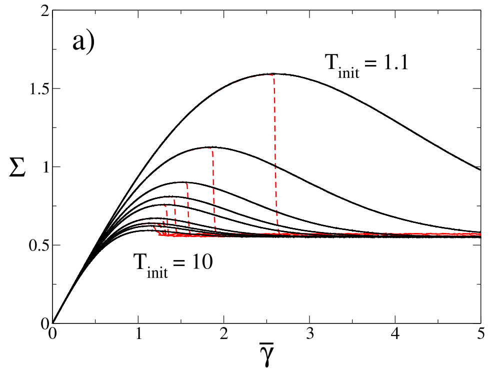

Figure 4.15: Homogeneous (solid lines) and heterogeneous (broken lines) shear start-up curves for a) fixed average shear-rate $\bar{\dot{\gamma}} = 0.001$ and for initial temperatures $T_{\text{init}} = \{1.1, 1.25, 1.5, 1.75, 2, 3, 4, 5, 6, 7, 8, 9, 10\}$, with overshoot height increasing with decreasing initial temperature. b) fixed $T_{\text{init}} = 1.1$ and varying applied shear rate $\bar{\dot{\gamma}} = \{10^{-1}, 10^{-1.5}, 10^{-2}, ..., 10^{-4}\}$. Homogeneous curves converge to a shear-rate independent homogeneous curve while heterogeneous drop off becomes increasingly precipitous with decreasing shear-rate.

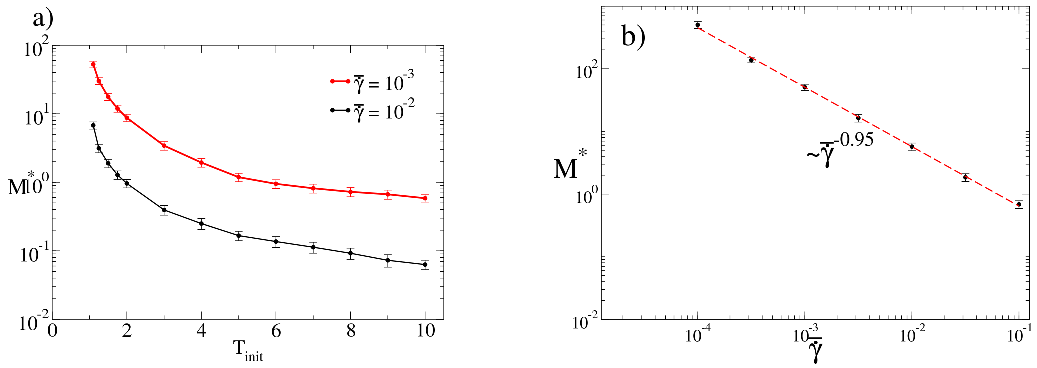

Figure 4.16: The maximum negative slope M* averaged over 50 start-up curves a) for fixed average shear-rate and varying initial temperature and b) for varying shear-rate for fixed initial temperature $T_{\text{init}} = 1.1$. Data shown in symbols (●) with line of best fit $\text{M}^* \sim \bar{\dot{\gamma}}^{-0.95}$ (broken line). Error bars depict standard deviation of calculated values.

4.6.2 Flow Heterogeneity

The unnormalised degree of banding as a function of strain is shown in Figure 4.17 a) for several T_{init} at fixed shear-rate $\bar{\dot{\gamma}}$ and b) for several values of $\bar{\dot{\gamma}}$ for fixed initial

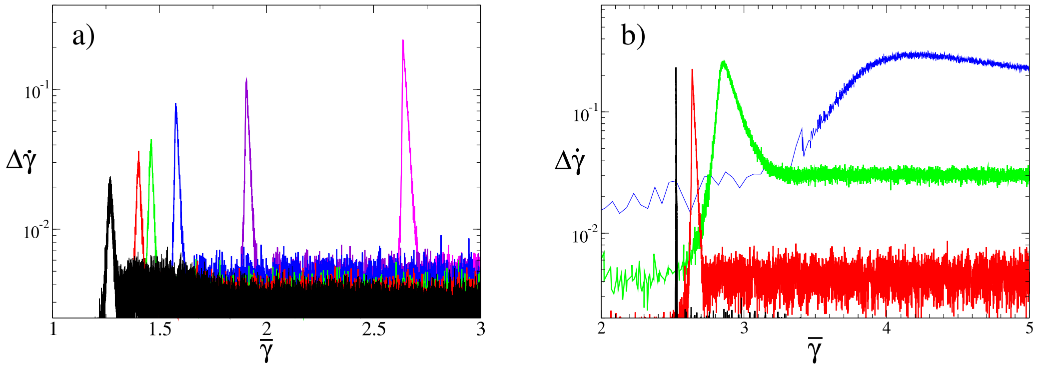

Figure 4.17: The unnormalised degree of banding as a function strain for a) a fixed average strain-rate $\bar{\dot{\gamma}} = 0.001$ and $T_{\text{init}} = \{3, 2, 1.75, 1.5, 1.25, 1.1\}$ and b) a fixed initial temperature $T_{\text{init}} = 1.1$ and varying average shear-rates $\bar{\dot{\gamma}} = \{10^{-4}, 10^{-3}, 10^{-2}, 10^{-1}\}$.

temperature T_{init}. We see an increasing maximum degree of banding with decreasing initial temperature in Figure 4.17 a). As seen in the previous protocols, this is correlated to increasing overshoot height. The unnormalised degree of banding, however, once again varies minimally with shear-rate in Figure 4.17 b). The width of this peak banding becomes narrower with the decreasing applied shear-rate.

The normalised degree of banding $\Delta\dot{\gamma}_m/\bar{\dot{\gamma}}$ for varying initial temperature and shear-rate is plotted in Figure 4.18. The normalised degree of banding is shown to increase as function of decreasing initial temperature at fixed applied average shear-rate $\bar{\dot{\gamma}}$. As in all protocols studied here, it varies in a similar manner to the corresponding severity of yielding M*. We once again see that the variation in the normalised degree of banding with respect to $\bar{\dot{\gamma}}$ obeys a power law with exponent very close to -1. This behaviour is consistent with that seen in Protocol II, in which we also subjected the sample to shear at zero effective noise temperature.

This protocol shows many similarities with Protocol II. When we compare Figures 4.10 b) and 4.15 b), we see that in both protocols the start-up curves follow a similar trend with decreasing shear-rate. This trend mirrors that seen in simulations of shear start-up in athermal soft glasses in Ref. [24] for decreasing shear-rates. The SGR model in the athermal limit is therefore demonstrated here to be effective at modelling the behaviour seen in simulations of athermal amorphous materials.

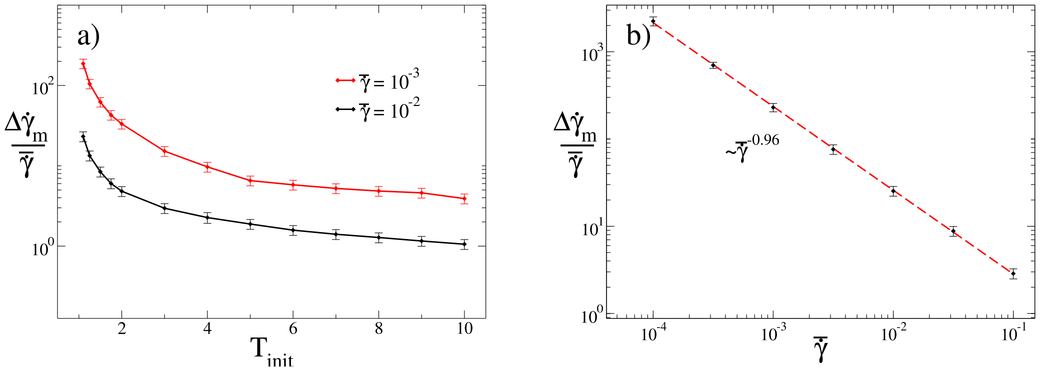

Figure 4.18: The maximum normalised degree of banding during start-up $\Delta\dot{\gamma}_m/\bar{\dot{\gamma}}$ averaged over 50 start-up curves for a) varying initial temperature T_{init} for fixed applied average shear-rate and b) varying shear-rate for fixed initial temperature $T_{\text{init}} = 1.1$. Data shown in symbols (♦) with line of best fit $\frac{\Delta\dot{\gamma}_m}{\bar{\dot{\gamma}}} \sim \bar{\dot{\gamma}}^{-0.96}$ (broken line). Error bars depict standard deviation of calculated values.

4.7 Conclusions and Future Work

In this chapter, we have studied the process of yielding in yield stress fluids subject to three different protocols for sample preparation. Following preparation, the system was subjected to a fixed average shear-rate $\bar{\dot{\gamma}}$. In the case of two of the protocols studied, shear was applied at zero effective noise temperature. We compared the results obtained for the non-zero temperature protocol to those of a simplified fluidity model which describes an age dependent yield stress fluid. While in all cases our results establish a clear relationship between the onset of yielding during shear start-up and the formation of heterogeneous flow, we observe distinct differences in behaviour between thermal and athermal systems during start-up.

In Protocol I, in both the fluidity and SGR models, we observe that longer ageing times lead to more brittle yielding, as characterised by the maximum negative slope of the start-up curve M^*. We also observe that yielding becomes more brittle with decreasing shear-rate for sufficiently large overshoots. In both models, the homogeneous flow is stable for sufficiently small overshoots. For stable flows, the heterogeneous start-up curves match those for homogeneous start-up.

We also observe that for shorter ageing times in the SGR model, as shown in Figure 4.5 b), the severity of yielding varies non-monotonically with shear-rate.

A similar behaviour is observed in the fluidity model, as shown in the colourplots in Figure 4.8 b). In both models, this trend is also exhibited in the degree of banding. Since the overshoot in both models for this protocol is determined by the product $\bar{\dot{\gamma}} t_w$, we may conclude that this is due to the overshoot height becoming too small for the flow to be unstable, hence both brittle yielding and banding diminish.

We do not observe such behaviour in the other protocols studied. Both Protocols II and III subject the systems to shear at zero effective noise temperature. In Protocol II, annealing is performed by cooling the systems at various rates prior to start-up. In Protocol III, the system is equilibrated to a fixed initial temperature before being quenched to $T = 0$ prior to shear. For better annealed samples, we see an increase in overshoot height, as was seen in Protocol I for longer ageing times. These results replicates those seen in particle simulations for both the cooling [29,32] and quenching [22,24] methods of preparation. To the knowledge of the author, this is the first time calculations performed using a mesoscopic model have replicated the results of these simulations. In these calculations, wherein samples are sheared at $T = 0$, we observe a break-off even at small overshoots, unlike the results seen in Refs. [22,23]. In the particle simulations of Refs. [22,23], small overshoots are seen for less well annealed samples. Where this is the case, ductile yielding is observed, even in the limit $\bar{\dot{\gamma}} \to 0$. This disparity between our findings and simulation may be attributable to finite size effects which are not accounted for in our model.

For variation in shear-rate, we see another departure from the behaviour seen in Protocol I. Where the flow is constrained to be homogeneous, the corresponding start-up curves converge with $\bar{\dot{\gamma}} \to 0$, such that they are independent of the applied shear-rate. When heterogeneous flow is allowed, the observed yielding becomes more brittle with decreasing shear-rate. This replicates simulations performed at finite shear-rates in Ref. [24], wherein simulations showed increasingly precipitous yielding as $\bar{\dot{\gamma}} \to 0$. At $\bar{\dot{\gamma}} = 0$, these simulations showed such yielding to be discontinuous. Our results in this chapter suggest that for athermal systems, we will observe the same effect. Results in both protocols show the values of M^* to follow an almost inverse dependence on the applied shear-rate as shown in Figures 4.11 b) and 4.16 b). This demonstrates that the rate of yielding with respect to time $d\Sigma/dt$ is independent of applied shear-rate.

When we examine the degree of banding in Protocols II and III, we again observe behaviours distinct from those seen in Protocol I. The absolute degree of banding is independent of applied shear-rate for a fixed value of α or T_{init}. As a result, the normalised degree of banding is inversely dependent on the applied shear rate. In Protocol I, we see the degree of banding decrease at very small shear-rates as the overshoot becomes too small to allow banding. In Protocols II and III, the invariance of both the degree of banding and the homogeneous start-up curves may indicate that these quantities are linked i.e. that the maximum degree of banding is set solely by the homogeneous start-up curve.

The motivation for this study was to examine yielding in amorphous materials during shear start-up and to gain insight into how this is linked to the formation of transient shear-bands. We have conclusively shown across all protocols studied, for both thermal and athermal systems, that the yielding is correlated to the formation of transient heterogeneous flow. In all cases in athermal systems, and in thermal systems where the height of the overshoot remains large enough to permit banding, the severity of yielding, as defined by M^*, increases with decreasing applied shear-rate.

In the case of athermal systems, the severity of yielding consistently increases with decreasing shear-rate. This suggests that should these calculations be performed at $\bar{\dot{\gamma}} = 0$, we may also observe the discontinuous yielding seen in Refs. [22, 24]. In Refs. [22, 23], this behaviour is attributed to a reversal in the direction of the start-up curve for homogeneous flow as depicted in Figure 4.1 a). For all calculations performed here, we find that the theoretical homogeneous start-up curves retain the form shown in Figure 4.1 b). We therefore suggest that the discontinuous yielding observed in simulation is the result of heterogeneous flow developing over some fixed timescale, rather than the spinodal phase transition mechanism proposed. Future simulations which measure the degree of heterogeneity as well as the overall shear-stress may substantiate the findings in this chapter.

Despite differences between the protocols, in all cases we see that better annealed samples display more brittle yielding. This is observed for thermal and athermal protocols. In order to understand this, we consider first the behaviour of the system prior to the formation of shear-bands. For increasingly well annealed samples, more elements are in deeper energy wells. We see this in Figures 4.3, 4.9 and 4.14. This naturally leads to larger overshoots due to a larger strain being required to induce yielding on elements. When the sample begins to yield heterogeneously, force balance requires that the fluidised region develops a larger shear-rate. If the average stress on the system is large, as in the case of the well annealed samples, this local shear-rate must likewise be large such that the Newtonian stress in the yielded region is equal to the elastoplastic stress in other regions. This increase in shear-rate leads to elements on this streamline yielding more rapidly, and in turn the shear-rate along that streamline increases further. In order to maintain a constant average shear-rate, the local shear-rate on all other regions decreases and may become negative [12]. This then causes the average stress to decrease rapidly and brittle yielding is observed. We can therefore infer from this process why the large shear-stress overshoot observed for well annealed samples leads to brittle yielding in all protocols.

While the findings of this study offer strong evidence to explain the behaviours observed in simulations, there remain questions which are unanswered, as well as new ones presented by this work. Simulations performed in Ref. [22] show that for samples sheared at $\overline{\dot{\gamma}} = 0$ and equilibrated at moderate T_{init}, a small overshoot without discontinuous yielding is observed. Our findings in this chapter suggest that given even a small overshoot, discontinuous yielding will be observed in the limit of zero shear-rate for athermal materials. We speculate that this is due to finite size effects unaccounted for in our model. This is substantiated by findings in Ref. [24], which demonstrate more dramatic yielding at $\overline{\dot{\gamma}} = 0$ for increasing system size.

Further questions which merit future study that have emerged from this work are the dissimilarities between the processes of shear start-up and yielding in thermal systems (Protocol I) as opposed to athermal (Protocol II and III). Even at low shear-rates, yielding does not occur at the apex of the homogeneous start-up curve, but after a small drop in shear-stress. Further study is required to examine how this behaviour varies with effective noise temperature.

Finally, it should be noted that while all calculations performed in this study have been at finite shear-rates, we frequently attempt to extrapolate our findings to the limit $\bar{\dot{\gamma}} \to 0$. We compare our results to simulations performed in this limit and substantiate our reasons for doing so. For scientific completeness however, such mesoscopic calculations should be performed in this limit to verify the findings of this work and hopefully grant further insights into the interplay between transient shear-banding and yielding during applied shear deformation.

4.8 Appendix I : Numerical Methods

For all protocols described in this chapter, we calculate both the homogeneous and heterogeneous start-up curves. We first outline in this appendix the method by which the system is evolved homogeneously before discussing additional methods used to study heterogeneous flow.

In the SGR model, the evolution of the material is studied by considering an ensemble of elements, each having a specified energy well depth E and microscopic strain $l = \sqrt{(\mathbf{W}-\mathbf{I}):(\mathbf{W}-\mathbf{I})}$. A fixed shear-rate $\bar{\dot{\gamma}}$ is applied to all elements and the strain on each element at a given time-step n incremented such that

$$\mathbf{W}_{n+1/2}(t) = \mathbf{W}_n(t) + 2\Delta t \mathbf{D}_n(t)\,. \tag{4.11}$$

Here Δt is the Euler time-step and $\mathbf{D} = \frac{1}{2}(\nabla \mathbf{v} + \nabla \mathbf{v}^T)$ is the symmetric part of the rate of strain tensor. In a system with uniform shear-rate, this becomes

$$\mathbf{D} = \frac{1}{2}\begin{pmatrix} 0 & \bar{\dot{\gamma}} \\ \bar{\dot{\gamma}} & 0 \end{pmatrix}. \tag{4.12}$$

The conformation tensor for the next stage of the update is given by $\mathbf{W}_{n+\frac{1}{2}}(i,j)$. The update in Eq. 5.5 is performed over all elements on the lattice. Following this, the hopping rate $\Gamma(i,j)$ is calculated for each element according to equation

$$\Gamma(i,j) = \Gamma_0 \mathrm{min}\{\exp[-(E(i,j) - \frac{G}{2} l(i,j)^2)/T], 1\}. \tag{4.13}$$

where $l(i,j) = \sqrt{\mathbf{W}_{n+1/2}(i,j) - \mathbf{I}) : (\mathbf{W}_{n+1/2}(i,j) - \mathbf{I})}$ The test for yielding is then performed via selecting a random number r from a uniform distribution in the range $(0,1)$. The criterion is applied such that the element yields if $r < \Gamma(i,j)\Delta t$. The microscopic conformation tensor is then reset $\mathbf{W}_{n+1}(i,j,t+\Delta t) = \mathbf{I}$. If the element does not yield $\mathbf{W}_{n+1}(i,j,t+\Delta t) = \mathbf{W}_{n+\frac{1}{2}}(i,j)$.

To study the stress evolution with heterogeneity permitted we simulate a one-dimensional flow field of N coupled streamlines. The shear-rate on each streamline $\dot{\gamma}$ is no longer fixed, but varies with time. Each streamline corresponds to an ensemble of M SGR elements, with shear-rate fixed along each streamline. A fixed average shear-rate is applied to the system and force balance preserved via coupling each streamline to the 1D Stokes equation such that

$$\nabla \cdot \mathbf{\Sigma} = \partial_y(\eta\dot{\gamma} + \sigma_{xy}) = 0. \tag{4.14}$$

The total stress is therefore uniform for each streamline. In order to apply an average shear-rate $\bar{\dot{\gamma}}$ to the system, we calculate the average total stress

$$\Sigma = \eta\bar{\dot{\gamma}} + \bar{\sigma}_{xy}, \tag{4.15}$$

where Σ is the average stress over all elements in the system. Force balance necessitates that the stress on each streamline be equal, and we impose an average Newtonian stress $\eta\bar{\dot{\gamma}}$. Therefore the shear-rate on each streamline is calculated via the relation

$$\dot{\gamma}\left(j\right) = \frac{1}{\eta}(\eta\bar{\dot{\gamma}} + \bar{\sigma}_{xy} - \sigma_{xy}\left(j\right)). \tag{4.16}$$

Here $\bar{\sigma}_{xy}$ is the average elastoplastic shear stress, with $\sigma_{xy}\left(j\right)$ corresponding to the average elastoplastic stress along a given streamline j . $\dot{\gamma}\left(j\right)$ is the shear-rate along a streamline j, and $\bar{\dot{\gamma}}$ is the applied average shear-rate. At each time-step, the average elastoplastic stress is calculated for each streamline as well as the overall average stress. The shear-rate upon each streamline is then preserved by varying the shear-rate $\dot{\gamma}\left(j\right)$ on each streamline.

The evolution of the homogeneous stress during start-up may be shown to be robust to a large range of timesteps. However, when undergoing heterogeneous dynamics, it is important to ensure that sufficiently small timesteps are used to resolve the dynamics of the flow. The timestep Δt is determined via an adaptive method which couples its value to the unnormalised degree of banding in the system $\frac{1}{M}\sqrt{\sum_{j=1}^{M}(\dot{\gamma}\left(j\right) - \bar{\dot{\gamma}})^2}$. The timestep is then varied in accordance with this heterogeneity. This ensures that during yielding, when heterogeneity is large, the dynamics are well resolved. Conversely, much faster calculation of the evolution of system is possible when homogeneity is retained.

In order to introduce a diffusive coupling between elements, as applied in previous studies of shear-banding, we impose the following protocol. If an element i along streamline j yields, the shear strain of three randomly chosen elements on each neighbouring streamline is adjusted by a factor $DW_{xy}\left(i, j\right)(-1, 2, -1)$, before the strain of $W_{xy}(i,j)$ is reset $W_{xy}(i,j) = 0$. This gives a spatial dependence of the heterogeneity in the system, previously shown to be important to avoid unphysical behaviour [161].

Chapter 5

Ultra-Long-Lived Transient Shear-Banding in Soft Glassy Materials

5.1 Introduction

In the previous chapter we established that the transition from solid to liquid like behaviour in an elastoviscoplastic fluid is closely associated with the manifestation of spatially heterogeneous shear-rates. Characterising both the onset and development of these heterogeneities remains a topical area of research. In this chapter, we study theoretically the longevity of shear-bands during shear start-up. A widely cited study of the longevity of shear-bands in a yield stress fluid was performed by Divoux et al. [27]. This study examined the evolution of shear-bands in a carbopol gel using velocimetry data to spatially resolve the flow profile in a Taylor-Couette cell. By tracking the interface between shear bands until a homogeneous shear-rate was recovered, they calculated the lifetime of shear-bands as a function of shear-rate. The time taken for the system to completely fluidise (i.e. the lifetime of the shear bands) τ_f was found to fit well to a power law $\bar{\dot{\gamma}}^{-\alpha}$ with exponent $\alpha = 2.3$.

A further study of band longevity was performed for stress controlled start-up [70]. This also demonstrated that the timescale for fluidisation followed a power law dependence $(\Sigma - \Sigma_y)^{-\beta}$, with power law exponent increasing with carbopol concentration from $\beta = 3.4 - 8$. In this paper, they suggest that sample preparation may also play a part in the these properties. They found that despite two samples having the same concentration, different exponents β were observed. This finding was attributed to variations in pH between the samples. The ratio of the exponents of fludisation time τ_f against applied shear-rate, α, and against shear-stress β was found to match the Herschel-Bulkley exponent of the fluid. This observation, it was suggested, may indicate a physical motivation for the Herschel-Bulkley model, usually considered phenomenological in nature. In an attractive colloidal gel, however, the fluidisation time τ_f was found to be exponentially dependent on the applied shear-stress [166, 167]. A free energy based continuum model was recently devised that effectively reproduces many of the results found in the experiments of Divoux and collaborators [168].

Chaudhuri et al. [169] performed simulations of an aged Yukawa fluid in order to study the longevity of shear-bands in a stress controlled shear-flow. Their study found the timescale for fludisation to also follow a power law $\tau_f \sim (\Sigma - \Sigma_y)^{-\beta}$, with exponent $\beta = 2.285$.

Simulations have also been used extensively to examine the emergence and persistence of shear-bands in soft glasses during shear start-up. These studies have made use of a number of different methods to prepare the sample prior to shear. In the case of Ref. [28, 33], the system of Leonard-Jones particles is equilibrated at a fixed temperature above the measured glass transition temperature. The system is then quenched below the glass transition and aged for a fixed waiting time t_w, before being subjected to shear at a fixed rate. The stress response was found to be dependent on both the applied shear-rate $\bar{\dot{\gamma}}$ and ageing time t_w. The spatial evolution of transient shear bands was examined by calculating the local mobility of particles in the sample. It was observed that the interface between the bands propagates as $t^{\frac{1}{2}}$. For a fixed sample age $t_w = 10^4$, the authors found that the fluidisation time τ_f, followed a power law such that $\tau_f \sim \bar{\dot{\gamma}}^{-1.28}$.

Simulations were also performed by Vasisht and DelGado, who studied the longevity of shear bands in an athermal Leonard-Jones glass at high packing fraction [29, 32]. In their simulations, the samples were prepared by first equilibritating the system at a high temperature before cooling to zero temperature. When measured as a function of shear-rate, the lifetime of shear bands was found to vary as a power law, as observed in the experiments of Divoux et al. [27]. The exponent of this power law was found to vary as a function of the cooling rate applied to the sample, with exponent of 1.11 for the highest cooling rate and 1.66 for the lowest. We perform a similar protocol in this study and compare our findings to those observed in simulation.

Simulations by Alix-Williams and Falk examined the formation and broadening of shear-bands in metallic glasses in two dimensions [34]. They performed particle simulations using a Leonard-Jones glass as well as using metallic glass potentials. In these simulations, the system is initially equilibrated before being cooled at different rates to a fixed non-zero temperature. The initial width of the shear-band within the cell was found to be dependent on the cooling rate applied. This study also compared the results found in simulation to those predicted by a Shear Transformation Zone (STZ) model which modelled the evolution of the bands as a pulled interface. Good agreement was found between this model and the simulations performed.

The STZ model has been used in several studies to examine how shear-bands develop during shear start-up. Studies by Manning and collaborators [170, 171] examined the emergence of shear-bands for different inital effective temperatures. In Ref. [170] they compared their results directly with particle simulations which were performed using a cooling protocol on samples of metallic glasses [172]. In order to emulate the effects of a cooling protocol, the initial effective temperature was selected for each calculation that best reproduced the start-up curves seen in simulation. Their calculations effectively captured aspects of the simulations, including a rate dependent localisation of shear-rate and an increasing overshoot height with decreasing cooling rate. They did not explore the longevity of these bands and examined only the early timescale behaviour of the material when subjected to shear. A study performed later by Hinkle and Falk [173] also used the STZ theory to qualitatively match the transient behaviour seen in the experiments of Ref. [27]. With some variation of the parameters of the model with the magnitude of the shear-rate, their study was quantitatively able to match the power law dependence of band longevity on applied shear-rate.

In all of these STZ studies the flow was confined to a 1D approximation, with effective temperature and shear-rate only varying in the cross channel direction. A two-dimensional simulation of strain localisation in metallic glasses was performed by Jagla [174] using a model first introduced in Ref. [175]. The study modelled the effects of ageing using a system of PDEs that simulate the relaxation of mesoscopic elements. This study observed that the height of the overshoot increased with sample age, and that shear bands formed during start-up when samples demonstrated sufficiently large stress overshoots. The width of these bands was found to grow as $t^{\frac{1}{2}}$, as was seen in the particle simulations performed in Ref. [28,33,34]. This model, which describes the material mesoscopically in terms of discrete elements is an example of an elastoplastic model, which are widely used to study elastoviscoplastic fluids, as we shall now discuss.

5.2 Elastoplastic Models

Elastoplastic models (EPMs) are widely used to study heterogeneous processes in amorphous materials. Thorough reviews of elastoplastic models and their widespread use may be found in Ref. [30, 31]. All elastoplastic models have a similar form and describe an amorphous material via a collection of elements. In general, evolution of the stress in these elements is captured by the following criteria [30]:

1. Each element behaves elastically before yielding.
2. A local yield criterion determines the onset of a plastic event for a given element.
3. The redistribution of the stress that is given during plastic yielding causes long range interactions among elements.
4. Each element recovers its elastic behaviour following a plastic event.

While these attributes apply generally to all elastoplastic models, including that used in this study, it is from each model's slight variations that different behaviour is observed. Differences between models chiefly relate to the selection of local yielding criteria and the manner in which the stress is redistributed following each yielding event.

A widely used class of lattice EPM was devised by Picard et al. [176]. They incorporate a yielding rate dependent on the stress of each element, Σ and critical stress Σ_c. The yielding rate of each element is modelled as $\Theta\left(\Sigma - \Sigma_c\right)$, where $\Theta\left(\xi\right)$ is the Heaviside step function. This yielding rate acts as the characteristic timescale of the system. Until each element has obtained this critical stress due to external loading, the yielding rate is 0, and the element imitates an elastic solid and gains stress in linear proportion to the applied strain. Once the stress exceeds Σ_c, the local yielding rate is 1. The element then has unit probability of yielding per unit time. Upon yielding, the anistropic stress redistribution is modelled using an Eschelby propagator [177]. This redistributes the stress according to the quadrapolar description derived originally by Eschelby for the failure of a single element in an elastic medium [178]. More recently, this formulation has been extended to a tensorial description of the stress [179], but showed little variation in overall behaviour. In this formulation, the stress is assumed to be redistributed instantaneously, but some models incorporate effects such as inertia which leads to a delayed redistribution of stress [180]. In the model we introduce in this chapter, the stress is redistributed via a background solvent viscosity, similar to the method used in other chapters in this thesis. We also incorporate a tensorial representation of the stress in our model. We demonstrate that this method also obtains the quadrupolar redistribution of stress after a single yielding event.

Much use of these models is made to study the avalanche dynamics caused by long range changes in the stress due to local plastic failure [181–186]. Associated with these avalanches are changes in the average shear-stress of the system, and many studies have linked them with macroscopic material yielding [187–192]. While this is a very active area of research, we do not explicitly explore these avalanche dynamics in this study and instead concentrate on modelling the other features of yielding. We specifically study the evolution of shear bands in an EPM [190, 193–195], the formation of which is examined in Chapter 4 of this thesis.

As in other complex fluids, the formation of permanent shear-bands is closely associated with a non-monotonic constitutive curve [23, 196–198]. In this study however, our model has a monotonic constitutive curve for all parameters studied and so permanent shear-bands do not form. Previous studies of transient heterogeneities under applied deformation using elastoplastic models [25, 199–201] have shown this to be related to the yielding criteria of the sample elements prior to shear. Moorcroft et al. [25] demonstrated that the formation of shear bands in the elastoplastic soft glassy rheology model was dependent on the sample age. They also found these shear-bands to be extremely long lived, sometimes persisting to thousands of strain units. They did not, however, characterise the longevity of these shear-bands in terms of sample age and applied shear-rate. In this study, we characterise the longevity of shear-bands by applying the soft glassy rheology model ageing dynamics to an elastoplastic lattice model.

5.3 Lattice Soft Glassy Rheology Model

In this study, we combine the ageing dynamics of the soft glassy rheology model with a two-dimensional lattice formulation. Previous studies have examined the effects of the varying initial distribution of critical stresses Σ_c [23,200,201] for mesoscopic elements prior to shear start up. They do so by explicitly varying the initial distribution of critical stresses directly. While these studies may offer insight into the underlying processes involved in yielding and transient shear banding, it is not necessarily clear how we can compare these results directly with simulation or experiment. Also of note is that previous studies which attempt to describe aged materials are all performed at the athermal limit and so do not account for the effects of non-zero temperature. Applying the ageing dynamics of SGR, we are able to directly compare our results with those of simulations, in particular those of Refs. [32, 33]. Our study emulates the ageing and cooling protocols used in these studies and so a proper comparison can be made.

In order to do this we define a lattice of $i = 1, ..., N_x$ and $j = 1, .., N_y$ elements. Each of these elements has an associated microscopic conformation tensor

$\mathbf{W}(i,j)$, rate of strain tensor $\nabla\mathbf{v}(i,j)$, an energy well $E(i,j)$ and a stress tensor $\sigma(i,j) = G(\mathbf{W}(i,j) - \mathbf{I})$. The soft glassy rheology dynamics are described in Chapter 4 so we shall not describe them in depth here. Recall that in an ensemble of SGR elements, each element has an associated hopping rate given by the expression

$$\Gamma(i,j) = \Gamma_0 \mathrm{min}\left\{1, \exp\left[-(E(i,j) - \frac{1}{2}Gl(i,j)^2)/T\right]\right\}. \tag{5.1}$$

Here Γ_0 is the microscopic hopping rate, T is the effective noise temperature. G the shear modulus and l is the generalised expression of strain as defined in [202, 203] for each element defined such that

$$l(i,j) = \sqrt{(\mathbf{W}(i,j) - \mathbf{I}) : (\mathbf{W}(i,j) - \mathbf{I})}. \tag{5.2}$$

The lattice of elements is projected onto a cell with dimensions L_x and L_y. The coordinates of each element (i,j) are then given by $\left(x = \frac{i}{N_x}L_x, y = \frac{j}{N_y}L_y\right)$. Each element is assumed elastic until it yields, such that the evolution of the stress between yielding events is given by the expression

$$\dot{\sigma}(x,y) = 2G\mathbf{D}(x,y). \tag{5.3}$$

Here $\mathbf{D}$ is the symmetric rate of strain tensor, $\frac{1}{2}(\nabla\mathbf{v} + \nabla\mathbf{v}^T)$. The evolution of the rate of strain tensor for each element is calculated via the Stokes equation

$$\nabla \cdot (2\eta\mathbf{D} + \sigma - p\mathbf{I}) = 0. \tag{5.4}$$

Here p is the hydrostatic pressure field which is determined by enforcing incompressibility $\nabla \cdot \mathbf{v} = 0$. The solvent viscosity η describes either a true solvent or modes much faster than those describing the elastoplastic stress σ. Each element therefore does not possess purely elastic stress, but also a viscous stress defined by the expression $2\eta\mathbf{D}$. The stress is redistributed between yielding events via the local rate of strain tensor. This introduces a timescale for the redistribution of the stress which is given by $\tau_\eta = \eta/G$. For all the applications of the model performed here $\eta \ll G/\Gamma_0$. The timescale for the redistribution of the stress is therefore much shorter than the rate of yielding. Therefore, for small values of η, the macroscopic behaviour is independent of the solvent viscosity η. The use of a background solvent is, as far as this author is aware, a novel method to preserve force balance in an Elastoplastic Lattice Model. We also implement Lees-Edwards periodic boundary conditions [204] in the system and incorporate affine advection using the method we shall now describe.

The deformation of each mesoscopic element is simulated by evolving each element individually as in Eq. 5.3. This is performed using Euler timestepping, which gives the expression

$$\mathbf{W}_{n+\frac{1}{2}}\left(i,j\right) = \mathbf{W}_{n}\left(i,j\right) + \Delta t 2\mathbf{D}_{n}\left(i,j\right). \tag{5.5}$$

Here $\mathbf{W}_{n}\left(i,j\right)$ is the microscopic conformation tensor and $\mathbf{D}_{n}\left(i,j\right)$ is the symmetric rate of strain tensor for element i,j at time-step n. The updated conformation tensor for the next update step is given by $\mathbf{W}_{n+\frac{1}{2}}\left(i,j\right)$. The update in Eq. 5.5 is performed over all elements on the lattice. Following this, the hopping rate $\Gamma(i,j)$ is calculated for each element according to equation Eq. 5.1. The test for yielding is then performed via selecting a random number r from a uniform distribution in the range $(0,1)$. The criterion is applied such that the element yields if $r < \Gamma(i,j)\Delta t$ and the microscopic conformation tensor is then reset $\mathbf{W}_{n+1}\left(i,j\right) = \mathbf{I}$. If the element does not yield $\mathbf{W}_{n+1}\left(i,j\right) = \mathbf{W}_{n+\frac{1}{2}}\left(i,j\right)$.

Following this, the flow field is calculated for the cell. Lees-Edwards boundary conditions incorporate shear via transformation into the co-sheared frame

$$(x', y', t) = (x' = x - \overline{\dot{\gamma}}ty, y' = y, t' = t). \tag{5.6}$$

The partial derivatives after this transformation are given by

$$(\partial_x, \partial_y, \partial_t) = (\partial_{x'}, -\overline{\dot{\gamma}}t\partial_{x'} + \partial_{y'}, -\overline{\dot{\gamma}}y\partial_{x'} + \partial_{t'}). \tag{5.7}$$

The cosheared 2D gradient operator then becomes

$$\nabla_c = \hat{\mathbf{x}}\partial_{x'} + \hat{\mathbf{y}}(-\overline{\dot{\gamma}}t\partial_{x'} + \partial_{y'}), \tag{5.8}$$

which is given in Fourier space by the expression

$$\tilde{\nabla}_c = \hat{\mathbf{x}}iq_{x'} + \hat{\mathbf{y}}(-\overline{\dot{\gamma}}tiq_{x'} + iq_{y'}). \tag{5.9}$$

Using this transformation, we are able to describe the evolution of the flow field in a periodic two-dimensional system subject to an applied shear-rate $\bar{\dot{\gamma}}$ and incorporate the effects of affine advection into our calculation. The quantity $\bar{\dot{\gamma}}t$, which corresponds to the affine displacement, we describe by the quantity ζ. This is incremented as the affine strain such that $\dot{\zeta} = \bar{\dot{\gamma}}$. Under the transformation described so far, the relative shear of the laboratory and cosheared frames becomes large at long times, diverging at a constant rate $\bar{\dot{\gamma}}$. The divergence between the cosheared and lab frame leads to numerical instabilities at large strains. To alleviate this, the quantity ζ is reset when $\zeta > \frac{1}{2}\frac{L_y}{L_x}$ to $\zeta = -\frac{1}{2}\frac{L_y}{L_x}$, and the elements are reset such that each element $(i, j) \rightarrow (i - jN_x/N_y, j)$. This method was previously implemented in a continuum model of demixing Newtonian fluids [205].

Using these transformed coordinates, the flow field can be solved using an Oseen tensor formulation such that in Fourier space, the flow field $\tilde{\mathbf{v}}_q$ is described by the expression

$$\tilde{\mathbf{v}}_{q'} = \frac{1}{\eta q'^2}(\mathbf{I} - \hat{\mathbf{q}}'\hat{\mathbf{q}}') \cdot (\mathbf{q}' \cdot \tilde{\sigma}_{q'}). \tag{5.10}$$

A derivation of the Oseen tensor formulation may be found in Chapter 2. The velocity gradient tensor is then calculated for each element in order to evolve the system for the next timestep.

We must first demonstrate that this implementation does show the characteristics of an elastoplastic model, along with that of a yield stress fluid. In Figure 5.1 a) we show the redistribution of the stress from a single yielding event. We first initialise all elements such that the viscoplastic shear stress $\sigma_{xy} = 1$. A single element is then artificially caused to yield. All other elements are prevented from yielding and the stress is redistributed via the flow field. We see that our model reproduces the distinctive quadrupolar stress propagation derived by Eschelby [178] and used in the model derived in Ref. [176]. We also demonstrate the steady state response of this model by computing the flow curves in Figure 5.1 b). With decreasing effective noise temperature, we observe an increasing yield stress. We note however that only $T = 0$ appears to display a true yield stress for the shear-rates explored. At higher temperatures, a small positive slope is seen even at the very low shear-rates plotted.

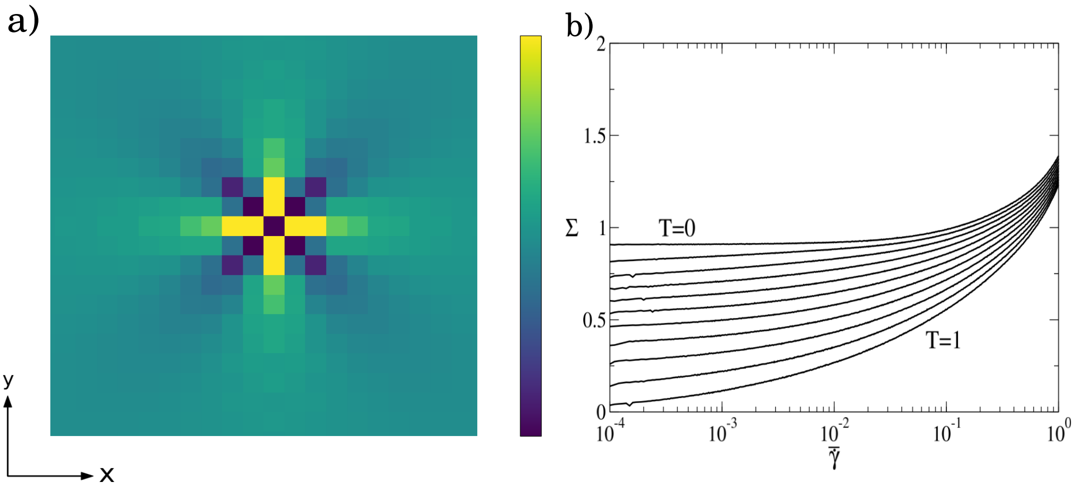

Figure 5.1: a) The quadrupolar redistribution of the elastoplastic shear stress σ_{xy}following a single local event imposed in a system with $\eta = 0.01$, $dt = 0.005$. All elements are initialised to $\sigma_{xy} = 1$ prior to yielding imposed on a single element. Plot shown $10\Gamma_0^{-1}$ after yielding imposed b) The steady state flow curves computed for a range of values of effective noise temperature, from $T = 1$ upward in increments of $\Delta T = 0.1$, to $T = 0$.

Methodology

This study seeks to establish the longevity of shear bands in systems subject to different sample preparation before start-up. The two protocols we use in this chapter have already been introduced to the reader in Chapter 4, but we shall recount them here.

The first of these protocols, which we term Protocol I, allows a waiting time prior to the application of shear. At $t = 0$, the system is quenched from $T = \infty$ to a value $0 < T < 1$. For this study we choose $T = 0.3$. The sample is then allowed to age for some waiting time t_w undisturbed, before an average shear-rate $\bar{\dot{\gamma}}$ is applied and held constant thereafter.

The second protocol (Protocol II), sets the initial temperature T_{init} of the sample above the glass transition temperature T_{g}, before cooling gradually at a fixed rate α until $T = 0$. The temperature of the sample then evolves as $T = T_{\text{init}} - \alpha t$. Here, we set this initial temperature $T_{\text{init}} = 2$, unlike the value used in the previous study in Chapter 4. This is due to the increased level of noise in the system which arises from the use of a smaller number of elements in the flow direction. As a result, the system must be better annealed in order to observe the formation of distinct shear-bands. Once the temperature $T = 0$ is reached, an average shear-rate $\bar{\dot{\gamma}}$ is applied and held constant thereafter.

In order to study the evolution of a single band, independent of the stochastic effects of the model, we perturb the system prior to imposing shear. To ensure the formation of single high shear-rate band, the energy well depth of elements of the cell is varied by the function

$$E'(x,y) = E(x,y)\left[1 + \epsilon \sin(2\pi y + \frac{\pi}{2})\right], \tag{5.11}$$

where $\epsilon = 0.1$. This relatively large perturbation effectively weakens the material sample at the centre of the cell. The elements near the centre of the cell will then yield for a much smaller applied strain, leading to the formation of a band of high shear-rate. We are then able to study the evolution of this yielded region as a function of the applied strain. We characterise the evolution of the band by the local shear-rate $\dot{\gamma}\,(x,y)$. In order to make our measurements robust to local stochastic effects, the local shear-rate is averaged over a single strain unit for all measurements.

In order to determine the width of the band w_b, the spatial average shear-rate along the $\hat{\mathbf{x}}$ direction is measured at each unit of strain as

$$\dot{\gamma}\,(y,\langle\bar{\gamma}\rangle) = \frac{1}{L_x}\int_0^{L_x}\int_{\bar{\gamma}-1}^{\bar{\gamma}} \dot{\gamma}\,(x,y,\bar{\gamma})\,d\gamma dx. \tag{5.12}$$

The position of the edge of the band is determined by comparing the value of $\dot{\gamma}\,(y,\langle\bar{\gamma}\rangle)$ to the imposed average shear-rate $\bar{\dot{\gamma}}$. The position of the band interface is defined to be where $\dot{\gamma}\,(y,\langle\bar{\gamma}\rangle)$ first exceeds $\bar{\dot{\gamma}}$ moving inwards from the edge of the cell. This is calculated moving inwards from $y = 0$ and $y = L_y$. The width of the band is then taken as the difference between these values. Examples of these profiles for several values of strain are shown in Figure 5.2. The interface is defined as where the high shear-rate band at the centre of the channel first exceeds the line designating the average shear-rate.

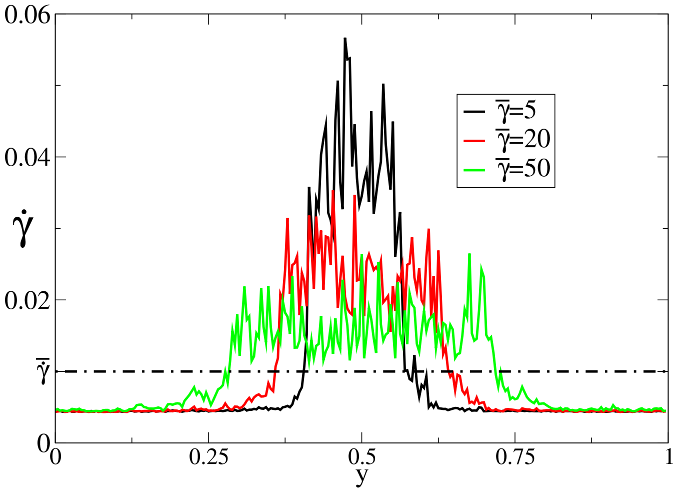

Figure 5.2: Profiles of shear-rate at several values of strain for a shear-banded sample. The average shear-rate is marked as a dashed line. The interface position is taken as the value of y at which the local shear-rate first exceeds the average strain-rate $\bar{\dot{\gamma}}$ as measured from either edge of the cell. Sample parameters $T = 0.3$, $t_w = 10^6$, $\bar{\dot{\gamma}} = 0.01$, $\eta = 0.01$, $N_x = 256$, $N_y = 256$, $dt = 0.005$.

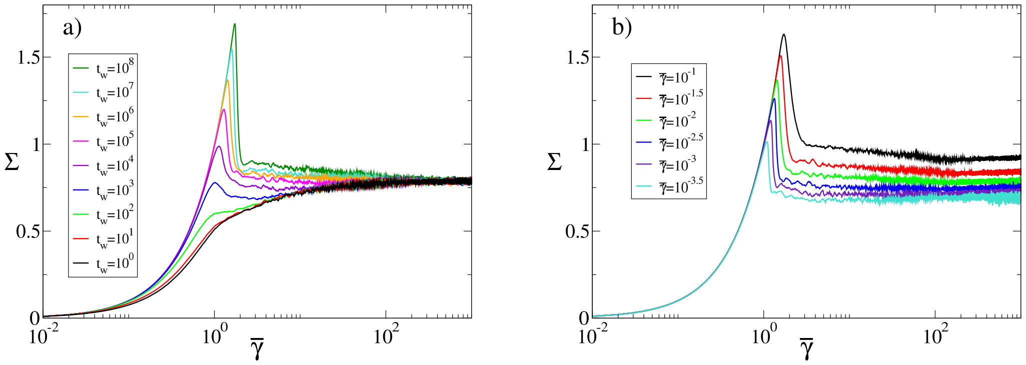

Figure 5.3: Start-up curves $\bar{\dot{\gamma}} = 0.01$ for system parameters $T = 0.3$, $\eta = 0.01$, $N_x = 256$, $N_y = 256$, $dt = 0.005$ a) for a range of sample ages t_w, b) for a range of applied shear-rates $\bar{\dot{\gamma}}$. Overshoot height increases with both sample age and shear-rate.

5.4 Results: Protocol I

5.4.1 Shear Start-up

Moorcroft et al. used a one-dimensional implementation of the soft glassy rheology model to study the onset of banding in aged systems [25]. It was observed that the bands can be extremely long lived. We now use a 2D lattice SGR model to characterise this longevity. Fig 5.3 a) shows the evolution of the average shear-stress in the system for different sample ages. We observe stress overshoots during start-up. The overshoot height increases with sample age in accordance with experiment [21] and simulations [28, 33] of soft glassy materials. Following an elastic like response at low strain, we observe the system yield and begin to fluidise. The stress then decreases to a value which is independent of the initial sample age t_w.

For fixed sample age and varying shear-rate in Figure 5.3 b), the overshoot height increases with applied shear-rate [21, 73, 77]. This behaviour is widely seen in experiment [64, 73], as well as in simulation [28, 33]. This was also found to be the case in our study performed in Chapter 4, which modelled the emergence of shear-bands during start-up in a one-dimensional flow. In that study, we observed that the degree of banding increased with sample age, but did not study the evolution of the bands after yielding. We shall now examine how these bands evolve with time.

5.4.2 Banding Profiles

During start-up, the material initially deforms as an elastic solid before it reaches the overshoot. After the overshoot, the material yields to a plastic flow. During this transition, shear-bands form due to the material yielding from elastic to plastic behaviour inhomogeneously. As the strain increases, the regions which are fluidised gradually grow until the entire system has a uniform shear-rate.

We show this for two samples aged for different waiting times in Figure 5.4. These plots show the local shear-rate averaged over a single strain unit $\dot{\gamma}\left(x, y, \langle\bar{\gamma}\rangle\right)$. Prior to shear, both samples are aged at $T = 0.3$ for a waiting time t_w. A perturbation is applied to weaken the centre of the cell, as described above, which leads to the formation of a single high shear-rate band. This corresponds to the brighter regions of the colour-plots shown. The systems are aged for $t_w = 10^5$ (Left) and $t_w = 10^6$ (Right). In both cases, we see that a shear-band forms and the high shear-rate band (brighter region) grows outwards with increasing strain (panels top to bottom in figure). We observe that the younger system fluidises more rapidly, with the band expanding outwards to fill the cell by $\bar{\gamma} = 90$ in the case of the system aged for $t_w = 10^5$. The yielded region remains localised for the system aged for $t_w = 10^6$.

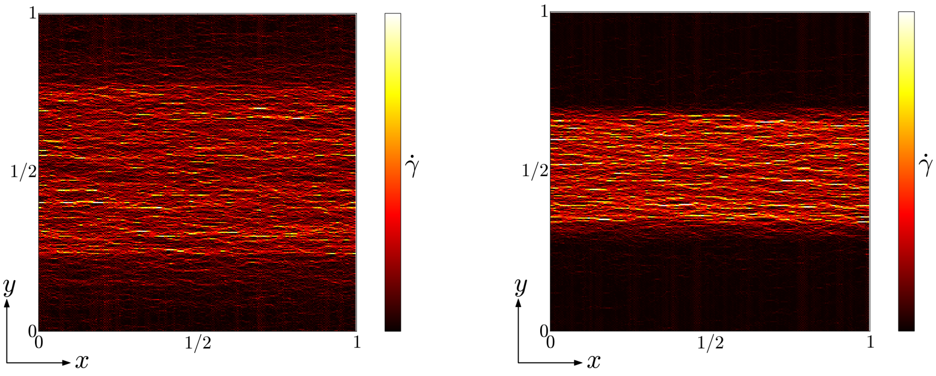

(a) $t_w = 10^5$,$\bar{\gamma} = 30$

(b) $t_w = 10^6$,$\bar{\gamma} = 30$

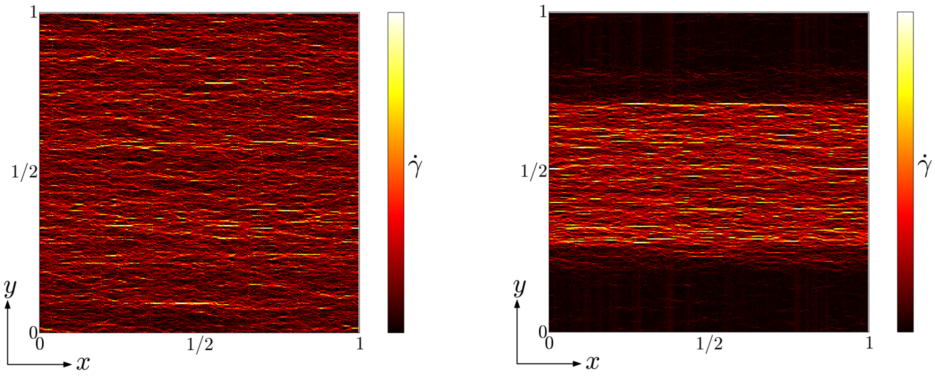

(c) $t_w = 10^5$,$\bar{\gamma} = 60$

(d) $t_w = 10^6$,$\bar{\gamma} = 60$

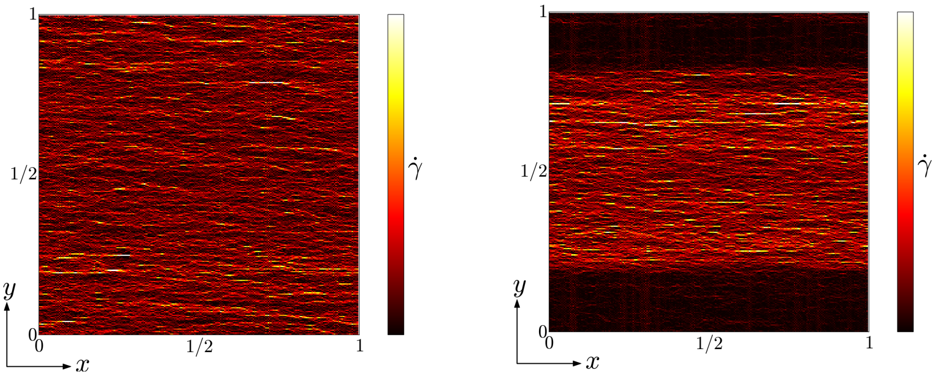

(e) $t_w = 10^5$,$\bar{\gamma} = 90$

(f) $t_w = 10^6$,$\bar{\gamma} = 90$

Figure 5.4: Colourscale of local shear-rate averaged over a single strain unit $\dot{\gamma}(x, y, \langle\bar{\gamma}\rangle)$. $\bar{\dot{\gamma}} = 0.01$, $T = 0.3$,$N_x = 256$, $N_y = 256$, $dt = 0.005$. Left) System aged for $t_w = 10^5$ prior to applied shear. Right) System aged for $t_w = 10^6$ prior to applied shear. Top) $\bar{\gamma} = 30$. Middle) $\bar{\gamma} = 60$. Bottom) $\bar{\gamma} = 90$.

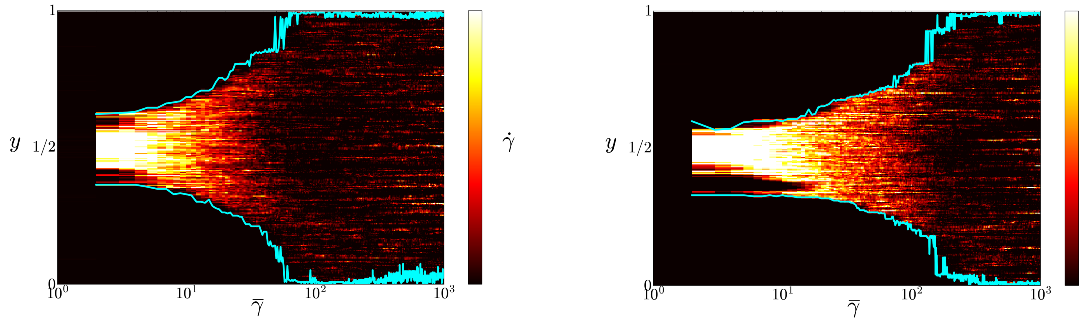

(a) $t_w = 10^4$, $\bar{\dot{\gamma}} = 0.01$

(b) $t_w = 10^6$, $\bar{\dot{\gamma}} = 0.01$

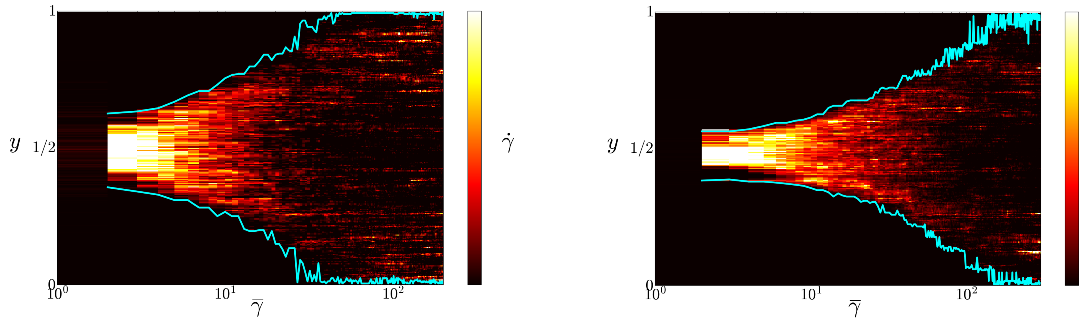

(c) $t_w = 10^4$, $\bar{\dot{\gamma}} = 0.001$

(d) $t_w = 10^6$, $\bar{\dot{\gamma}} = 0.001$

Figure 5.5: Colourmap of $\dot{\gamma}(y, \langle\bar{\gamma}\rangle)$ as a function of strain for $\eta = 0.01, N_x = 256, N_y = 256, dt = 0.005$ a) $t_w = 10^4$, $\bar{\dot{\gamma}} = 0.01$. b) $t_w = 10^6$, $\bar{\dot{\gamma}} = 0.01$. c) $t_w = 10^4$, $\bar{\dot{\gamma}} = 0.001$. d) $t_w = 10^6$, $\bar{\dot{\gamma}} = 0.001$.

The growth of these bands as a function of time is plotted in Figure 5.5. These colour-maps show the value of the local shear-rate averaged over a single strain unit and integrated along the $\hat{x}$ direction of the cell as described by Eq. 5.12. The position of the bands is calculated using the algorithm described previously. The fluidised band expands outwards from the centre of the cell with increasing strain. As the age of the sample increases, we see that the time for the bands to reach the complete system size also increases.

In Figure 5.6 a), we observe the growth of the band width w_b for fixed shear-rate at varying ageing times. Refs. [28, 33, 34, 173] demonstrate the width of the bands to grow as a power law $\bar{\gamma}^{\frac{1}{2}}$. We take a power law fit of the growth of the bands here, as well as measuring the initial band width w_0. In Figure 5.6 b) the value of the exponent β is found only to vary a little with sample age, with

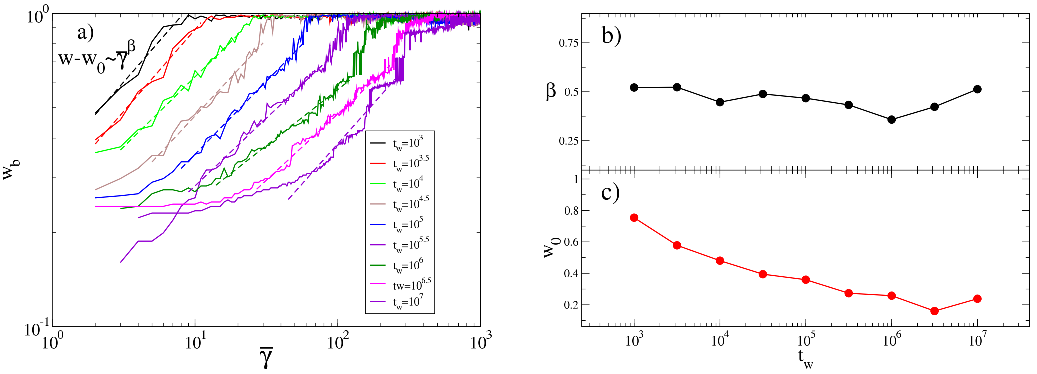

Figure 5.6: a) The growth of shear-band width w_b as a function of average shear-strain $\bar{\gamma}$ for fixed average shear-rate $\bar{\dot{\gamma}} = 10^{-2}$ for varying sample age t_w. Data from simulations (solid lines) are fitted to power laws expression $w_b - w_0 \sim \bar{\gamma}^{\beta}$ (broken lines). b) Exponent β as a function of waiting time t_w. c) Initial band width w_0 as a function of waiting time t_w. Model parameters $T = 0.3$, $\eta = 0.01$, $N_x = 256$, $N_y = 256$, $dt = 0.005$.

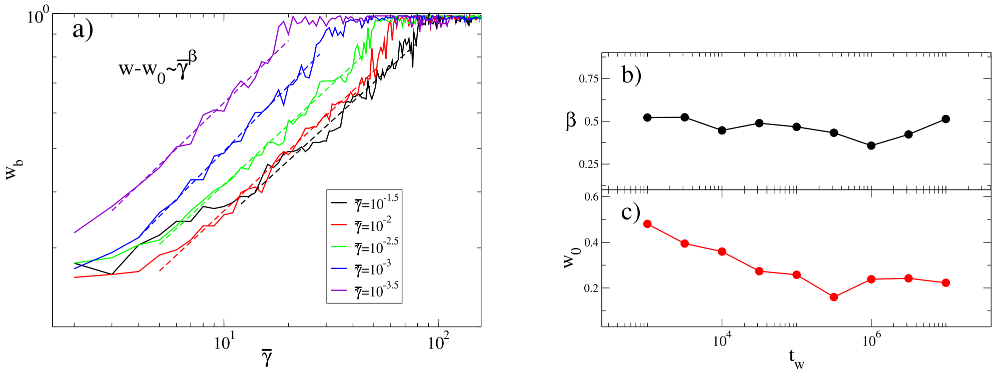

Figure 5.7: a) The growth of shear-band width w_b as a function of average shear-strain $\bar{\gamma}$ for fixed sample age $t_w = 10^5$ for varying applied shear-rate $\bar{\dot{\gamma}}$. Data from simulations (solid lines) are fitted to power laws expression $w_b - w_0 \sim \bar{\gamma}^{\beta}$ (broken lines). b) Exponent β as a function of applied shear-rate $\bar{\dot{\gamma}}$. c) Initial band width w_0 as a function of applied shear-rate $\bar{\dot{\gamma}}$. Model parameters $T = 0.3$, $\eta = 0.01$, $N_x = 256$, $N_y = 256$, $dt = 0.005$.

$\beta \approx 0.5$ for all measured samples. In contrast, we see the initial width of the band w_0 in Figure 5.6 c) decreases with sample age. Such behaviour was also seen in the theoretical work of Manning et al. [170], which saw the measured band thickness decrease with initial effective temperature in an STZ model. It was also observed in the simulations of Hinkle and Falk for decreasing cooling rate [34].

In Figure 5.7 a) the growth of the band width w_b for several values of applied shear-rate $\bar{\dot{\gamma}}$ is plotted as a function of average strain $\bar{\gamma}$. The calculated power law exponents are once again found to vary only a small amount with shear-rate, with most values of $\beta \approx 0.5$. We therefore see that this model successfully replicates the $w_b \sim \bar{\gamma}^{\frac{1}{2}}$ band growth described in simulations. We also see that the initial width of the bands decreases with increasing shear-rate. Having observed the formation and development of shear-bands with time, we now see how the time taken for the system to completely fluidise varies with shear-rate and preparation.

5.4.3 Band Longevity

The time at which the system has become completely fluidised τ_f, corresponds to the time at which the bands reach the edge of the cell. In order to mitigate the effects of noise encountered as the band begins to meet itself at the edge of the cell, we define the fluidisation time as when the band width $w_b = 0.95L_y$. The values of this fluidisation time τ_f are plotted as a function of sample age for several values of applied shear-rate in Figure 5.8 a). We observe the fluidisation time increase with decreasing applied shear-rate $\bar{\dot{\gamma}}$ as observed in the simulations of Shrivastav et al. [33]. The calculated exponents of these power laws are included in the inset in Figure 5.8 a). For the sample ageing times here, we observe an increase in the exponent with sample age. All exponents are less than unity and generally increase with the value of t_w. The findings of Ref. [33] also find the longevity of shear bands to increase as a power law, with exponent -1.28, for a sample aged for a single waiting time. This is in accordance with experimental studies of shear-band longevity in yield stress fluids [27, 70], which also observe such a power law dependence. Our results are somewhat in contrast to previous findings as no former study known to this author measures this exponent to be less than 1. In Figure 5.8 b) the fluidisation time as a function of sample age t_w is plotted for several applied shear-rates. We find that for all values of $\bar{\dot{\gamma}}$, the time taken for shear bands to dissipate follows a power law $t_w^{1/2}$.

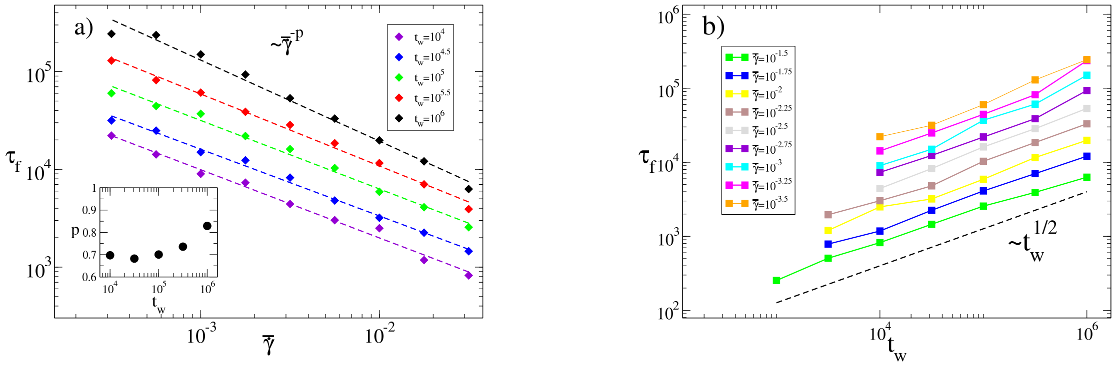

Figure 5.8: a) The fluidisation time as a function of applied average shear-rate $\bar{\dot{\gamma}}$ for several values of sample age t_w. Data from simulations (symbols) fitted to power laws (dashed lines). Inset) Calculated power law exponents. b) The fluidisation time as a function of waiting time t_w. Power law $t_w^{\frac{1}{2}}$ (dashed line) included as guide for the eye.

5.5 Results: Protocol II

We now seek to examine how heterogeneous flow develops in systems with zero noise temperature. The protocol for sample preparation in this limit is inspired by work done by Vashist and collaborators in simulation [29, 32]. Their studies were performed for a Leonard-Jones glass cooled from above the glass transition to zero temperature.

5.5.1 Shear Start-up

We observe in Figure 5.9 a), that as the cooling rate applied to the sample is decreased, the stress overshoot increases. This is in agreement with the simulations in Refs. [29, 32]. Our findings show a variation in overshoot height as a function of both shear-rate $\bar{\dot{\gamma}}$ and cooling rate α which are in accordance with the results of their studies. In Figure 5.10, the height of the overshoots $\Delta\Sigma$ is plotted as a function of the cooling rate and the applied shear-rate. We see that on a semi-log scale, the height of the overshoot plotted as a function of the cooling rate α in Figure 5.10 a), follows a straight line. This indicates that the overshoot height has an exponential dependence on the cooling rate.

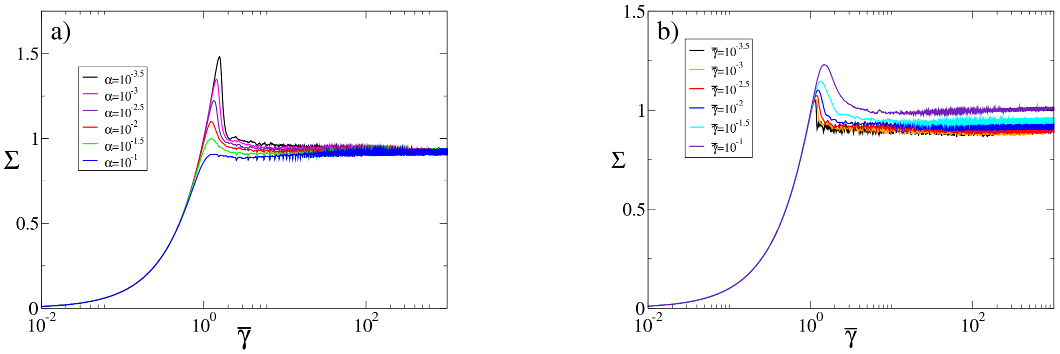

Figure 5.9: The evolution of the system average shear-stress for systems under imposed average shear-rate for simulation parameters $\eta = 0.01$, $N_x = 256$, $N_y = 256$, $dt = 0.005$. a) Shear start-up curves for a range of samples cooled to $T = 0$ for $T_{init} = 2$ at a range of cooling rates at fixed applied average shear-rate $\bar{\dot{\gamma}} = 0.01$. Overshoots increase with decreasing cooling rates corresponding to more well annealed samples. b) Shear start-up curves for samples with fixed cooling rate $\alpha = 0.01$ for a range of applied average shear-rate $\bar{\dot{\gamma}}$. Overshoots decrease with decreasing shear-rate, as well as experiencing a more abrupt drop off in stress at the overshoot.

In Figure 5.10 b), we plot the overshoot height against shear-rate. Our results corresponds closely to Figure 12 c) of Ref. [29]. This differs somewhat from the results of Chapter 4 of this thesis, which implemented this protocol for a 1D SGR model. In Chapter 4 we observed very little variation in overshoot height with shear-rate. This may be attributed to the noise effects of the SGR model. In the previous chapter 80'000 elements are used to model the flow direction. This minimizes the variation between the small number of streamlines due to the stochastic effects in the SGR model. In this chapter we perform calculations for a system of 256×256 elements. This results in a much greater degree of variation in the stress response over the cross flow direction, thereby causing the system to yield at lower strains and with a much larger effect of shear-rate. Further studies using a greater number of element in a Lattice SGR model may replicate the findings in Chapter 4, but may be extremely computationally expensive. In line with the findings of Chapter 4, and those of simulations of shear start-up in athermal soft glasses [24, 29, 30, 32], yielding becomes more severe with decreasing shear-rate.

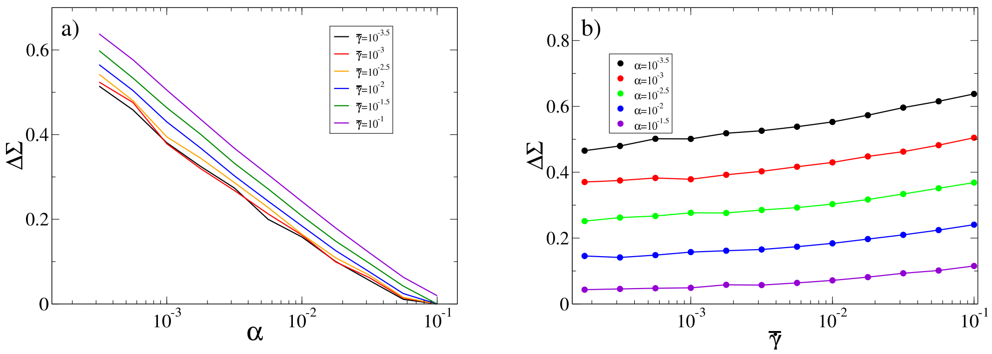

Figure 5.10: a) Overshoot height $\Delta\Sigma$ plotted as a function of cooling-rate α for a range of values of shear-rate $\dot{\bar{\gamma}}$. b) as a function of shear-rate for a range of cooling rates. $T = 0$, $T_{\text{init}} = 2$ $\eta = 0.01$, $N_x = 256$, $N_y = 256$, $dt = 0.005$.

5.5.2 Band Profiles

In the previous protocol, the system was prepared prior to shear by ageing the sample at a fixed temperature. In this protocol, we instead cool the sample at a fixed rate to the athermal limit $T = 0$ from T_{init}. Systems cooled at slower rates are better annealed, so we expect to see shear-bands persist longer as the cooling rate is decreased. Full colour-maps of the local shear-rate $\dot{\gamma}\,(x, y)$ averaged over a single strain unit are shown in Figure 5.11. We see that the more rapidly cooled sample fluidises more quickly, with the shear-rate almost homogeneous by the largest strain $\bar{\gamma} = 90$ for $\alpha = 10^{-2}$. In the $\alpha = 10^{-3}$ system, which was cooled more slowly, the cell retains a large region at almost no shear-rate and the interface between the banded and non-banded region is quite sharp. As seen in the previous protocol, the fluidised band spreads outwards to encompass the entire cell.

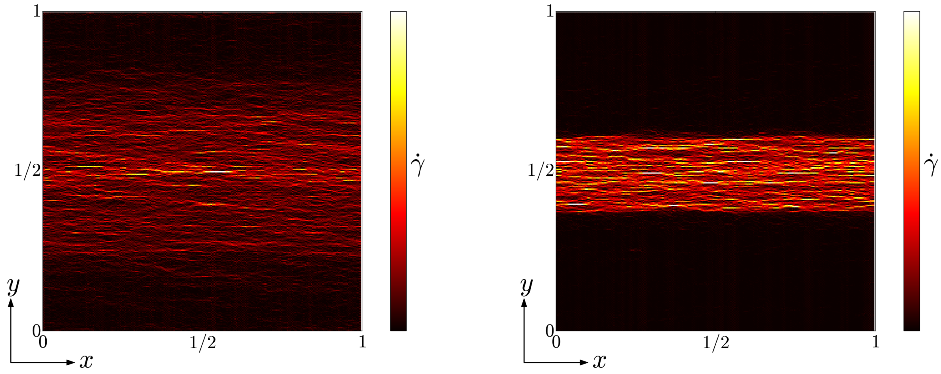

(a) $\alpha = 0.01$, $\bar{\gamma} = 30$ (b) $\alpha = 0.001$, $\bar{\gamma} = 30$

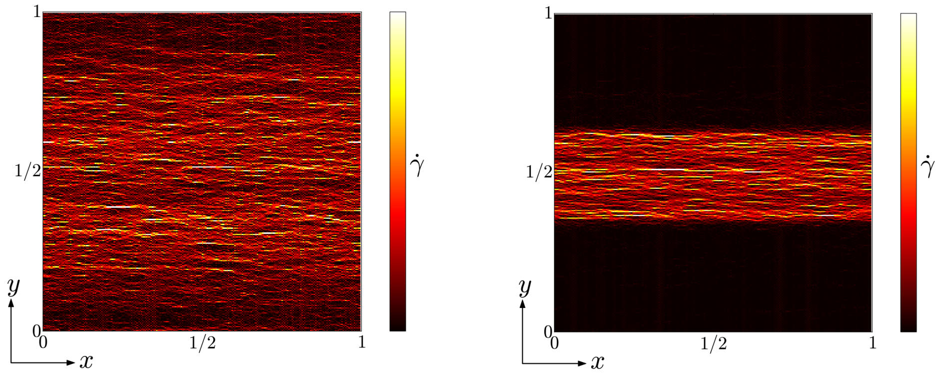

(c) $\alpha = 0.01$, $\bar{\gamma} = 60$ (d) $\alpha = 0.001$, $\bar{\gamma} = 60$

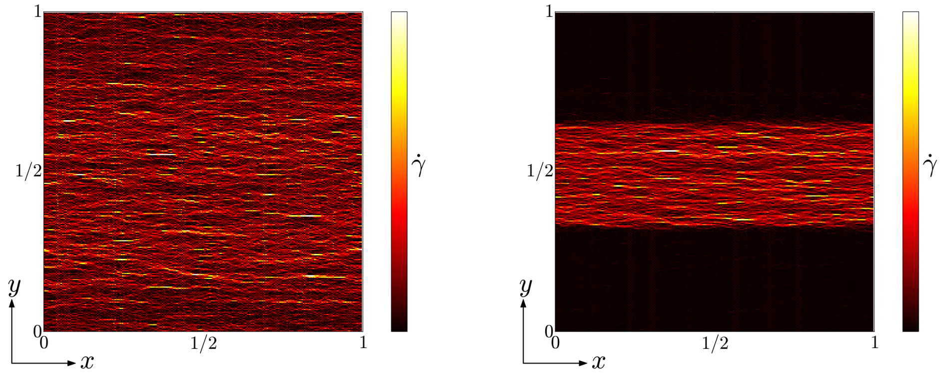

(e) $\alpha = 0.01$, $\bar{\gamma} = 90$ (f) $\alpha = 0.001$, $\bar{\gamma} = 90$

Figure 5.11: Colourscale of local shear-rate $\dot{\gamma}\left(x, y, \langle\bar{\gamma}\rangle\right)$ averaged over a single strain unit. $\overline{\dot{\gamma}} = 0.01$, $T = 0.0$,$T_{\text{init}} = 2$, $\eta = 0.01$, $N_x = 256$, $N_y = 256$, $dt = 0.005$, Left) System cooled at $\alpha = 10^{-2}$ prior to applied shear. Right) System cooled at $\alpha = 10^{-3}$ prior to applied shear. Top) $\bar{\gamma} = 30$. Middle) $\bar{\gamma} = 60$. Bottom) $\bar{\gamma} = 90$.

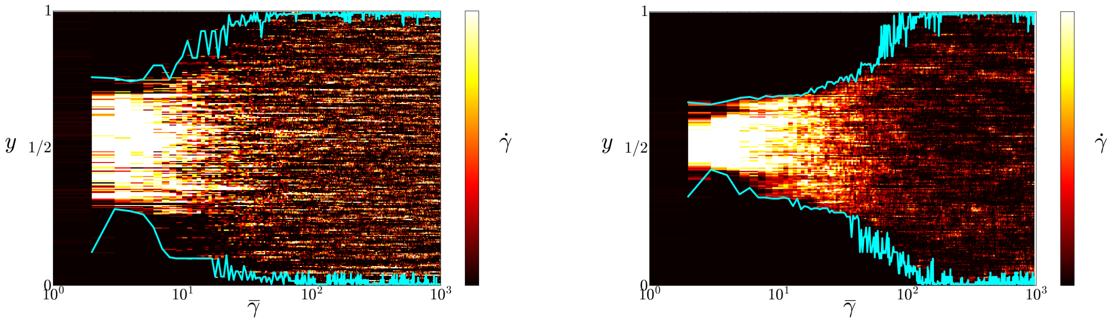

(a) $\alpha = 0.01$, $\dot{\bar{\gamma}} = 0.1$

(b) $\alpha = 0.001$, $\dot{\bar{\gamma}} = 0.1$

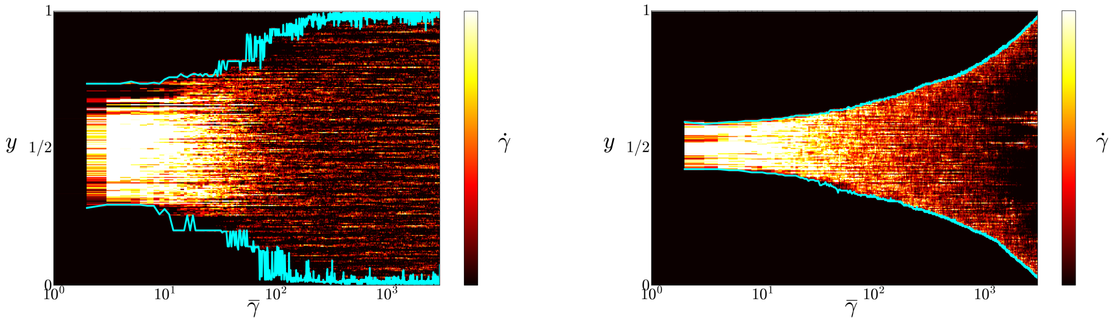

(c) $\alpha = 0.01$, $\dot{\bar{\gamma}} = 0.01$,

(d) $\alpha = 0.001$, $\dot{\bar{\gamma}} = 0.01$

Figure 5.12: Colourmap of $\dot{\gamma}(y, \langle\bar{\gamma}\rangle)$ as a function of strain for $T = 0$, $T_{\text{init}} = 2$, $\eta = 0.01, N_x = 256, N_y = 256, dt = 0.005$. a) $\dot{\bar{\gamma}} = 0.1$, $\alpha = 0.01$. b)$\dot{\bar{\gamma}} = 0.01$, $\alpha = 0.001$. c) $\dot{\bar{\gamma}} = 0.1$, $\alpha = 0.001$. d) $\dot{\bar{\gamma}} = 0.01$, $\alpha = 0.001$

As previously, we integrate along the $\hat{x}$ direction in the cell to examine the spread of the band as a function of strain. Four samples are shown for this protocol in Figure 5.12. As shown in the full colour plots, the system remains banded at larger strains for the more gradually cooled sample, as they do for larger ageing times in Protocol I. In contrast to the previous protocol however, we observe that for lower shear-rates bands diffuse more slowly. This is in accordance with the findings of both experiment [27, 64, 70] and simulation [32, 33]. This implies that the lattice SGR model sucessfully captures the dynamics of shear banded yield stress fluids at this athermal limit.

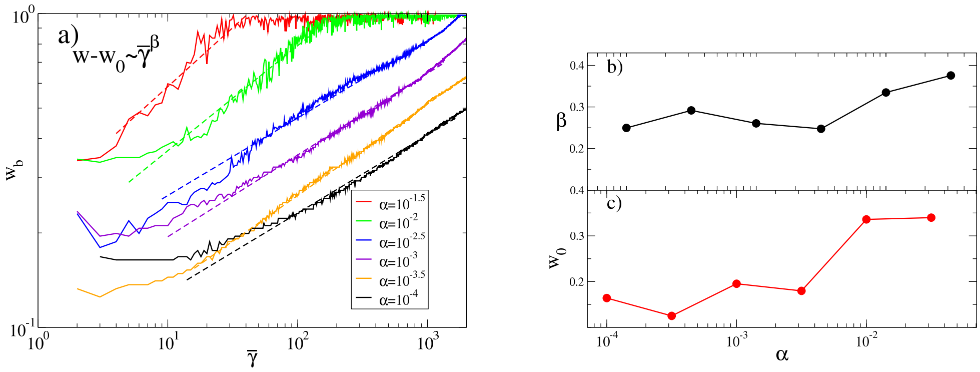

Figure 5.13: a) The growth of shear-band width w_b as a function of average shear-strain $\bar{\gamma}$ for fixed shear-rate $\bar{\dot{\gamma}} = 10^{-2}$. Data from simulations (solid lines) are fitted to power laws expression $w_b - w_0 \sim \bar{\gamma}^\beta$. b) Exponent β as a function of cooling rate α. c) Initial band width w_0 as a function of cooling rate α. Model parameters $T = 0$, $T_{init} = 2$, $\eta = 0.01$, $N_x = 256$, $N_y = 256$, $dt = 0.005$.

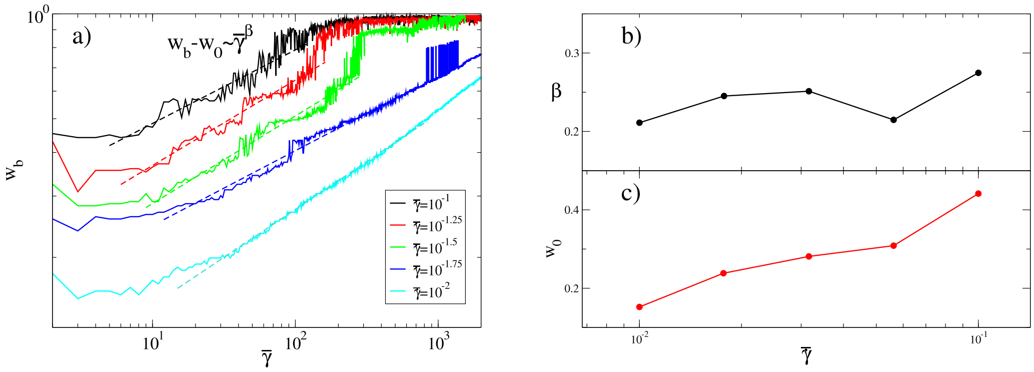

Figure 5.14: a) The growth of shear-band width w_b as a function of average shear-strain $\bar{\gamma}$ for fixed cooling rate $\alpha = 10^{-3}$ Data from simulations (solid lines) are fitted to power laws expression $w_b - w_0 \sim \bar{\gamma}^\beta$. b) Exponent β as a function of applied shear-rate $\bar{\dot{\gamma}}$. c) Initial band width w_0 as a function of applied shear-rate $\bar{\dot{\gamma}}$. Model parameters $T = 0$, $T_{init} = 2$, $\eta = 0.01$, $N_x = 256$, $N_y = 256$, $dt = 0.005$.

The width of the bands w_b is plotted as a function of strain in Figure 5.13 a) for a range of cooling rates at fixed strain-rate $\bar{\dot{\gamma}}$. As in Protocol I, we find that the growth follows a power law, however not the $\bar{\gamma}^{\frac{1}{2}}$ seen previously. Instead we see the value of the exponent drop with decreasing cooling rate in Figure 5.13 b) to a value near $\beta \approx 0.3$. We also see a variation in the initial width of the bands drop considerably with decreasing cooling rate in Figure 5.13 c) in line with the findings of particle simulations for cooled metalic glasses [34].

In Figure 5.14 a), the growth of the bands is plotted at a range of shear-rates at fixed cooling rate. Here we observe once again an only small variation in the growth exponent of the bands, as plotted in Figure 5.14 b). We also observe a large decrease in initial band width in Figure 5.14 c) with decreasing shear-rate. This is in contrast to the behaviour observed in Protocol I, which showed the bands being initially smaller at higher shear-rates. They are, however, in agreement with the calculations of Ref. [170] and the particle simulations of Ref. [34], both of which observed smaller initial band width at smaller shear-rates.

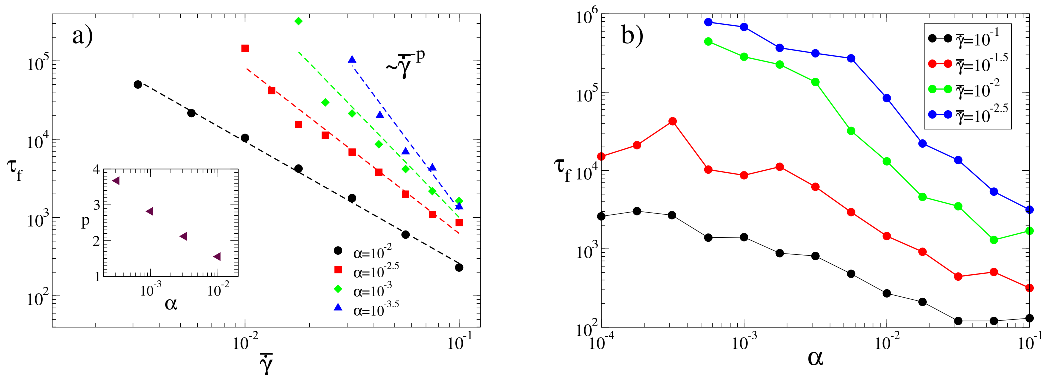

Figure 5.15: a) The fluidisation time as a function of shear-rate for several cooling rates. Data points are shown as symbols, with lines of best fit to a power law expression $\tau_f \sim \bar{\dot{\gamma}}^{-p}$ shown as broken lines. Inset) Calculated exponents p as a function of cooling rate α. b) The fluidisation time as a function of cooling rate α for a range of values of imposed average shear-rate $\bar{\dot{\gamma}}$.

5.5.3 Band Longevity

As in the case of the first protocol, we calculate the longevity of the bands based on the time at which they obtain a width $w_b = 0.95L_y$. This τ_f is the time at which the system can be considered to be completely fluidised. Plotting τ_f as a function of applied average shear-rate $\bar{\dot{\gamma}}$ in Figure 5.15 a) demonstrates a power-law dependence similar to that seen in the results of Vashist and collaborators [32] for the same protocol. For a Leonard-Jones glass cooled at various rates, they observe the longevity of shear-bands to increase with decreasing shear-rate. They also observe the exponent of these power-laws to increase as a function of decreasing cooling rate. As in their study, we plot the calculated exponents of these power laws as a function of cooling rate α (see Figure 5.15 a) Inset). Over four decades in cooling rate ($5 \times 10^{-2} - 5 \times 10^{-6}$) they observe an increase in the exponent from 1.11 to 1.66, while our results show a much larger increase from $p \approx 1.5$ to $p \approx 3.8$ over only one and a half decades.

Despite this larger variation, we observe the same trend in exponent with cooling rate. The exponent p follows a linear dependence on cooling rate α on a semi-log scale, indicating an exponential dependence as observed for the overshoot. The longevity of the bands as a function of cooling rate for fixed imposed shear-rate

$\bar{\dot{\gamma}}$ is plotted in Figure 5.14 b). The longevity of the bands increases with decreasing cooling rate. At very low cooling rates the value of τ_f appears to plateau. This plateau value increases with decreasing imposed shear-rate.

5.6 Conclusions and Future Work

The study performed in this chapter examines the longevity of shear-bands that form during shear start-up in an elastoviscoplastic fluid. We have performed this study using a novel elastoplastic lattice model that incorporates SGR dynamics to simulate the effects of temperature [28, 29, 32, 33, 169] and experiment [21, 73]. Our findings match qualitatively many of the results of prior studies, but also show some differences which suggest that further research is required.

In the first protocol, the system is aged at a fixed temperature for a waiting time t_w before being sheared at a fixed rate $\bar{\dot{\gamma}}$ at effective noise temperature $T = 0.3$. This protocol is most closely matched in simulation by the work of Ref. [28, 33]. In agreement with their findings, we see larger overshoots during shear start-up for longer aged materials and for higher imposed average shear-rates. Our findings also show longer lived shear bands for smaller shear-rates in accordance with the findings of Ref. [28]. We also observe that as the fluidised band grows outwards from the centre of the cell, the growth follows a power law function of average strain, displaying the $\bar{\gamma}^{1/2}$ relation seen in that study as well as Refs. [34]. Our findings also demonstrate that the lifetime of the bands increases with decreasing shear-rate as a power law function of $\bar{\dot{\gamma}}$. In our study, all calculated exponents were less than one, unlike the finding of Ref. [33]. This suggests that while our model successfully describes many of the features of shear-banded systems at finite temperature, but fails to capture others. We note however, that the exponent of these power laws increases with sample age t_w, suggesting that further simulations with larger waiting times may capture the results of simulation, or that simulations for lower ageing times may see the behaviour we observe here.

In the second protocol, our methodology closely followed that of the works in Refs. [29, 32], which performed simulations of a Leonard-Jones glass cooled to the athermal limit. The simulations performed in Ref. [32] demonstrated the fluidisation time τ_f to be a power-law function of the applied average shear-rate $\bar{\dot{\gamma}}$. The exponent of this power law varied between 1.11 and 1.66, for cooling rates 5×10^{-2} and 5×10^{-6}. These power laws are fitted over a range of shear-rates between $\bar{\dot{\gamma}} = 10^{-4}$ to 10^{-1}. Our results show a qualitative agreement with these findings, and we observe that the time for fluidisation increases with decreasing average shear-rate. Unfortunately we have not been able to perform our simulations over as many decades in shear-rate due to computational limitations. The exponent of these power-laws also increases with decreasing cooling rate, as seen in Ref. [32]. Our calculations show a greater variation in the exponent with cooling rate (1.5 to 3.8 for a variation in α from 10^{-2} to $10^{-3.5}$). This may be the result of finite system size effects in simulation which are not accounted for in the ageing dynamics of SGR. Future work combining simulations with this new model may prove useful to establish the parameters for which it may best replicate the findings of simulation.

We may understand the differing effectiveness of the model to reproduce the results of simulation by comparing the protocols to one another. In the first protocol, the sample is aged prior to shear. With increasing sample age t_w, the average depth of energy wells increases, and the system is better annealed. The sample is then subject to a fixed imposed shear-rate at a non-zero noise temperature $T = 0.3$. In the second protocol, the average well depth increases with decreasing cooling rate α. Shear is then applied at the athermal limit $T = 0$. Therefore, the development of the bands over time may be linked to the effects of non-zero temperature while a shear-rate is imposed. Further studies modelling the effects of varying noise temperature on shear-bands (as performed in Ref. [28]) may provide better understanding of these effects.

This study seeks to examine the behaviour of shear bands formed in a sample of a yield stress fluid during shear start-up. By studying such behaviour for other start-up protocols, we could further assess the effectiveness of this model to simulate the dynamics of soft glassy materials. Studies of shear-banding have been performed for stress imposed flows in both experiment [70] and simulation [169]. They have shown the fludisation time to follow a power law $\tau_f \sim (\Sigma - \Sigma_y)^{-\beta}$, where Σ_y is the fluid yield stress. In the experiments of Ref. [64], it was found that the ratio of the band longevity exponents of this protocol and that of the shear start-up protocols corresponded to the Herschel-Bulkley exponent of the material. A next step in order to evaluate the effectiveness of this model would be to examine the formation of shear-bands in such a flow protocol.

In this study we have introduced a new model of an elastoviscoplastic material that can effectively replicate much of the behaviour observed in simulation and experiment. This may prove especially useful to examine the connection between macroscopic yielding and the preceeding mesoscopic behaviour. Experimental studies have found evidence for microscopic precursors to failure in the form of local plastic yielding and non-affine particle motion [206–208]. To this authors knowledge, these observations have not yet been explored in a mesoscopic model of soft materials. In particular, how these effects may act as precursors to the formation of shear-bands offers an unsolved mystery to theoreticians. A next step for this research could be to study how the mechanism for the development of shear bands during yielding may imitate local nucleation during a phase transition. In experiments of granular materials the formation of shear-bands has been linked to microbands which may also occur in soft materials [209–211]. In order to observe these, as well as other possible precursors, we may perform further simulations without the initial perturbation used to seed the bands in this study. The development of macroscopic fluidised regions from uncorrelated (or initially uncorrelated) plastic events is a clear next step for our research. This will require statistical analysis of elements yielding, local shear-rates and non-affine motion to be undertaken, such as the calculation of spatial or time correlation functions.

Following their formation, other questions about the development of shear shear bands remain, such as the effects of temperature on their growth. In this study we have seen how the broadening of shear bands is affected by preparation and applied shear-rate, but also see discrepancies between the growth of shear bands with and without effective noise temperature. Further investigations into the effects of temperature on the growth of shear bands may be of interest to describe how these materials fluidise with time. By artificially setting the initial distribution of energy wells and only varying the effective temperature at which shear is applied we may investigate these effects more closely. Our study does not probe the effects of normal stress difference on shear-band development, despite the inclusion of normal stress terms in our model. Previously developed elastoplastic models have neglected these terms [31, 176], and we should carefully examine their influence on the macroscopic dynamics following yielding in future work.

Chapter 6

Conclusions

In this thesis, we have studied shear flow instabilities in two types of complex fluid using numerical simulation: shear-thinning polymeric fluids and yield stress fluids. Although our studies may appear disparate, shear-thinning acts as a common rheological property connecting our studies. Yield stress fluids typically display a large degree of shear-thinning, with the viscosity of a Bingham fluid $\eta\left(\dot{\gamma}\right) \sim \dot{\gamma}^{-1}$. Transient shear-banding, the focus of our studies in Chapters 5 & 6 has been shown in previous studies to occur in the shear-thinning polymeric fluids studied in Chapter 3 [69]. The studies undertaken in this thesis may therefore be considered a general investigation into flow instabilities arising in shear-thinning complex fluids. Future work may determine further connections between the instabilities studied here, such as the influence of normal stress effects on yielding and fluidisation of soft glassy materials. We now outline the key findings of each study, and some possible avenues for future research that may further advance the field.

6.1 Linear Instability of Shear-Thinning Pressure-Driven Channel Flow

Summary of main results. In this chapter we studied the linear instability of a one-dimensional base state to two-dimensional perturbations for a shear-thinning viscoelastic fluid. We determined, in each of the models studied, the critical pressure drop required to observe instability P'^{*} as a function of model parameters using linear stability analysis. Our studies are the first to demonstrate this instability in the Rolie-Poly and Johnson-Segalman models, for which we also conduct full non-linear simulations. Using these calculated values and the steady state flow curves for each model, we constructed empirically a generalised functional form that predicts the critical pressure drop in all studied models. In this chapter, we also reproduced the basic results of Ref. [14] for stability of the White-Metzner model in pressure-driven channel flow. The criterion we developed is also effective in predicting instability in this model.

All models studied show some general behaviour, which suggests that the mechanism that leads to instability may be universal. Most notable of these is the functional form

$$\frac{dN_1}{dy}|_{max} > f\left(\frac{d\log\Sigma}{d\log\dot{\gamma}}|_{min}\right), \tag{6.1}$$

where

$$f(\zeta) = \alpha_0 + \alpha_1/(\alpha_2 - \zeta). \tag{6.2}$$

We have demonstrated this functional form to be reasonably effective in predicting instability in all models studied. In each model the fitting parameters α_0, α_1 and α_2 differed. α_2 demarks the largest value of $\frac{d\log\Sigma}{d\log\dot{\gamma}}|_{min}$ for which instability was observed and a different minimum degree of shear-thinning was required to observe instability in each model. The Johnson-Segalman model, for which $\alpha_2 \approx 0.11$, is shown to be the most stable model studied, while White-Metzner, with $\alpha_2 \approx 0.31$, is the most unstable. The Rolie-Poly model was found to be unstable for $\frac{d\log\Sigma}{d\log\dot{\gamma}}|_{min} < 0.21$. It is unclear from our study what leads to this variation, and it may be linked to the dynamics of the particular model in question. The degree of shear-thinning for which instability is observed in all studied models is within the range for which it was shown in experiment [18–20].

Further commonalities in our results suggest a general mechanism underlying the observed behaviour. Eigenfunctions of stress in the Rolie-Poly and Johnson-Segalman models are highly localised to that region of the base state where the shear-rate varies most sharply. In White-Metzner, the degree of shear-thinning is constant throughout the channel, and the eigenfunctions are spread out. Therefore, our findings suggest that some combination of shear-thinning and normal stress differences are necessary to observe instability.

Outline for future work. The results of this study suggest that the instability of pressure driven channel flow to two-dimensional perturbations may be generic across shear-thinning constitutive models. There exist several previous theoretical studies of this instability in other constitutive models, such as Giesekus and Phan-Thien-Tanner [103], eXtended Pom-Pom [107], Bautista-Manero-Puig [17] and additional variations of the White-Metzner model [15, 16]. An immediate direction for future research would be to perform a meta-analysis of the findings of these studies and to establish if the criteria found to be effective here also works for past studies. It would also be of interest to perform full non-linear simulations within the unstable regime for each of the models studied, thereby establishing which model best reproduces the results of experiment at longer timescales.

The parameters used in our theoretical study, P'^{*}, $\frac{d\log\Sigma}{d\log\dot{\gamma}}|_{min}$, $\frac{dN_1}{d\Sigma}|_{max}$, may be determined from experimental measurements. This could be done for a number of different viscoelastic fluids, such as the different polymer concentrations in Refs. [18, 19, 110]. A further avenue for research would be to fit the experimentally measured flow curves with the models studied here. We have shown that the different models studied can display different levels of stability, despite exhibiting the same degree of shear-thinning. By establishing the effectiveness of constitutive models to reproduce flow instabilities seen in experiment, it may provide an important tool for model building in future. The feasibility of performing such a study, however, remains speculative. Any such work would require close collaboration between experimentalists and theoreticians.

6.2 Ductile to Brittle Yielding in Soft Glassy Materials

Summary of main results. In this chapter, we examined the yielding of soft glassy materials during shear start-up. We performed numerical calculations using the soft glassy rheology model in three different preparation protocols. Our findings showed that in both thermal and athermal materials, better annealed samples displayed more sudden yielding. We also demonstrated this to be the case for samples sheared at lower rates during start-up.

We characterised the rate of yielding and the maximum degree of banding during start-up as a function of annealing and shear-rate. In the first protocol we studied, based on the ageing protocol implemented by Moorcroft et al. [25], the samples were sheared at non-zero noise temperature. We observed that the overshoot height in this case is dependent on the applied shear-rate. For smaller overshoots, the start-up curves with heterogeneous flow allowed do not break off from the corresponding curve with homogeneity enforced.

In the other protocols, for which the system was sheared at zero noise temperature, this is not the case. The homogeneous start-up curve is instead almost independent of the applied shear-rate. As the shear-rate decreases the rate of yielding increases in a similar manner to the behaviour seen in simulations of athermal soft glasses [24]. The start-up curve with heterogeneous flow allowed breaks off from the homogeneous start-up curve even for small overshoots. This suggests that athermal systems may always display brittle yielding for sufficiently small shear-rates.

In each of the protocols studied, we calculated the stress response as a function of strain for systems with homogeneity enforced and with heterogeneous flow allowed. We do not observe a qualitative variation in the shape of the homogeneous start-up curve that was suggested in Refs. [22,23]. Our findings show in all protocols a consistent relationship between yielding and the formation of shear-bands. The results of this study therefore offer an alternative hypothesis to the spinodal decomposition mechanism espoused by these studies. It instead suggests that yielding is a product of homogeneous flow becoming unstable to the formation of shear-bands.

Outline for future work. The most apparent avenue for future work is to assess the effects of noise temperature on yielding. We have observed in this study qualitative differences in behaviour between athermal and thermal systems. Future calculations performed at different effective noise temperatures may reveal more about the influence of finite temperatures on the dynamics of yielding. The influence of finite temperature dynamics, in the context of shear start-up, has been explored in simulation by Shristavaz et al. [28,33], but they did not characterise the effects of temperature on yielding. A collaborative study using both simulation and mesoscopic modelling may be best suited to fully investigate these phenomena.

In the study performed here, we have shown that the severity of yielding in athermal systems diverges with decreasing shear-rate. This is consistent with simulations performed under AQS, which imitates zero shear-rate start-up. For completeness, such an algorithm could be developed that would allow such calculations to be performed in SGR, thereby confirming that our findings are completely consistent with simulation.

6.3 Ultra-Long-Lived Transient Shear Banding in Soft Glassy Materials

Summary of main results. Our study in this chapter examines the evolution of shear-banded systems during shear start-up. We do so in a novel elastoplastic lattice model that incorporates the ageing dynamics of SGR as well as affine advection. We study the longevity of shear-bands as a function of sample preparation and applied shear-rate. This study is performed using two different preparation protocols, with shear applied at zero and non-zero noise temperature. The protocols used replicate those in the simulations of Shrivastav et al. [28, 33] and Vasisht et al. [29, 32]. Our calculations of the longevity of shear-bands, measured as the fluidisation time τ_f, show results qualitatively consistent with these simulations.

In the first protocol, we observe that the bands grow as $w_b \sim \bar{\gamma}^{1/2}$ in accordance with the findings of Refs [28, 33, 34]. The lifetime of bands was found to increase with sample age t_w with power law dependence $\tau_f \sim t_w^{1/2}$ for all applied shear-rates. We also observed that the fluidisation times increases as a power law $\tau_f \sim \bar{\dot{\gamma}}^{-p}$ for all sample ages, but that the exponent was less that one for all sample ages studied. This result is broadly consistent with the findings of experiment [27] and simulation [28]. In previous studies, however, the exponent p has always been found to be greater than unity, even in the non-zero temperature simulations of Ref. [33]. In this protocol, shear-bands in systems subjected to a higher strain-rate will persist to larger strains, but shorter times.

The second protocol is inspired by the work of Vasisht and collaborators [29, 32]. In this protocol, we examine the evolution of shear-bands at zero effective noise temperature following cooling. Here we see that the fluidisation time also follows a power-law function of shear-rate $\tau_f \sim \overline{\dot{\gamma}}^{-p}$, with $p > 1$. The exponent p increases as an exponential function of the cooling rate α. These results are in qualitative agreement with those of Ref. [32]. Their findings, however, differ quantitatively and show a much smaller increase in the value of p with decreasing cooling rate.

We have therefore shown that the model introduced in this chapter is effective at reproducing many of the behaviours observed in soft glassy materials in the shear start-up protocol. Further study is required, however, to establish if this model can replicate other behaviours observed in amorphous materials.

Outline for future work. This study looks at the longevity of shear bands subject to a shear start-up protocol. A first course of further study may therefore be to look at how this model behaves subject to different start-up protocols, such as stress controlled flow [70, 169, 187]. Performing such a study may be a relatively straightforward way of further establishing the effectiveness of the model to simulate elastoviscoplastic materials.

As in the previous study, an interesting way forward for future research lies in studying the effects of finite temperature on the transient dynamics of heterogeneous flows. Such a study could establish a relationship between the dynamics resulting from temperature effects and those caused by imposed deformation. This could offer greater insights into the different rheology of thermal and athermal systems. Some debate still remains, however, concerning the relationship between effective noise temperature and true thermal effects [156].

Further direction of research lie in studying precisely how the transition from an elastic to a fluid like response occurs, particularly how and where a material yields [208]. Many studies have been performed that attempt to establish precursors to mechanical yielding, such as correlations between local plastic events [191, 192, 212]. Investigating how these plastic events act as precursors to yielding may prove a fruitful avenue for future research using mesoscopic models.

6.4 Closing Remarks

Finally, the studies performed in this thesis have examined some of the rich variety of flow instabilities observed in complex fluids. Our examination of these systems has been motivated by previous theoretical, experimental and simulation based studies. We hope that the results presented here may in turn motivate others to perform further investigations which will build upon the results and methods introduced in this thesis.

Bibliography

[1] D. F. James. Open channel siphon with viscoelastic fluids. *Nature*, 212(5063):754–756, 1966.

[2] D. Saville and D. Thompson. Secondary flows associated with the Weissenberg effect. *Nature*, 223(5204):391–392, 1969.

[3] A. Kaye. A bouncing liquid stream. *Nature*, 197(4871):1001–1002, 1963.

[4] T. C. Polachini, R. C. Basso, and J. Telis-Romero. Rheology and fluid dynamic of egg white: Effect of thixotropy on engineering design. *Journal of Food Process Engineering*, 40(1):e12277, 2017.

[5] G. L. Wilkes. An overview of the basic rheological behavior of polymer fluids with an emphasis on polymer melts. *Journal of Chemical Education*, 58(11):880, 1981.

[6] M. Cates. Nonlinear viscoelasticity of wormlike micelles (and other reversibly breakable polymers). *Journal of Physical Chemistry*, 94(1):371–375, 1990.

[7] P. Bottiglieri, F. De Sio, G. Fasanaro, G. Mojoli, M. Impembo, and D. Castaldo. Rheological characterization of ketchup. *Journal of Food Quality*, 14(6):497–512, 1991.

[8] L. Ma and G. Barbosa-Cánovas. Rheological characterization of mayonnaise. part ii: Flow and viscoelastic properties at different oil and xanthan gum concentrations. *Journal of Food Engineering*, 25(3):409–425, 1995.

[9] P. Stevenson, editor. *Foam Engineering: fundamentals and applications.* John Wiley & Sons, Ltd, Feb. 2012.

[10] D. I. Wilson. Industrial applications of yield stress fluids. In *Lectures on Visco-Plastic Fluid Mechanics*, pages 195–259. Springer, 2019.

[11] P. D. Olmsted. Perspectives on shear banding in complex fluids. *Rheologica Acta*, 47(3):283–300, 2008.

[12] S. M. Fielding. Shear banding in soft glassy materials. *Reports on Progress in Physics*, 77(10):102601, 2014.

[13] T. Divoux, M. A. Fardin, S. Manneville, and S. Lerouge. Shear banding of complex fluids. *Annual Review of Fluid Mechanics*, 48:81–103, 2016.

[14] H. J. Wilson and J. M. Rallison. Instability of channel flow of a shear-thinning White–Metzner fluid. *Journal of Non-Newtonian fluid mechanics*, 87(1):75–96, 1999.

[15] H. J. Wilson and V. Loridan. Linear instability of a highly shear-thinning fluid in channel flow. *Journal of Non-Newtonian Fluid Mechanics*, 223:200–208, Sept. 2015.

[16] H. A. Castillo and H. J. Wilson. Towards a mechanism for instability in channel flow of highly shear-thinning viscoelastic fluids. *Journal of Non-Newtonian Fluid Mechanics*, 247:15–21, Sept. 2017.

[17] H. A. Castillo and H. J. Wilson. Elastic instabilities in pressure-driven channel flow of thixotropic-viscoelasto-plastic fluids. *Journal of Non-Newtonian Fluid Mechanics*, 261:10 – 24, 2018.

[18] H. Bodiguel, J. Beaumont, A. Machado, L. Martinie, H. Kellay, and A. Colin. Flow enhancement due to elastic turbulence in channel flows of shear thinning fluids. *Physical Review Letters*, 114(2), Jan. 2015.

[19] R. J. Poole. Elastic instabilities in parallel shear flows of a viscoelastic shear-thinning liquid. *Physical Review Fluids*, 1(4):041301, 2016.

[20] L. Picaut, O. Ronsin, C. Caroli, and T. Baumberger. Experimental evidence of a helical, supercritical instability in pipe flow of shear thinning fluids. *Physical Review Fluids*, 2(8), Aug. 2017.

[21] Y. M. Joshi and G. Petekidis. Yield stress fluids and ageing. *Rheologica Acta*, 57(6-7):521–549, 2018.

[22] M. Ozawa, L. Berthier, G. Biroli, A. Rosso, and G. Tarjus. Random critical point separates brittle and ductile yielding transitions in amorphous materials. *Proceedings of the National Academy of Sciences*, 115(26):6656–6661, 2018.

[23] M. Popović, T. W. J. de Geus, and M. Wyart. Elastoplastic description of sudden failure in athermal amorphous materials during quasistatic loading. *Physical Review E*, 98:040901, Oct 2018.

[24] M. Singh, M. Ozawa, and L. Berthier. Brittle yielding of amorphous solids at finite shear rates. *Physical Review Materials*, 4(2), Feb. 2020.

[25] R. L. Moorcroft, M. E. Cates, and S. M. Fielding. Age-dependent transient shear banding in soft glasses. *Physical Review Letters*, 106(5):055502, 2011.

[26] S. M. Fielding. Triggers and signatures of shear banding in steady and time-dependent flows. *Journal of Rheology*, 60(5):821–834, 2016.

[27] T. Divoux, D. Tamarii, C. Barentin, and S. Manneville. Transient shear banding in a simple yield stress fluid. *Physical Review Letters*, 104:208301, May 2010.

[28] G. P. Shrivastav, P. Chaudhuri, and J. Horbach. Heterogeneous dynamics during yielding of glasses: Effect of aging. *Journal of Rheology*, 60(5):835–847, 2016.

[29] V. V. Vasisht and E. Del Gado. Computational study of transient shear banding in soft jammed solids. *Physical Review E*, 102:012603, Jul 2020.

[30] D. Rodney, A. Tanguy, and D. Vandembroucq. Modeling the mechanics of amorphous solids at different length scale and time scale. *Modelling and Simulation in Materials Science and Engineering*, 19(8):083001, 2011.

[31] A. Nicolas, E. E. Ferrero, K. Martens, and J.-L. Barrat. Deformation and flow of amorphous solids: Insights from elastoplastic models. *Reviews of Modern Physics*, 90(4):045006, 2018.

[32] V. V. Vasisht, G. Roberts, and E. Del Gado. Emergence and persistence of flow inhomogeneities in the yielding and fluidization of dense soft solids. *Physical Review E*, 102:010604, Jul 2020.

[33] G. P. Shrivastav, P. Chaudhuri, and J. Horbach. Yielding of glass under shear: A directed percolation transition precedes shear-band formation. *Physical Review E*, 94:042605, Oct 2016.

[34] D. D. Alix-Williams and M. L. Falk. Shear band broadening in simulated glasses. *Physical Review E*, 98(5):053002, 2018.

[35] D. J. Acheson. *Elementary Fluid Dynamics*, volume 89. Acoustical Society of America (ASA), 1991.

[36] E. Hemingway, A. Clarke, J. Pearson, and S. Fielding. Thickening of viscoelastic flow in a model porous medium. *Journal of Non-Newtonian Fluid Mechanics*, 251:56 – 68, 2018.

[37] J. Blake. A note on the image system for a Stokeslet in a no-slip boundary. In *Mathematical Proceedings of the Cambridge Philosophical Society*, volume 70, pages 303–310. Cambridge University Press, 1971.

[38] R. G. Larson. *The Structure and Rheology of Complex Fluids.* Topics in Chemical Engineering. Oxford University Press USA, 1999.

[39] J. Mewis and N. Wagner. *Colloidal Suspension Rheology.* Cambridge Series in Chemical Engineering. Cambridge University Press, 2011.

[40] J. Ryder and J. Yeomans. Shear thinning in dilute polymer solutions. *The Journal of Chemical Physics*, 125(19):194906, 2006.

[41] J. Ding, P. Tracey, W. Li, G. Peng, P. G. Whitten, and G. G. Wallace. Review on shear thickening fluids and applications. *Textiles and Light Industrial Science and Technology*, 2(4):161–173, 2013.

[42] T. Tian, M. Nakano, and W. Li. Applications of shear thickening fluids: a review. *International Journal of Hydromechatronics*, 1(2):238–257, 2018.

[43] J. Ding, W. Li, and S. Z Shen. Research and applications of shear thickening fluids. *Recent Patents on Materials Science*, 4(1):43–49, 2011.

[44] D. Bonn, M. M. Denn, L. Berthier, T. Divoux, and S. Manneville. Yield stress materials in soft condensed matter. *Reviews of Modern Physics*, 89:035005, Aug 2017.

[45] P. Coussot. Yield stress fluid flows: A review of experimental data. *Journal of Non-Newtonian Fluid Mechanics*, 211:31 – 49, 2014.

[46] E. C. Bingham. *Fluidity and Plasticity*, volume 2. McGraw-Hill, 1922.

[47] R. G. Larson. *Constitutive Equations for Polymer Melts and Solutions: Butterworths Series in Chemical Engineering.* Butterworth-Heinemann, 2013.

[48] T. Osswald and N. Rudolph. *Polymer Rheology.* Carl Hanser Verlag GmbH & Co. KG, Nov. 2014.

[49] D. Boger. A highly elastic constant-viscosity fluid. *Journal of Non-Newtonian Fluid Mechanics*, 3(1):87–91, 1977.

[50] F. A. Morrison. *Understanding Rheology.* Raymond F. Boyer Library Collection. Oxford University Press, 2001.

[51] D. V. Boger and K. Walters. *Rheological phenomena in focus.* Elsevier, 2012.

[52] R. Tanner. *Engineering Rheology.* Oxford Engineering Science Series. Oxford University Press, 2000.

[53] R. G. Larson. Instabilities in viscoelastic flows. *Rheologica Acta*, 31(3):213–263, 1992.

[54] E. S. Shaqfeh. Purely elastic instabilities in viscometric flows. *Annual Review of Fluid Mechanics*, 28(1):129–185, 1996.

[55] F. L. Muller and J. F. Davidson. Rheology of shear thinning polymer solutions. *Industrial & engineering chemistry research*, 33(10):2364–2367, 1994.

[56] H. J. Wilson. Instabilities and constitutive modelling. *Philosophical Transactions of the Royal Society A: Mathematical, Physical and Engineering Sciences*, 364(1849):3267–3283, 2006.

[57] C. J. Petrie and M. M. Denn. Instabilities in polymer processing. *AIChE Journal*, 22(2):209–236, 1976.

[58] J. Yerushalmi, S. Katz, and R. Shinnar. The stability of steady shear flows of some viscoelastic fluids. *Chemical Engineering Science*, 25(12):1891–1902, 1970.

[59] S. Manneville. Recent experimental probes of shear banding. *Rheologica Acta*, 47(3):301–318, 2008.

[60] P. Schall and M. van Hecke. Shear bands in matter with granularity. *Annual Review of Fluid Mechanics*, 42, 2010.

[61] N. Germann. Shear banding in semidilute entangled polymer solutions. *Current Opinion in Colloid and Interface Science*, 39:1 – 10, 2019.

[62] K. A. Carter, J. M. Girkin, and S. M. Fielding. Shear banding in large amplitude oscillatory shear (laostrain and laostress) of polymers and wormlike micelles. *Journal of Rheology*, 60(5):883–904, 2016.

[63] R. Radhakrishnan, T. Divoux, S. Manneville, and S. M. Fielding. Understanding rheological hysteresis in soft glassy materials. *Soft Matter*, 13:1834–1852, 2017.

[64] T. Divoux, C. Barentin, and S. Manneville. Stress overshoot in a simple yield stress fluid: An extensive study combining rheology and velocimetry. *Soft Matter*, 7(19):9335–9349, 2011.

[65] V. Grenard, T. Divoux, N. Taberlet, and S. Manneville. Timescales in creep and yielding of attractive gels. *Soft Matter*, 10(10):1555–1571, 2014.

[66] Y. Kim, A. Adams, W. H. Hartt, R. G. Larson, and M. J. Solomon. Transient, near-wall shear-band dynamics in channel flow of wormlike micelle solutions. *Journal of Non-Newtonian Fluid Mechanics*, 232:77–87, 2016.

[67] S. Rogers, D. Vlassopoulos, and P. Callaghan. Aging, yielding, and shear banding in soft colloidal glasses. *Physical Review Letters*, 100:128304, 2008.

[68] R. L. Moorcroft and S. M. Fielding. Criteria for shear banding in time-dependent flows of complex fluids. *Physical Review Letters*, 110:086001, Feb 2013.

[69] R. L. Moorcroft and S. M. Fielding. Shear banding in time-dependent flows of polymers and wormlike micelles. *Journal of Rheology*, 58(1):103–147, 2014.

[70] T. Divoux, D. Tamarii, C. Barentin, S. Teitel, and S. Manneville. Yielding dynamics of a herschel–bulkley fluid: a critical-like fluidization behaviour. *Soft Matter*, 8(15):4151–4164, 2012.

[71] T. Gibaud, C. Barentin, N. Taberlet, and S. Manneville. Shear-induced fragmentation of laponite suspensions. *Soft Matter*, 5(16):3026–3037, 2009.

[72] J. D. Martin and Y. T. Hu. Transient and steady-state shear banding in aging soft glassy materials. *Soft Matter*, 8(26):6940–6949, 2012.

[73] Y. Wei, M. J. Solomon, and R. G. Larson. Time-dependent shear rate inhomogeneities and shear bands in a thixotropic yield-stress fluid under transient shear. *Soft Matter*, 15:7956–7967, 2019.

[74] T. Gibaud, D. Frelat, and S. Manneville. Heterogeneous yielding dynamics in a colloidal gel. *Soft Matter*, 6(15):3482–3488, 2010.

[75] G. Ovarlez, L. Tocquer, F. Bertrand, and P. Coussot. Rheopexy and tunable yield stress of carbon black suspensions. *Soft Matter*, 9(23):5540–5549, 2013.

[76] R. Mendes, G. Vinay, G. Ovarlez, and P. Coussot. Reversible and irreversible destructuring flow in waxy oils: An MRI study. *Journal of Non-Newtonian Fluid Mechanics*, 220:77–86, 2015.

[77] S. A. Rogers, P. T. Callaghan, G. Petekidis, and D. Vlassopoulos. Time-dependent rheology of colloidal star glasses. *Journal of Rheology*, 54(1):133–158, 2010.

[78] W. H. Press, S. A. Teukolsky, W. T. Vetterling, and B. P. Flannery. *Numerical Recipes in C (2Nd Ed.): The Art of Scientific Computing.* Cambridge University Press, New York, NY, USA, 1992.

[79] Y. Li. Wavenumber-extended high-order upwind-biased finite-difference schemes for convective scalar transport. *Journal of Computational Physics*, 133(2):235 – 255, 1997.

[80] J. P. Boyd. *Chebyshev and Fourier spectral methods.* Courier Corporation, 2001.

[81] E. O. Brigham and R. Morrow. The fast fourier transform. *IEEE spectrum*, 4(12):63–70, 1967.

[82] R. G. Larson, E. S. Shaqfeh, and S. J. Muller. A purely elastic instability in Taylor–Couette flow. *Journal of Fluid Mechanics*, 218:573–600, 1990.

[83] D. O. Olagunju. Instabilities and bifurcations of von kármán similarity solutions in swirling viscoelastic flow. *Zeitschrift für angewandte Mathematik und Physik*, 46(2):224–238, 1995.

[84] B. A. Schiamberg, L. T. Shereda, H. Hu, and R. G. Larson. Transitional pathway to elastic turbulence in torsional, parallel-plate flow of a polymer solution. *Journal of Fluid Mechanics*, 554:191–216, 2006.

[85] A. N. Morozov and W. van Saarloos. Subcritical finite-amplitude solutions for plane Couette flow of viscoelastic fluids. *Physical Review Letters*, 95(2):024501, 2005.

[86] A. Morozov and W. van Saarloos. Subcritical instabilities in plane Poiseuille flow of an Oldroyd-B fluid. *Journal of Statistical Physics*, 175(3):554–577, May 2019.

[87] B. Qin and P. E. Arratia. Characterizing elastic turbulence in channel flows at low Reynold's number. *Physical Review Fluids*, 2(8):083302, 2017.

[88] L. Pan, A. Morozov, C. Wagner, and P. Arratia. Nonlinear elastic instability in channel flows at low Reynold's numbers. *Physical Review Letters*, 110(17):174502, 2013.

[89] P. Pakdel and G. H. McKinley. Elastic instability and curved streamlines. *Physical Review Letters*, 77(12):2459, 1996.

[90] R. J. Poole. The Deborah and Weissenberg numbers. *The British Society of Rheology - Rheology Bulletin*, 53:32–39, 06 2012.

[91] H. J. Wilson and J. M. Rallison. Instability of channel flows of elastic liquids having continuously stratified properties. *Journal of Non-Newtonian Fluid Mechanics*, 85(2-3):273–298, 1999.

[92] T. C. Ho and M. M. Denn. Stability of plane Poiseuille flow of a highly elastic liquid. *Journal of Non-Newtonian Fluid Mechanics*, 3(2):179–195, 1977.

[93] V. Gorodtsov and A. Leonov. On a linear instability of a plane parallel Couette flow of viscoelastic fluid. *Journal of Applied Mathematics and Mechanics*, 31(2):310 – 319, 1967.

[94] H. J. Wilson and J. M. Rallison. Short wave instability of co-extruded elastic liquids with matched viscosities. *Journal of Non-Newtonian fluid mechanics*, 72(2-3):237–251, 1997.

[95] J. C. Miller and J. Rallison. Instability of coextruded elastic liquids at high Weissenberg number. *Journal of Non-Newtonian Fluid Mechanics*, 143:88–106, 2007.

[96] J. Miller and J. Rallison. Interfacial instability between sheared elastic liquids in a channel. *Journal of Non-Newtonian Fluid Mechanics*, 143(2-3):71–87, 2007.

[97] S. M. Fielding. Linear instability of planar shear banded flow. *Physical Review Letters*, 95:134501, Sep 2005.

[98] S. M. Fielding and H. J. Wilson. Shear banding and interfacial instability in planar Poiseuille flow. *Journal of Non-Newtonian Fluid Mechanics*, 165(5-6):196–202, 2010.

[99] S. M. Fielding and P. D. Olmsted. Nonlinear dynamics of an interface between shear bands. *Physical Review Letters*, 96:104502, Mar 2006.

[100] P. Nghe, S. M. Fielding, P. Tabeling, and A. Ajdari. Interfacially driven instability in the microchannel flow of a shear-banding fluid. *Physical Review Letters*, 104:248303, Jun 2010.

[101] M.-A. Fardin, L. Casanellas, B. Saint-Michel, S. Manneville, and S. Lerouge. Shear-banding in wormlike micelles: Beware of elastic instabilities. *Journal of Rheology*, 60(5):917–926, 2016.

[102] J. White and A. Metzner. Development of constitutive equations for polymeric melts and solutions. *Journal of Applied Polymer Science*, 7(5):1867–1889, 1963.

[103] A. M. Grillet, A. C. Bogaerds, G. W. Peters, and F. P. Baaijens. Stability analysis of constitutive equations for polymer melts in viscometric flows. *Journal of Non-Newtonian Fluid Mechanics*, 103(2-3):221–250, 2002.

[104] L. Blonce. Linear stability of Giesekus fluid in Poiseuille flow. *Mechanics Research Communications*, 24(2):223 – 228, 1997.

[105] F. Lim and W. Schowalter. Pseudo-spectral analysis of the stability of pressure-driven flow of a Giesekus fluid between parallel planes. *Journal of Non-Newtonian Fluid Mechanics*, 26(1):135 – 142, 1987.

[106] A. Palmer. Linear Stability Analyses of Poiseuille Flows of Viscoelastic Liquids. 2007.

[107] A. C. Bogaerds, A. M. Grillet, G. W. Peters, and F. P. Baaijens. Stability analysis of polymer shear flows using the extended pompom constitutive equations. *Journal of Non-Newtonian Fluid Mechanics*, 108(1):187 – 208, 2002. Numerical Methods Workshop S.I.

[108] B. Qin, P. F. Salipante, S. D. Hudson, and P. E. Arratia. Flow resistance and structures in viscoelastic channel flows at low Re. *Physical Review Letters*, 123(19):194501, 2019.

[109] A. Varshney and V. Steinberg. Drag enhancement and drag reduction in viscoelastic flow. *Physical Review Fluids*, 3:103302, Oct 2018.

[110] B. Chandra, R. Mangal, D. Das, and V. Shankar. Instability driven by shear thinning and elasticity in the flow of concentrated polymer solutions through microtubes. *Physical Review Fluids*, 4:083301, Aug 2019.

[111] F. Bautista, J. De Santos, J. Puig, and O. Manero. Understanding thixotropic and antithixotropic behavior of viscoelastic micellar solutions and liquid crystalline dispersions. i. the model. *Journal of Non-Newtonian Fluid Mechanics*, 80(2-3):93–113, 1999.

[112] A. E. Likhtman and R. S. Graham. Simple constitutive equation for linear polymer melts derived from molecular theory: Rolie-Poly equation. *Journal of Non-Newtonian Fluid Mechanics*, 2003.

[113] M. W. Johnson and D. Segalman. A model for viscoelastic fluid behavior which allows non-affine deformation. *Journal of Non-Newtonian Fluid Mechanics*, 1977.

[114] H. B. Squire. On the stability for three-dimensional disturbances of viscous fluid flow between parallel walls. *Proceedings of the Royal Society of London. Series A, Containing Papers of a Mathematical and Physical Character*, 142(847):621–628, 1933.

[115] F. Lockett. On Squire's theorem for viscoelastic fluids. *International Journal of Engineering Science*, 7(3):337–349, 1969.

[116] R. S. Graham, A. E. Likhtman, T. C. B. McLeish, and S. T. Milner. Microscopic theory of linear, entangled polymer chains under rapid deformation including chain stretch and convective constraint release. *Journal of Rheology*, 2003.

[117] T. C. B. McLeish and R. G. Larson. Molecular constitutive equations for a class of branched polymers: The pom-pom polymer. *Journal of Rheology*, 42(1):81–110, 1998.

[118] H. J. Wilson and S. M. Fielding. Linear instability of planar shear banded flow of both diffusive and non-diffusive johnsonsegalman fluids. *Journal of Non-Newtonian Fluid Mechanics*, 138(2):181 – 196, 2006.

[119] H. J. Wilson, M. Renardy, and Y. Renardy. Structure of the spectrum in zero reynolds number shear flow of the UCM and Oldroyd–B liquids. *Journal of Non-Newtonian Fluid Mechanics*, 80(2-3):251–268, 1999.

[120] J. G. Oldroyd. On the formulation of rheological equations of state. *Proceedings of the Royal Society of London. Series A. Mathematical and Physical Sciences*, 200(1063):523–541, 1950.

[121] S. F. Edwards. The statistical mechanics of polymerized material. *Proceedings of the Physical Society*, 92(1):9–16, 1967.

[122] M. Doi and S. F. Edwards. *The theory of polymer dynamics*, volume 73. Oxford University Press, 1988.

[123] G. Ianniruberto and G. Marrucci. Convective constraint release (ccr) revisited. *Journal of Rheology*, 58(1):89–102, 2014.

[124] D. Bonn and M. M. Denn. Yield stress fluids slowly yield to analysis. *Science*, 324(5933):1401–1402, 2009.

[125] P. Coussot. Rheophysics of pastes: a review of microscopic modelling approaches. *Soft Matter*, 3(5):528–540, 2007.

[126] M. M. Denn and D. Bonn. Issues in the flow of yield-stress liquids. *Rheologica Acta*, 50(4):307–315, 2011.

[127] M. Chen. A brief overview of bulk metallic glasses. *NPG Asia Materials*, 3(9):82–90, 2011.

[128] T. C. Hufnagel, C. A. Schuh, and M. L. Falk. Deformation of metallic glasses: Recent developments in theory, simulations, and experiments. *Acta Materialia*, 109:375–393, 2016.

[129] J. Knott. Brittle fracture in structural steels: perspectives at different size-scales. *Philosophical Transactions of the Royal Society A: Mathematical, Physical and Engineering Sciences*, 373(2038):20140126, 2015.

[130] C. A. Schuh, T. C. Hufnagel, and U. Ramamurty. Mechanical behavior of amorphous alloys. *Acta Materialia*, 55(12):4067–4109, 2007.

[131] R. A. C. Slater. Yield criteria for ductile metals. In *Engineering Plasticity*, pages 67–89. Macmillan Education UK, 1977.

[132] W. H. Herschel and R. Bulkley. Konsistenzmessungen von gummibenzollösungen. *Kolloid-Zeitschrift*, 39(4):291–300, Aug 1926.

[133] M. Dinkgreve, M. Fazilati, M. M. Denn, and D. Bonn. Carbopol: From a simple to a thixotropic yield stress fluid. *Journal of Rheology*, 62(3):773–780, 2018.

[134] F. Caton and C. Baravian. Plastic behavior of some yield stress fluids: from creep to long-time yield. *Rheologica Acta*, 47(5-6):601–607, 2008.

[135] A. Ikeda, L. Berthier, and P. Sollich. Disentangling glass and jamming physics in the rheology of soft materials. *Soft Matter*, 9:7669–7683, 2013.

[136] J. Z. Zhou, P. H. Uhlherr, and F. T. Luo. Yield stress and maximum packing fraction of concentrated suspensions. *Rheologica Acta*, 34(6):544–561, 1995.

[137] G. Parisi and F. Zamponi. Mean-field theory of hard sphere glasses and jamming. *Review Modern Physics*, 82:789–845, Mar 2010.

[138] M. Tsamados. Plasticity and dynamical heterogeneity in driven glassy materials. *The European Physical Journal E*, 32(2):165–181, 2010.

[139] C. Maloney and A. Lemaitre. Universal breakdown of elasticity at the onset of material failure. *Physical Review Letters*, 93(19):195501, 2004.

[140] A. Wisitsorasak and P. G. Wolynes. On the strength of glasses. *Proceedings of the National Academy of Sciences*, 109(40):16068–16072, 2012.

[141] P. Urbani and F. Zamponi. Shear yielding and shear jamming of dense hard sphere glasses. *Physical Review Letters*, 118(3):038001, 2017.

[142] G. Biroli and P. Urbani. Liu-Nagel phase diagrams in infinite dimension. *SciPost Physics*, 4:20, 2018.

[143] P. K. Jaiswal, I. Procaccia, C. Rainone, and M. Singh. Mechanical yield in amorphous solids: A first-order phase transition. *Physical Review Letters*, 116(8):085501, 2016.

[144] G. Parisi, I. Procaccia, C. Rainone, and M. Singh. Shear bands as manifestation of a criticality in yielding amorphous solids. *Proceedings of the National Academy of Sciences*, 114(22):5577–5582, 2017.

[145] A. D. Parmar, S. Kumar, and S. Sastry. Strain localization above the yielding point in cyclically deformed glasses. *Physical Review X*, 9(2):021018, 2019.

[146] J. D. Barry, D. Weaire, and S. Hutzler. Shear localisation with 2d viscous froth and its relation to the continuum model. *Rheologica Acta*, 49(6):687–698, 2010.

[147] A. Kabla, J. Scheibert, and G. Debregeas. Quasi-static rheology of foams. part 2. continuous shear flow. *Journal of Fluid Mechanics*, 587:45–72, 2007.

[148] T. Gibaud, C. Barentin, and S. Manneville. Influence of boundary conditions on yielding in a soft glassy material. *Physical Review Letters*, 101:258302, Dec 2008.

[149] J. Lin, T. Gueudré, A. Rosso, and M. Wyart. Criticality in the approach to failure in amorphous solids. *Physical Review Letters*, 115:168001, Oct 2015.

[150] S. Lerouge, J. P. Decruppe, and C. Humbert. Shear banding in a micellar solution under transient flow. *Physical Review Letters*, 81:5457–5460, Dec 1998.

[151] R. Radhakrishnan and S. M. Fielding. Shear banding of soft glassy materials in large amplitude oscillatory shear. *Physical Review Letters*, 117:188001, Oct 2016.

[152] P. Sollich. Rheological constitutive equation for a model of soft glassy materials. *Physical Review E*, 58:738–759, Jul 1998.

[153] J.-P. Bouchaud. Weak ergodicity breaking and aging in disordered systems. *Journal de Physique I*, 2:1705–1713, 1992.

[154] J.-P. Bouchaud and D. S. Dean. Aging on Parisi's tree. *Journal de Physique I*, 5(3):265–286, 1995.

[155] C. Monthus and J.-P. Bouchaud. Models of traps and glass phenomenology. *Journal of Physics A: Mathematical and General*, 29(14):3847, 1996.

[156] P. Sollich and M. E. Cates. Thermodynamic interpretation of soft glassy rheology models. *Physical Review E*, 85:031127, Mar 2012.

[157] S. M. Fielding, P. Sollich, and M. E. Cates. Aging and rheology in soft materials. *Journal of Rheology*, 44(2):323–369, 2000.

[158] S. Fielding, M. Cates, and P. Sollich. Shear banding, aging and noise dynamics in soft glassy materials. *Soft Matter*, 5(12):2378–2382, 2009.

[159] D. M. Hoyle and S. M. Fielding. Age-dependent modes of extensional necking instability in soft glassy materials. *Physical Review Letters*, 114:158301, Apr 2015.

[160] R. Radhakrishnan and S. M. Fielding. Shear banding in large amplitude oscillatory shear (laostrain and laostress) of soft glassy materials. *Journal of Rheology*, 62(2):559–576, 2018.

[161] N. Spenley, X. Yuan, and M. Cates. Nonmonotonic constitutive laws and the formation of shear-banded flows. *Journal de Physique II*, 6(4):551–571, 1996.

[162] S. M. Fielding and P. D. Olmsted. Nonlinear dynamics of an interface between shear bands. *Physical Review Letters*, 96:104502, Mar 2006.

[163] S. Fielding. Ageing, driving and effective temperatures from soft rheology" to glassy dynamics". *The University of Edinburgh*, 2000.

[164] H. J. Barlow, J. O. Cochran, and S. M. Fielding. Ductile and brittle yielding in thermal and athermal amorphous materials. *Physical Review Letters*, 125:168003, Oct 2020.

[165] W.-T. Yeh, M. Ozawa, K. Miyazaki, T. Kawasaki, and L. Berthier. Glass stability changes the nature of yielding under oscillatory shear. *Physical Review Letters*, 124:225502, Jun 2020.

[166] M. Leocmach, C. Perge, T. Divoux, and S. Manneville. Creep and fracture of a protein gel under stress. *Physical Review Letters*, 113:038303, Jul 2014.

[167] V. Grenard, T. Divoux, N. Taberlet, and S. Manneville. Timescales in creep and yielding of attractive gels. *Soft Matter*, 10, 2014.

[168] R. Benzi, T. Divoux, C. Barentin, S. Manneville, M. Sbragaglia, and F. Toschi. Unified theoretical and experimental view on transient shear banding. *Physical Review Letters*, 123(24):248001, 2019.

[169] P. Chaudhuri and J. Horbach. Onset of flow in a confined colloidal glass under an imposed shear stress. *Physical Review E*, 88:040301, Oct 2013.

[170] M. L. Manning, J. S. Langer, and J. Carlson. Strain localization in a shear transformation zone model for amorphous solids. *Physical Review E*, 76(5):056106, 2007.

[171] M. Manning, E. Daub, J. Langer, and J. Carlson. Rate-dependent shear bands in a shear-transformation-zone model of amorphous solids. *Physical Review E*, 79(1):016110, 2009.

[172] Y. Shi, M. B. Katz, H. Li, and M. L. Falk. Evaluation of the disorder temperature and free-volume formalisms via simulations of shear banding in amorphous solids. *Physical Review Letters*, 98(18), May 2007.

[173] A. R. Hinkle and M. L. Falk. A small-gap effective-temperature model of transient shear band formation during flow. *Journal of Rheology*, 60(5):873–882, 2016.

[174] E. A. Jagla. Shear band dynamics from a mesoscopic modeling of plasticity. *Journal of Statistical Mechanics: Theory and Experiment*, 2010(12):P12025, Dec. 2010.

[175] E. A. Jagla. Strain localization driven by structural relaxation in sheared amorphous solids. *Physical Review E*, 76:046119, Oct 2007.

[176] G. Picard, A. Ajdari, F. Lequeux, and L. Bocquet. Slow flows of yield stress fluids: Complex spatiotemporal behavior within a simple elastoplastic model. *Physical Review E*, 71(1):010501, 2005.

[177] G. Picard, A. Ajdari, F. Lequeux, and L. Bocquet. Elastic consequences of a single plastic event: A step towards the microscopic modeling of the flow of yield stress fluids. *The European Physical Journal E*, 15(4):371–381, 2004.

[178] J. D. Eshelby. The elastic field outside an ellipsoidal inclusion. *Proceedings of the Royal Society of London. Series A. Mathematical and Physical Sciences*, 252(1271):561–569, 1959.

[179] Z. Budrikis, D. F. Castellanos, S. Sandfeld, M. Zaiser, and S. Zapperi. Universal features of amorphous plasticity. *Nature Communications*, 8(1), July 2017.

[180] K. Karimi, E. E. Ferrero, and J.-L. Barrat. Inertia and universality of avalanche statistics: The case of slowly deformed amorphous solids. *Physical Review E*, 95(1), Jan. 2017.

[181] A. Tanguy, F. Leonforte, and J.-L. Barrat. Plastic response of a 2D Lennard–Jones amorphous solid: Detailed analysis of the local rearrangements at very slow strain rate. *The European Physical Journal E*, 20(3):355–364, 2006.

[182] M. L. Falk and J. S. Langer. Dynamics of viscoplastic deformation in amorphous solids. *Physical Review E*, 57(6):7192, 1998.

[183] J. Chattoraj and A. Lemaître. Elastic signature of flow events in supercooled liquids under shear. *Physical Review Letters*, 111(6), Aug. 2013.

[184] V. Chikkadi, G. Wegdam, D. Bonn, B. Nienhuis, and P. Schall. Long-range strain correlations in sheared colloidal glasses. *Physical Review Letters*, 107(19), Nov. 2011.

[185] P. Schall, D. A. Weitz, and F. Spaepen. Structural rearrangements that govern flow in colloidal glasses. *Science*, 318(5858):1895–1899, 2007.

[186] K. W. Desmond and E. R. Weeks. Measurement of stress redistribution in flowing emulsions. *Physical Review Letters*, 115(9), Aug. 2015.

[187] R. Cabriolu, J. Horbach, P. Chaudhuri, and K. Martens. Precursors of fluidisation in the creep response of a soft glass. *Soft Matter*, 15(3):415–423, 2019.

[188] C. E. Maloney and A. Lemaître. Amorphous systems in athermal, quasistatic shear. *Physical Review E*, 74(1), 2006.

[189] N. P. Bailey, J. Schiøtz, A. Lemaître, and K. W. Jacobsen. Avalanche size scaling in sheared three-dimensional amorphous solid. *Physical Review Letters*, 98(9):095501, 2007.

[190] T. Niiyama, M. Wakeda, T. Shimokawa, and S. Ogata. Structural relaxation affecting shear-transformation avalanches in metallic glasses. *Physical Review E*, 100(4), 2019.

[191] A. Lemaitre and C. Caroli. Rate-dependent avalanche size in athermally sheared amorphous solids. *Physical Review Letters*, 103(6):065501, 2009.

[192] D. Castellanos and M. Zaiser. Avalanche behavior in creep failure of disordered materials. *Physical Review Letters*, 121(12), Sept. 2018.

[193] J. L. Barrat and A. Lemaitre. *Dynamical heterogeneities in glasses, colloids, and granular media*, chapter Heterogeneities in amorphous systems under shear. Oxford University Press, Oxford New York, 2011.

[194] N. V. Priezjev. Shear band formation in amorphous materials under oscillatory shear deformation. *Metals*, 10(3):300, Feb. 2020.

[195] B. P. Bhowmik, P. Chaudhuri, and S. Karmakar. Effect of pinning on the yielding transition of amorphous solids. *Physical Review Letters*, 123(18):185501, 2019.

[196] K. Martens, L. Bocquet, and J.-L. Barrat. Spontaneous formation of permanent shear bands in a mesoscopic model of flowing disordered matter. *Soft Matter*, 8(15):4197, 2012.

[197] A. Nicolas, K. Martens, L. Bocquet, and J.-L. Barrat. Universal and non-universal features in coarse-grained models of flow in disordered solids. *Soft Matter*, 10(26):4648–4661, 2014.

[198] K. Karimi and J.-L. Barrat. Correlation and shear bands in a plastically deformed granular medium. *Scientific Reports*, 8(1):4021, 2018.

[199] H. Ruan, L. Zhang, and J. Lu. A new constitutive model for shear banding instability in metallic glass. *International Journal of Solids and Structures*, 48(21):3112–3127, 2011.

[200] D. Vandembroucq and S. Roux. Mechanical noise dependent aging and shear banding behavior of a mesoscopic model of amorphous plasticity. *Physical Review B*, 84(13):134210, 2011.

[201] C. Liu, S. Dutta, P. Chaudhuri, and K. Martens. An elasto-plastic approach based on microscopic insights for the steady state and transient dynamics of sheared disordered solids. *arXiv preprint arXiv:2007.07162*, 2020.

[202] M. Denn. *Dynamics of complex fluids : proceedings of the Second Royal Society-Unilever Indo-UK Forum in Materials Science and Engineering*, chapter Are plug-flow regions possible in fluids exhibiting a yield stress. Dynamics of Complex Fluids, pages 372 – 378. Imperial College Press, London, 1998.

[203] A. Shaukat, M. Kaushal, A. Sharma, and Y. M. Joshi. Shear mediated elongational flow and yielding in soft glassy materials. *Soft Matter*, 8(39):10107, 2012.

[204] A. W. Lees and S. F. Edwards. The computer study of transport processes under extreme conditions. *Journal of Physics C: Solid State Physics*, 5(15):1921–1928, 1972.

[205] S. M. Fielding. Role of inertia in nonequilibrium steady states of sheared binary fluids. *Physical Review E*, 77(2), Feb. 2008.

[206] S. Aime, L. Ramos, J.-M. Fromental, G. Prevot, R. Jelinek, and L. Cipelletti. A stress-controlled shear cell for small-angle light scattering and microscopy. *Review of Scientific Instruments*, 87(12):123907, 2016.

[207] S. Aime, L. Ramos, and L. Cipelletti. Microscopic dynamics and failure precursors of a gel under mechanical load. *Proceedings of the National Academy of Sciences*, 115(14):3587–3592, 2018.

[208] L. Cipelletti, K. Martens, and L. Ramos. Microscopic precursors of failure in soft matter. *Soft Matter*, 16(1):82–93, 2020.

[209] A. Le Bouil, A. Amon, and J. Crassous. Experimental studies of precursors to failure in granular material. In *AIP Conference Proceedings*, volume 1542, pages 475–478. American Institute of Physics, 2013.

[210] A. Amon, A. Mikhailovskaya, and J. Crassous. Spatially resolved measurements of micro-deformations in granular materials using diffusing wave spectroscopy. *Review of Scientific Instruments*, 88(5):051804, 2017.

[211] A. Seguin. Hysteresis of the drag force of an intruder moving into a granular medium. *The European Physical Journal E*, 42(1):13, 2019.

[212] E. D. Cubuk, R. J. S. Ivancic, S. S. Schoenholz, D. J. Strickland, A. Basu, Z. S. Davidson, J. Fontaine, J. L. Hor, Y.-R. Huang, Y. Jiang, N. C. Keim, K. D. Koshigan, J. A. Lefever, T. Liu, X.-G. Ma, D. J. Magagnosc, E. Morrow, C. P. Ortiz, J. M. Rieser, A. Shavit, T. Still, Y. Xu, Y. Zhang, K. N. Nordstrom, P. E. Arratia, R. W. Carpick, D. J. Durian, Z. Fakhraai, D. J. Jerolmack, D. Lee, J. Li, R. Riggleman, K. T. Turner, A. G. Yodh, D. S. Gianola, and A. J. Liu. Structure-property relationships from universal signatures of plasticity in disordered solids. *Science*, 358(6366):1033–1037, 2017.